



저작자표시-비영리-변경금지 2.0 대한민국

이용자는 아래의 조건을 따르는 경우에 한하여 자유롭게

- 이 저작물을 복제, 배포, 전송, 전시, 공연 및 방송할 수 있습니다.

다음과 같은 조건을 따라야 합니다:



저작자표시. 귀하는 원저작자를 표시하여야 합니다.



비영리. 귀하는 이 저작물을 영리 목적으로 이용할 수 없습니다.



변경금지. 귀하는 이 저작물을 개작, 변형 또는 가공할 수 없습니다.

- 귀하는, 이 저작물의 재이용이나 배포의 경우, 이 저작물에 적용된 이용허락조건을 명확하게 나타내어야 합니다.
- 저작권자로부터 별도의 허가를 받으면 이러한 조건들은 적용되지 않습니다.

저작권법에 따른 이용자의 권리는 위의 내용에 의하여 영향을 받지 않습니다.

이것은 [이용허락규약\(Legal Code\)](#)을 이해하기 쉽게 요약한 것입니다.

[Disclaimer](#)

공학박사학위논문

**A STUDY ON SMALL SCALE
MECHANICAL BEHAVIOR FOR
DEFORMATION ANALYSIS OF DUPLEX
STAINLESS STEEL**

2상 스테인리스의 변형 해석을 위한
미소 스케일 기계적 거동에 대한 연구

2015년 7월

서울대학교 대학원
재료공학부
김 용 민

A STUDY ON SMALL SCALE MECHANICAL BEHAVIOR FOR DEFORMATION ANALYSIS OF DUPLEX STAINLESS STEEL

2상 스테인리스의 변형 해석을 위한
금속재료의 미소 스케일 기계적 거동에 대한 연구

지도교수 한 홍 남

이 논문을 공학박사학위논문으로 제출함
2015년 7월

서울대학교 대학원
재료공학부
김 용 민

김용민의 박사학위논문을 인준함
2015년 7월

위	원	장	오 규 환 (인)
부	위	원	장 한 홍 남 (인)
위		원	선 정 윤 (인)
위		원	김 동 익 (인)
위		원	우 완 측 (인)



ABSTRACT

Stainless steels are an important class of alloys and the use of stainless steels is indispensable. Above all, duplex stainless steels (DSS) are generally known as material combining good strength with corrosion properties. However, mechanical behavior of DSS is complex and inhomogeneous, since respective phases in DSS have different response to applied stress or strain. Therefore, in recent years, great effort has been made to understand complex deformation behavior of DSS. There are three conventional deformation analysis methods for DSS; (1) neutron diffraction analysis, (2) EBSD (texture) base analysis and (3) digital image base analysis. In this paper, these deformation analysis methods for DSS are reviewed and some demerits of the methods are reported. Then advanced analysis methods are developed and suggested in order to analyze complex deformation behavior of DSS, precisely.

Neutron diffraction is one of the conventional methods to analyze deformation behavior of DSS. Especially, the plastic yielding behavior of each phase in DSS was often focused by time-of-flight (TOF) analysis using in-situ neutron diffraction. However, it is difficult to separate the individual contribution of each phase from macroscopic applied stress or strain. And applied stress can't be measured precisely by this method since there is a

limitation in the step for the static load control during in-situ neutron diffraction. Besides, neutron diffraction has bad accessibility because the size of equipment is quite huge and there are few places that can use it. For these reasons, as more accessible technique, nanoindentation was suggested to measure plastic deformation behavior of each phase in DSS. Nanoindentation was chosen since separated intrinsic mechanical behavior of each phase can be measured, and applied stress can be obtained as continuous value by this technique.

In this research, two specimens of Fe-24.67Cr-7.04Mn-3.98Ni-3.88Mo-0.49Si-0.45N-0.022C (DSH) and Fe-17.2Cr-5.9Mn-5.01W-2.54Mo-0.31Si-0.43N-0.012C (DSL) were used. Nanoindentation tests were performed to measure intrinsic deformation behavior of individual α and γ grains guided by electron backscattered diffraction (EBSD). Generally, maximum shear stress underneath indenter tip when first pop-in occurs is considered as elasto-plastic transition stress by dislocation nucleation. Thus maximum shear stress when first pop-in occurs (τ_m) is measured to define elasto-plastic transition stress of each phase in DSH and DSL. In order to correlate the small-scale nanoindentation behavior to the macro-scale tensile behavior, an angular-dispersive in-situ neutron diffraction test was performed using a residual stress analysis diffractometer equipped with a deformation device enabling tensile deformation. And the correlation was investigated by comparing the

indentation load-depth (L-D) curves for each phase with the lattice strains of various lattice planes in α and γ obtained by in-situ neutron diffraction. In nanoindentation, γ had approximately 20% lower elasto-plastic transition stress than α in DSH, while both α and γ had similar elasto-plastic transition stress in DSL. And this tendency of elasto-plastic transition corresponded correctly to in-situ neutron diffraction data. Thus we concluded that tendency of maximum shear stress when first pop-in occurs can represent that of yield stress. Furthermore, the dislocation nucleation energy (DNE) was calculated based on nanoindentation results, since it is generally known that the pop-in is closely related with dislocation nucleation. As expected, these results correctly correspond with results from nanoindentation. Finally we could conclude that the difference of elasto-plastic transition stresses in both DSS can be explained by DNE and the SFE in austenite could be evaluated by nanoindentation based DNE calculation.

And secondly, EBSD supported DIC (digital image correlation) analysis was developed to improve both texture and digital image base deformation analysis methods for DSS. In texture base deformation analysis for DSS, the phase which has intensely distorted texture regards as severely deformed phase. However, correlation between strain and misorientation is not investigated clearly. Thus it is ambiguous to define deformation by texture information and, of course, accurate strain cannot be measured by EBSD base

deformation analysis. On the contrary, precise quantitative strain can be directly measured by digital image base deformation analysis method called DIC. But with this method, phase/grain boundaries cannot be identified clearly because they are observed by etched surface morphology. However, in order to analyze complex deformation of DSS, accurate quantitative local strain and precise phase/grain information are both necessary. Thus EBSD supported DIC analysis method was developed in order to measure accurate quantitative strain with regarding precise microstructure and texture. In addition, relation between local strain and misorientation was investigated to verify texture base deformation analysis.

In order to develop EBSD supported DIC technique, full annealed pure copper sheet (purity 99.9%) was used in this research. For DIC analysis, grayscale random pattern is required on the surface of specimen. Speckle patterning method has been conventionally used for this, but it is shown that speckle patterning is inappropriate for EBSD since the speckles disturb contact of electron beam. In order to obtain well indexed precise EBSD image with grayscale patterned surface image for DIC, carbon coat patterning technique was developed and applied. After carbon coat patterning, selected area of Cu specimen was captured while tensile test by in-situ SEM equipped with a deformation module. The area was also scanned by EBSD. The sequential SEM images during deformation were analyzed by DIC and

quantitative strain maps were drawn. Consequently, accurate quantitative strain, precise microstructure and texture of the selected area could be measured together. Then in order to investigate relation between local strain and misorientation, Kernel average misorientation (KAM) map and grain average misorientation (GAM) map were drawn and directly compared with local strain. As generally known, overall average state of misorientation correlated with macroscopic applied strain, statistically. However, it was shown that locally evaluated KAM/GAM values have quite weak correlation with applied local strain of the spot. One of the reasons for this tendency, we found that crystal distortion and increasing misorientation by deformation are influenced by orientational stability for deformation mode. That is, locally increased KAM/GAM values can be varied by initial orientation of observed area, not only applied strain. Thus we conclude that orientational stability for applied deformation mode should be regarded for reliable strain analysis by EBSD.

Keywords: Duplex stainless steel (DSS), Deformation analysis, Quantitative strain analysis, Neutron diffraction, Time of flight (TOF) analysis, Electron backscatter diffraction (EBSD), Scanning electron microscope (SEM), Nanoindentation, Elasto-plastic transition stress, Pop-in,

Hertzian contact theory, Dislocation nucleation energy (DNE), in-situ SEM, in-situ EBSD, Digital image correlation (DIC), Speckle patterning method, Carbon coat patterning method, Local strain, Texture, Misorientation, Kernel average misorientation (KAM), Grain average misorientation (GAM), Orientational stability

Student number: 2009-20589

Contents

Abstract	I
Table of Contents	VII
List of Tables	X
List of Figures	XI

1. Theoretical Background

1.1 Developments of stainless steels.....	1
1.2 Duplex stainless steel.....	6
1.3 Deformation analysis for duplex stainless steel.....	10
1.3.1 Neutron diffraction analysis.....	10
1.3.2 EBSD (Texture) base analysis.....	17
1.3.3 Digital image base analysis.....	25
1.4 Issues of existing deformation analysis for DSS and motivations for research	36
1.5 References	40

Part I

2. Investigation of yielding behavior of duplex stainless steel by nanoindentation, EBSD and in-situ neutron diffraction

2.1 Introduction	53
2.2 Materials and experimental procedures	59
2.2.1 Materials: Duplex Stainless Steel.....	59
2.2.2 Experimental procedure.....	70
2.3 EBSD combined Nanoindentation	74
2.4 In-situ neutron diffraction	84
2.5 Dislocation nucleation energy barrier calculation	92
2.6 Summary	102
2.7 References	103

Part II.

3. Investigation of correlation between strain and crystal orientation by EBSD supported DIC

3.1 Introduction	108
3.2 Experimental procedures	113
3.2.1. Material and processing.....	113
3.2.2. Developing carbon coat patterning method.....	115
3.2.3. DIC by using in-situ SEM image with EBSD.....	126
3.3 Relation between strain and crystal orientation	130
3.4 Summary	148
3.5 References	150
4. Conclusion	155

LIST OF TABLES

Table 2.1 Average elasto-plastic transition stress of respective phases in DSS.

Table 2.2 Corrected average elasto-plastic transition stress of respective phases in DSS considering the Hall–Petch relationship.

Table 2.3 Lattice parameter and length of Burgers vector measured by XRD.

Table 2.4 MS strain and SFP of γ (DSH) and γ (DSL).

Table 2.5 SFE of γ (DSH) and γ (DSL).

Table 3.1 Information of selected grains.

LIST OF FIGURES

Figure 1.1 Schematic image of the in-situ stress measuring system by neutron diffraction.

Figure 1.2 Change in the grain average misorientation (GAM) (a) with plastic strain in the tensile/compression specimens of the type 316NG and (b) with creep damage ratio in the specimens of the type 316 stainless steel creep tested at 600 °C.

Figure 1.3 KAM maps for evaluating local strain of weld joint: (a) austenite and (b) ferrite in the base metal, (c) austenite and (d) ferrite in the weld metal.

Figure 1.4 Fabrication of the microgrids; (a) polishing and electro-etching; (b) coating with an electro-sensitive polymer; (c) irradiation of the resin with the electron beam; (d) dissolution of the irradiated polymer; (e) engraving by electro-etching; (f) dissolution of the remaining polymer.

Figure 1.5 Example of a correspondence between the microgrids and the underlying microstructure with phase boundaries.

Figure 1.6 Logarithmic strain distribution maps after plane strain compression; (a) ϵ_{11} ; (b) ϵ_{22} ; (c) ϵ_{12} ; (d) ϵ_{eq} ; the strain maps are superimposed with the undeformed microstructure; the compression axis corresponds to the vertical

axis.

Figure 2.1 Price histories of stainless steel and Ni.

Figure 2.2 Phase map of (a) DSH and (b) DSL by EBSD.

Figure 2.3 Grain size distribution of DSH.

Figure 2.4 Grain size distribution of DSL.

Figure 2.5 S-S curves of DSH and DSL.

Figure 2.6 Crystal orientation map of DSH.

Figure 2.7 Crystal orientation map of DSL.

Figure 2.8 Orientation distribution function (ODF) of DSH.

Figure 2.9 Orientation distribution function (ODF) of DSL.

Figure 2.10 Phase map and crystal orientation (ND) map of indentation area.

Figure 2.11 Group of L-D curves of (a) α , (b) γ in DSH.

Figure 2.12 Group of L-D curves of (a) α , (b) γ in DSL.

Figure 2.13 Cumulative probability of pop-in of (a) DSH and (b) DSL, as a function of maximum stress under the indenter.

Figure 2.14 Schematic image of in-situ neutron diffraction.

Figure 2.15 changes in ε_{hkl} of (a) α , (b) γ in DSH, as a function of applied true stress for the $(200)_\alpha$, $(112)_\alpha$, $(110)_\alpha$, $(200)_\gamma$, $(311)_\gamma$ and $(222)_\gamma$ reflections.

Figure 2.16 changes in ε_{hkl} of (a) α , (b) γ in DSL, as a function of applied true stress for the $(200)_\alpha$, $(112)_\alpha$, $(110)_\alpha$, $(200)_\gamma$, $(311)_\gamma$ and $(222)_\gamma$ reflections.

Figure 2.17 Elasto-plastic transition stress tendency from (a) in-situ neutron diffraction test and (b) nanoindentation.

Figure 2.18 Shear stress of dislocation nucleation, τ_{dn} for (a) DSH and (b) DSL, as function of radius of dislocation loop.

Figure 3.1 ND orientation map of Cu specimen.

Figure 3.2 Schematic image of carbon coat patterning method.

Figure 3.3 SEM image of Cu specimen (a) before patterning, (b) after speckle patterning and ND orientation map of Cu specimen (c) before patterning, (d) after speckle patterning.

Figure 3.4 KAM map of Cu specimen (a) before patterning, (b) after speckle patterning and (c) enhanced KAM map from EBSD data of patterned specimen.

Figure 3.5 High angle misorientation distribution of Cu specimen (a) before patterning, (b) after speckle patterning and (c) enhanced result from EBSD data of patterned specimen.

Figure 3.6 SEM image of Cu specimen (a) before patterning, (b) after carbon coat patterning and ND orientation map of Cu specimen (c) before patterning, (d) after carbon coat patterning.

Figure 3.7 KAM map of Cu specimen (a) before patterning, (b) after carbon coat patterning and (c) enhanced KAM map from EBSD data of patterned specimen.

Figure 3.8 High angle misorientation distribution of Cu specimen (a) before patterning, (b) after speckle patterning and (c) enhanced result from EBSD data of patterned specimen.

Figure 3.9 SEM image of carbon coat patterned Cu specimen before deformation.

Figure 3.10 (a) Tensile stage and (b) control unit of deformation module

Figure 3.11 (a) ND orientation map and (b) maximum shear strain map with grain boundaries after 9.2% tensile test.

Figure 3.12 Maximum shear strain map calculated by (a) normal Cartesian coordination and (b) 45° rotated coordination.

Figure 3.13 KAM maps of (a) undeformed state and (b) 9.2% tensile deformed state.

Figure 3.14 KAM developments as function of maximum shear strain of 9.2% tensile specimen (a) with error bars and (b) without error bars.

Figure 3.15 GAM maps of (a) undeformed state and (b) 9.2% tensile deformed state.

Figure 3.16 Grain average maximum shear strain map after 9.2% tensile deformation.

Figure 3.17 GAM as function of grain average maximum shear strain of 9.2% tensile specimen.

Figure 3.18 (a) ND orientation map and (b) inverse pole figures of selected grains.

Figure 3.19 Maximum shear strain map and KAM map of (a) grain A and (b) grain B.

Figure 3.20 ND orientation map of (a) undeformed and (b) after 9.2% tensile state of grain A. And (c) maximum shear strain map and (d) misorientation map with original orientation of deformed grain A.

Figure 3.21 ND orientation map of (a) undeformed and (b) after 9.2% tensile state of grain B. And (c) maximum shear strain map and (d) misorientation map with original orientation of deformed grain B.

Figure 3.22 KAM values of selected grains as function of maximum shear strain.

1. Theoretical background

1.1 Developments of stainless steels

Stainless steels are generally known as important class of alloys. Their importance is proved in the plenitude of applications that depend on their use. From low-end applications, like furniture and cooking tools, to very complicated ones, such as space vehicles [1], the use of stainless steels is essential.

The word 'steel' means that iron which is regarded as the bulk of the material, while the use of the adjective 'stainless' indicates absence of rusting, staining or corroding in environments where 'normal' steels are. In order to assign stainless characteristic to steels, chromium must be added to at least 11 wt%. At this level of Cr, self-healing chromium oxide can form on the steel surface in relatively benign environments. However, to guard against rusting and pitting in more adverse environments (for instance, polluted environments or moist atmospheres) or in the presence of specific elements like carbon, higher Cr or Ni contents must be added.

Modern stainless steels also contain a host of other alloying elements whose presence improves specific properties, while the Fe–Cr system forms the basis. Mo is added to enhance resistance against pitting and Ni is added to obtain γ , for example. It is general for some grades, for instance, the superferritics and superaustenitics, to contain quite generous amounts of these alloying elements. When the contents of Cr and Ni are added in considerable amounts, the resulting alloys are called heat-resisting alloy. Although contents of alloying elements can be present in stainless steels, their total fraction is usually kept below the iron content, in order to maintain the resulting alloy to be steel.

There are three conventional types of microstructures in stainless steels, i.e., austenitic, ferritic and martensitic. These microstructures can be obtained by appropriate controlling of steel chemistry. Out of these three most conventional microstructures, stainless steels can be categorized into several main classes [1, 2]. These are (1) austenitic stainless steels, (2) ferritic stainless steels, (3) martensitic stainless steels, (4) duplex stainless steels (DSS), (5) Mn-N substituted austenitic stainless steels and (6) precipitation hardening stainless steels. The respective classes of stainless steels have different properties and purposes. For example, fully austenitic stainless steels are not magnetic material, but their ferritic and martensitic counterparts have ferromagnetism. The different properties of the various stainless steels have

been researched extensively for a very long time and thus are very well reported in many literatures. The early handbooks for stainless steels, which include a series of informative articles, are very helpful sources on this topic [3].

Although they are considered as an 'old' alloy system (the history of stainless steels traces back to about the early 1900s) and very extensive researches have been carried out to understand them, stainless steels have never been sidelined until recent date in materials science. The fact that a search in popular databases (such as the Science Citation Index Expanded and the ScienceDirect) with the keywords 'stainless steel' easily turns up thousands of recent articles can be cogent evidence for this statement. The absolute volume of recent publications about stainless steels authentically shows that there are still a lot of unresolved problems and unknown territories in stainless steels.

Some of the recent articles have wrapped up the unfinished researches carried out by early workers. For example, while the γ phase of stainless steel was discovered and characterized for a long time ago, a model for formation of γ phase had not been formally formulated until recently [4]. Several problems which are considered to be well settled long before have been examined again in a lot of recent publications and fresh views have been put

forward. For example, strain induced martensite in metastable austenitic stainless steels is commonly believed to be possible via the formation of the ϵ martensite. However, this is thought to be improbable by Hedstrom et al. [5] in their recent works. Another good example is the effect of nitrogen on stacking fault energy (SFE). A number of early researches concluded that N monotonously suppressed SFE in austenitic stainless steels as their content increased, however, recent studies have unambiguously proved that the effect of N on SFE is rather complicated and quite far from being monotonous [6, 7]. Of course, recent workers have been able to make new discoveries with an arsenal of sophisticated technologies which were unavailable to early researchers. For example, using 3DXRD, Hedstrom et al. [8] have been able to investigate in-situ the γ - ϵ transformation of respective grains in a polycrystalline AISI301 stainless steel and shown that this transformation occurs in a quite localized manner. And recently, new kinds of stainless steels offering very superior properties have been developed [9]. A variety of methods (for instance, using very severe plastic deformations) for fabricating stainless steels of grain sizes in the nanometer scale have also been recently demonstrated. Transmission electron microscopes (TEM) of higher resolution have enabled researchers to better characterize the evolution of microstructure during quite severe plastic deformations (For example, refer to the series of recent works by Belyakov et al. [10-13]). Several recent publications seem to have settled controversies, such as the main mechanism responsible for

causing hydrogen embrittlement. For example, several recent researches have convincingly demonstrated that hydrogen-enhanced localized plasticity (HELP) is the fundamental mechanism for causing hydrogen embrittlement of austenitic stainless steels [14].

And a large portion of recent researches has been devoted to fabricating DSS and their various properties. Even though DSS are certainly not fresh inventions, systematic and large scale researches on them seems to increase its ascendancy only since the 1990s, as proved by the publications of some frequently cited monographs [15, 16] and a series of international conferences that are dedicated specifically to duplex stainless. In 1998, even it was not a long time ago, researches aimed at suggesting the guidelines on alloy design for high nitrogen DSS were still encountered in the literature [17]. A few fresh approaches for introducing and analyzing DSS were only published after 2000s.

1.2 Duplex stainless steel

The superplasticity of DSS was discovered in the 1960s [18-20]. Since then, different mechanisms for the superplastic behavior of DSS have been suggested. The early studies and most recent ones [21-23] have generally attributed superplasticity to sliding of grain boundaries. Later researches by Maehara et al. [24-26] proposed that it was the balance between dynamic continuous recrystallization (often referred to simply as dynamic recrystallization in several publications) and strain hardening in the neighborhood of the softer phase that led to superplasticity of DSS, not grain sliding. On the other hand, Tsuzaki et al. [27] argued that the role of dynamic continuous recrystallization during superplastic deformation was to maintain a fine grained microstructure by slowing down the grain growth of the softer phase, such that grain sliding could take place during superplastic deformation.

Some of the recent researches on the superplasticity of DSS have been devoted to explaining further the mechanism which is involved. In a study by Han and Hong [28] on a DSS which has ($\gamma + \sigma$) microstructure, it has been concluded that superplasticity is caused by dynamic recrystallization assisted grain sliding. However, dynamic continuous recrystallization, in addition to generating a fine grained, equiaxed microstructure at the initial stage, also transforms the low-angle grain boundaries into high-angle boundaries, which

expedite grain sliding.

Miyamoto et al. [29], emphasizing the importance of the different sliding rates of various types of grain boundaries [29, 30], have gone further to introduce the concept of cooperative interphase grain boundary sliding in DSS having the α - γ microstructure. According to this mechanism, a large amount of sliding involving partial grains takes place cooperatively on preferred planes of α/γ grain boundaries [29]. The interphase grain sliding discontinues when the sliding is obstructed by other grains. And grain sliding restarts when the obstructing grains cannot hold the sliding in place or when the other planes appropriate for sliding kick into action [29]. The removal of the obstruction to sliding by other grains involves the sliding of γ/γ and α/α homophase grain boundaries. The homophase boundaries slide quite slower than the α/γ heterophase grain boundaries [29, 30]. The significance of the heterophase grain boundaries to superplasticity has also been realized by Nieh et al. [30], who reported that superplastic strain rate can be increased if total fraction of the heterophase boundaries is increased [30]. Nevertheless, if the inhomogeneous deformation caused by the different sliding rates of the various types of boundaries cannot be correctly accommodated, then cavities will be generated, especially in grain triple junctions [20] and the α/γ heterophase grain boundaries [30].

As previously stated, the dynamic continuous recrystallization of the softer phase in the DSS plays a very significant role in superplastic deformation. The increase of misorientation in grain boundary, which is critical to superplasticity, has been closely examined during dynamic recrystallization by Tsuzaki et al. [31]. These researchers have found that at the initial stage of superplastic deformation, strain was developed mainly through general intragranular slips, rather than grain boundary sliding, since the misorientations are not sufficiently concentrated among the softer phase. Consequently, the strain incompatibility between the hard phase and the soft phase of the duplex structure like DSS is accommodated by intragranular slips. The absorption of concentrated dislocations into grain boundaries will distort the crystal orientation and gradually increase the misorientations around grain boundaries. Finally, the original low angles boundaries become high angle boundaries which are able to support grain boundary sliding [31-33]. Thus, the increase in misorientation can take place without grain boundary sliding. For this reason, Tsuzaki et al. [31] have suggested that the term 'dynamic continuous recrystallization' is a misnomer, because the process is in fact 'recovery'. The importance of intragranular slips is also reported by Song and Bate [34].

Accordingly, the respective different mechanical properties and the elastic/plastic anisotropy of each constituent phase may lead to two

kinds of microstresses in the duplex steel, including the phase stress and intergranular stress (or grain-orientation-dependent stress). The former is produced by the phase-to-phase interactions and the latter is due to the grain-to-grain interactions. The presence of the internal microstresses is closely related to the evolution of the macrostress subjected in service. Both macrostresses and microstresses greatly affect the performance of engineering components. Therefore, in recent years, great effort has been made to figure out relationship between small scale deformation of respective phases in DSS and macroscopic deformation behavior.

1.3 Deformation analysis for duplex stainless steel

1.3.1 Neutron diffraction analysis

The neutron diffraction technique is a well-established tool for studying micromechanical behavior of materials [35, 36]. Because of the selective nature of diffraction techniques, the elastic (lattice) strain of the specified grain populations of each phase with their (hkl) crystal planes along the macroscopic specimen directions may be experimentally determined, which enables us to separate the elastic response of different phases during deformation. On the other hand, the self-consistent models prove to be effective in describing the anisotropic micromechanical behaviors of single-phase materials during elastic and plastic deformation [37, 38]. For dual phase materials, however, the interactions of grain-to-grain and phase-to-phase may occur simultaneously during deformation, which requires a complicated model for describing the micromechanical behavior [39, 40]. In the present work, based on time-of-flight (TOF) neutron diffraction experiments, different lattice strains in DSS during uniaxial tensile deformation were measured. Since multiple reflections of different phases had been captured simultaneously, material parameters required for the numerical modeling of heterogeneous stresses within the material can be determined from the experimental lattice strain distributions.

In the present studies, experiments combining incremental tensile testing with in-situ neutron diffraction measurement were performed for the Fe–Cr–Ni alloys in order to characterize elasto-plastic deformation behavior of α - γ dual-phase alloys. The geometric arrangement of the in-situ strain measuring system is displayed in Fig. 1.1. Both slits in Fig. 1.1 were of the same width. The specimens were deformed in tension in a step-by-step. The overall specimen strains were measured by means of strain gauges glued on the specimen surface. From here on, they are called macroscopic strains.

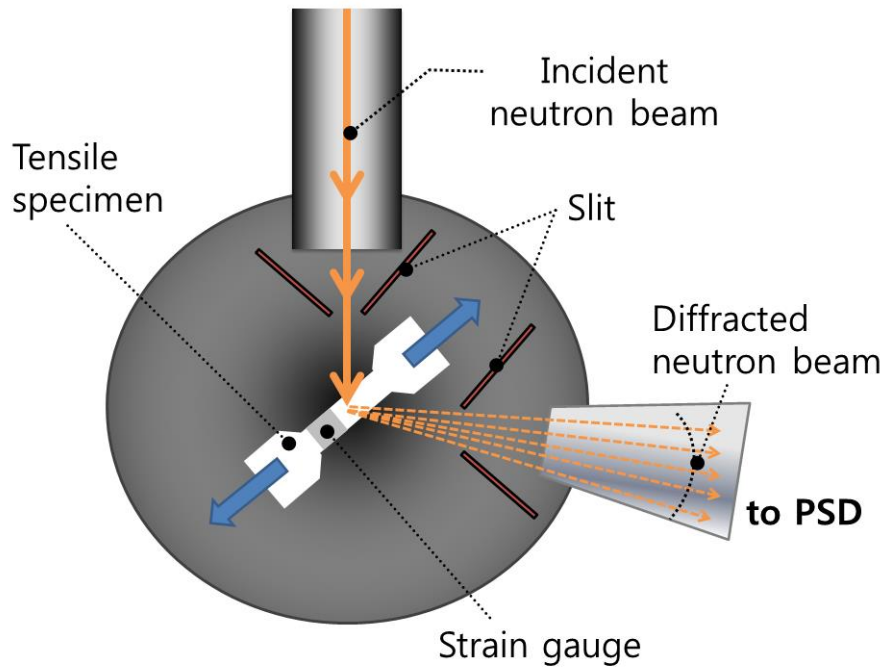


Figure 1.1 Schematic image of the in-situ stress measuring system by neutron diffraction.

The monochromatic neutrons of wavelength λ selected by a crystal monochromator are incident to a sampling gauge volume which is adjusted by a set of absorbing masks in the incident and diffracted beams. Following the Bragg law [41], the neutrons are then diffracted by a family of lattice planes (hkl) with spacing d_{hkl} at an angle of $2\theta_{hkl}$:

$$\lambda = 2d_{hkl} \sin \theta_{hkl} \quad (1-1)$$

Differentiating equation (1-1) gives a relation for determining a relative lattice strain ε_{hkl} along the normal direction to the (hkl) plane, i.e. parallel to the scattering vector,

$$\varepsilon_{hkl} = \frac{d_{hkl} - d_{hkl}^0}{d_{hkl}^0} = -\cot \theta_{hkl} \Delta \theta_{hkl} \quad (1-2)$$

where d_{hkl} , d_{hkl}^0 and θ_{hkl} are the measured lattice plane spacing, stress-free lattice spacing and the Bragg angle, respectively. The ε_{hkl} determination is based on the measurement of angular deviation of the profile $\Delta \theta_{hkl}$ with respect to the stress-free state. In the present study, d_{hkl}^0 for α and γ phase were determined by measurement of reference α and the γ single-phase alloy before deformation, respectively.

In the case of a diffractometer with a sufficiently high instrumental resolution, a parameter of microstrain can be evaluated from the shape of the

diffraction profile by using an appropriate method for the profile analysis [42]. Such an analysis includes a correction for the instrumental resolution and a separation of two main contributions to the profile broadening, microstrain and size of mosaic blocks. In the present tensile deformation, the change in block size is caused by dislocation cell formation while that of microstrain by the increase of lattice defects like dislocations. Since the resolution of the diffractometer used is optimized for a selected lattice plane spacing ($d = 2 \text{ \AA}$ typically), we are restricted to investigate a narrow band of the angular spectra consisting usually of one or two diffraction peaks. Recently, a transformed model for fitting some elements of an integral breadth technique has been proposed [43]. The modeling is performed in reciprocal space, and the microstrain contribution is treated according to the simple Keijser approach [44, 45]. The input instrumental resolution function is usually approximated by a measured diffraction profile of a well-annealed standard specimen where the broadening due to size contribution is negligible.

The effect of peak broadening is treated in terms of an integral breadth method. Here the basic assumption is that a sample broadened profile, i.e. a measured profile which is deconvoluted with the instrument function, can be described by the convolution of a Gauss and a Cauchy function:

$$I(x) = I(0) \exp \left[-\pi \frac{x^2}{\beta_G^2} \right] \otimes \left[\frac{1}{\beta_C^2 / \pi^2 + x^2} \right] \quad (1-3)$$

where $x = 2 \sin \theta/\lambda$ and β_C and β_G are constant parameters of the Cauchy and Gauss function, respectively. The Keijser method assumes that the Cauchy function reflects block size while the Gauss function reflects microstrain. The block size and the microstrain contributions are then related to the parameters of the Cauchy and the Gauss function by

$$D_{eff} = \frac{1}{\beta_C} \quad (1-4)$$

and

$$\langle \xi^2 \rangle^{1/2} = \left(\frac{2}{\pi} \right)^{1/2} \beta_G d_{hkl} / 2 \quad (1-5)$$

respectively, where D_{eff} is the effective dimension of coherently diffracting blocks and ξ is the microstrain. For instance, the root-mean-square of ξ , i.e. $\langle \xi^2 \rangle^{1/2}$, could be interpreted to be proportional to the square root of dislocation density ($\sqrt{\rho}$) by a dislocation density model [46] as follows:

$$\rho = \frac{k \langle \xi^2 \rangle}{F b^2} \quad (1-6)$$

where b , F and k represent the magnitude of Burgers vector, the factor describing interaction between dislocations, and a constant, respectively. In the present case, researchers assume $F = 1$, $k = 16.1$ for FCC crystal with a

Burgers vector along $\langle 110 \rangle$, and $k = 14.4$ for BCC with a Burgers vector along $\langle 111 \rangle$ according to Ref. [46].

1.3.2 EBSD (Texture) base analysis

With the automation of the electron backscatter diffraction (EBSD) technique, EBSD systems have become commonplace in microscopy facilities within materials science and geology research laboratories all around the world. The capabilities of EBSD to aid the scientist in understanding the crystallographic aspects of microstructures have been well used in a wide variety of materials and applications. However, another potential use of EBSD is in quantifying strain. In recent years, the electron back-scattering diffraction (EBSD) technique has been applied toward investigations of the microstructural-features-related deformation process on materials subjected to various deformation modes [47-49]. When this technique is applied for characterizing evolution of microstructures during in-situ loading [50], detailed information regarding the emergence of slip bands, the evolution of grain boundary distributions, as well as the change in grain orientation could be traced in the real specimen space for specimens under the strain/stress field. Thus, the deformation mechanism that is dependent on the microstructural features could be deduced from robust experimental observations. Fréchar et al. [51], who made a complete identification of slip systems in a γ - α stainless steel by combining atomic force microscopy (AFM) and EBSD, have suggested that the plastic deformation of ferritic grains is triggered by dislocation accumulations in the neighboring austenitic grains. As for γ ,

plastic activity is considered to depend mainly on its intrinsic glide and orientation characteristics [52]. Consistent results could be found in other study of localized strains in duplex steel by transmission electron microscopy (TEM) [53]. Meanwhile, some efforts have been made to develop numerical and analytical models for simulating the anisotropic micromechanical behaviors of duplex materials. Those numerical simulations or analytical models mainly depend on the distributions of lattice strains in the reciprocal space that were obtained from neutron diffraction [54-58] or synchrotron based X-ray diffraction [59, 60]. In comparison with the modeling for single-phase materials, both interactions of grain-to-grain within one phase and phase-to-phase have to be considered for duplex materials [40], aiming at the accurate evaluation and reliable prediction of mechanical performances for such materials. In recent research [61], a two-phase visco-plastic self-consistent (VPSC) model has been developed for simulating the elastic and plastic interactions among grains with various orientations in two phases. The in-situ neutron diffraction experiments were used to obtain materials parameters required for numerical simulations. In spite of the above-mentioned studies, the direct in-situ experimental efforts to study the deformation behavior with a resolution of submicrometer, particularly for elucidating the stress heterogeneity under the applied stress field, through combining the EBSD experimental observation with the numerical simulations, are still lacking. The present work focuses on the evolution of

grain orientation-dependent strains and strain compatibility between two phases, which were influenced by the starting microstructure of the duplex steel and lately affected again the development of deformation microstructures in the late stage of deformation. The in-situ tensile EBSD experiments will be conducted also for characterizing the changes in microstructures at different stages of deformation.

In EBSD, a fine beam of electrons is focused sequentially on a grid of points on the surface of a crystalline material. Diffraction of the electrons backscattered from the top 10 to 100 nm [62, 63] forms patterns from which the crystallographic orientation of the material under each spot can be determined. The generation and accumulation of dislocations during metal's plastic deformation results in local changes to the lattice orientation and plastic strain can be estimated by measuring these local orientation differences (misorientations). The dislocations which contribute to the lattice rotations are known as geometrically necessary dislocations (GNDs) [64]. Plastic strain also degrades the quality of the diffraction patterns and this effect has also been used to estimate plastic strain e.g., [65, 66] but this approach suffers from the disadvantage that many other factors such as surface contamination, surface preparation, pattern overlap close to grain boundaries, compositional variations and the particular crystallographic planes contributing to an individual pattern [67] affect the pattern quality too and may give misleading

results. The accuracy of strain assessment by measuring local misorientations clearly depends on the accuracy with which each individual orientation can be determined which in turn depends on the microscope operating conditions, the pattern acquisition parameters and the condition of the surface [68]. The use of various EBSD metrics for the analysis of plastic strain has recently been reviewed [69] but there is little published research concerning the behavior of these metrics after deformation at different temperatures, strain rates and deformation mode. Most study in this area has focused on the development of calibration curves for solution-treated materials [65, 70-75] based on room-temperature deformation. The use of such curves in assessing plastic strain developed at high temperatures is limited by differences in the deformation mechanisms operating at different temperatures and by the effects of microstructural changes occurring during high-temperature deformation. These include the development of intragranular and intergranular precipitation and changes in the grain size distribution which alter the deformation behavior from that of the SA material. The influence of aging on the “low angle boundary fraction” (LABF)[69] EBSD metric has been demonstrated in a ferritic steel[76] which showed LABF in unstrained P91 steels to vary with aging time at 923 K(650°C), but there have been no systematic studies on aged austenitic steel investigating the behavior of the various metrics after different deformations. The metric integrated angular misorientation density (IMD), which is based on spatially correlated misorientations, has been found

to have a close to linear relationship with applied plastic strain under both compressive and tensile deformations at room temperature, although the two different deformation modes gave different IMD values at any given strain level [77]. There has been no examination of whether the observed nonlinear behavior of other metrics e.g., [78] with increasing strain beyond 0.15 to 0.2 are the result of a change in the underlying dislocation behavior or result from the way each metric is defined and calculated. There is little literature on the effects of deformation strain rate on EBSD. This has been addressed indirectly [72, 78, 79] by comparing results obtained from uniaxial tensile and from creep tests but there have been no systematic studies in which strain rate was the only variable. Several studies [65, 72, 80-82] have demonstrated good correlation between hardness and different EBSD metrics, implying a relationship between the metrics and the overall dislocation density rather than its relating solely to the density of GNDs. Thus hardness can provide a comparison for EBSD measurements of strain, although with the reservation that the volume of the strain fields sampled by the two techniques differs by several orders of magnitude. In the current study, the EBSD metrics investigated were kernel averaging misorientation (KAM), grain average misorientation (GAM), grain orientation spread (GOS) and low angle misorientation fraction (LAMF). The sensitivity of the metrics is examined under different deformation conditions and through a statistical approach adopted to determine the nature of their variations with the applied plastic

strain. As shown in Fig. 1.2, Yoda et al. reported the value of Grain Average Misorientation (GAM) which showed the average misorientation for the whole observed area including over several dozen grains, was a very useful parameter for quantifying the microstructural change as either the plastic or creep strain increased [72]. And KAM even occasionally used to evaluate and to map the local plastic strain as seen in Fig. 1.3 [83].

However, Since EBSD measurements are made from a layer of material less than 100 nm from the surface, this can only be typical of the bulk strain if the local misorientations in this layer are representative of those below. Although dislocation dynamics simulations for Cu suggest that dislocations relax within 65 nm of a free surface, comparisons between EBSD measurements and those from X-ray micro diffraction (which probed to a depth $\sim 2\mu\text{m}$) on a Cu single crystal deformed to a macroscopic strain of about 0.1 showed very similar overall lattice rotations measured by each technique[83] which gives confidence that, although it is a surface technique, EBSD can give reliable information about deformation in the bulk.

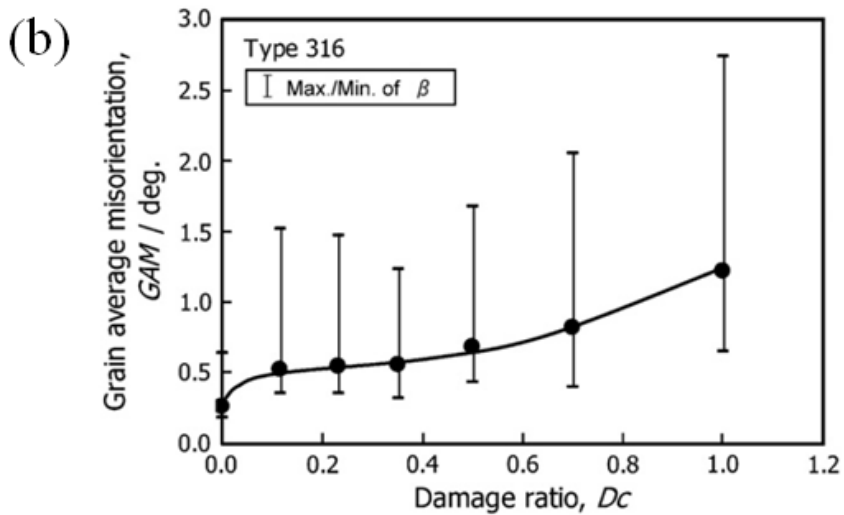
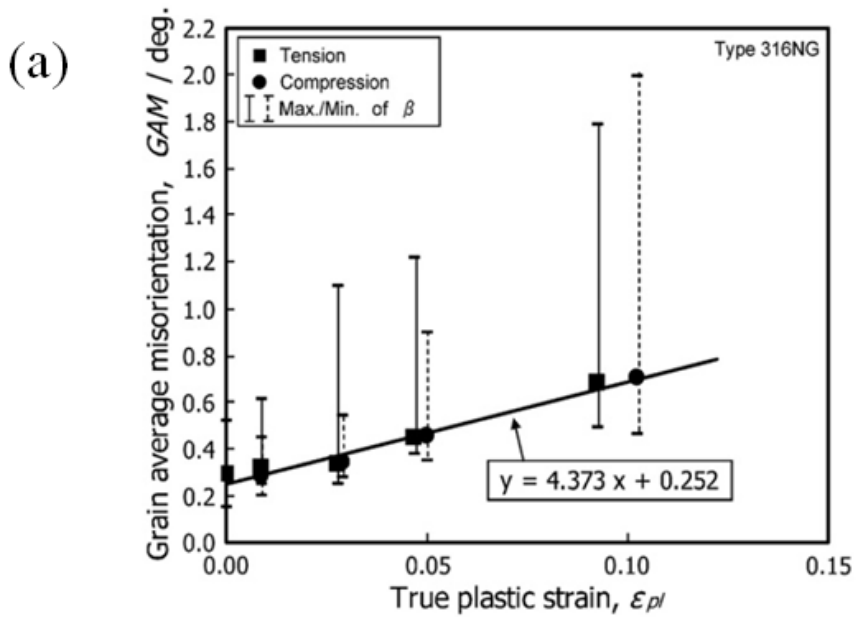


Figure 1.2 Change in the grain average misorientation (GAM) (a) with plastic strain in the tensile/compression specimens of the type 316NG and (b) with creep damage ratio in the specimens of the type 316 stainless steel creep tested at 600 °C [72].

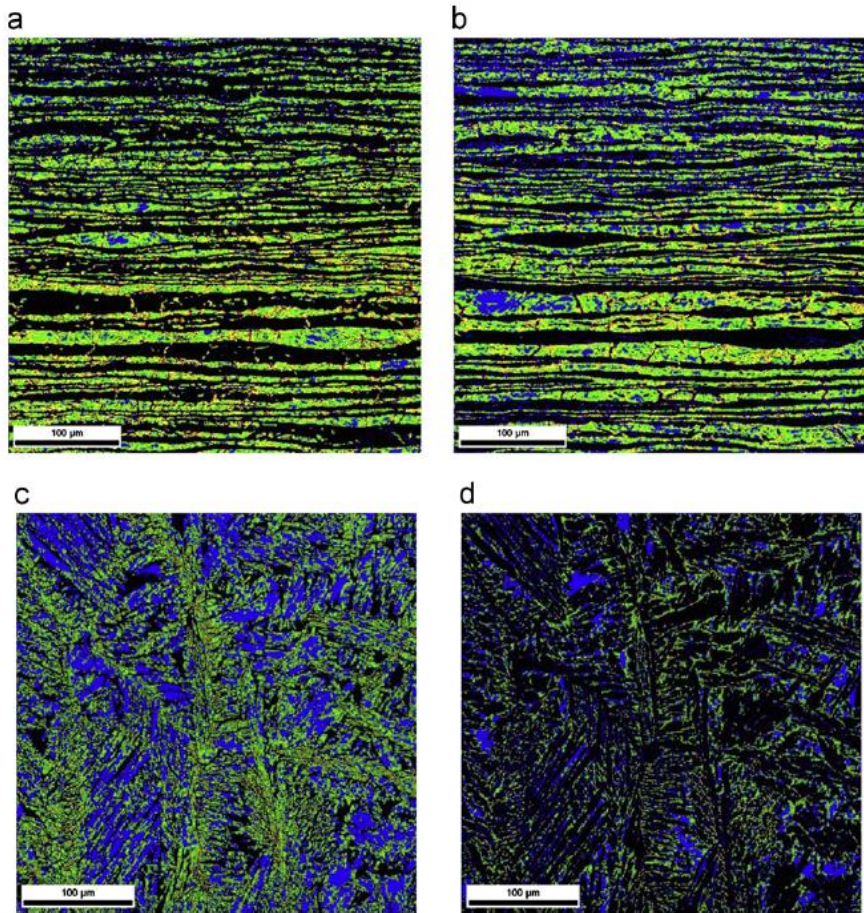


Figure 1.3 KAM maps for evaluating local strain of weld joint: (a)austenite and (b)ferrite in the base metal, (c)austenite and (d)ferrite in the weld metal [83].

1.3.3 Digital image base analysis

As previously stated, strain measurements in DSS have already been studied by various methods [85-87]. However, quantitative data about the strain partitioning between α and γ and strain heterogeneities induced by the microstructure are limited to preliminary experimental attempts [88-90] while being essential to unravel the origin of the damage mechanisms leading to the edge cracking process. Complex phenomena take place during hot forming of metals, especially when involving two phases with different strengths. Indeed, in addition to the overall stress and strain gradients, the local strain can be highly heterogeneous. A first method to quantitatively determine the strain partitioning has been proposed by Unckel [91] and used by Duprez et al. and Al-Jouni [92, 93]. These authors estimated the strain differences between the constituent phases by measuring the evolution of the dimensions of the grains. Other investigators have used hardness [94, 95] and residual stress measurements [86] to probe the relative strength of constitutive phases. In order to quantify the stress and strain partitioning in multiphase alloys, important research efforts have been recently made to obtain more accurate results. Grid techniques are often used in the context of metal forming, see examples in [96-98]. Microgrid techniques combined with SEM in-situ mechanical testing and automated image analysis has been used for many years for the investigation of deformation mechanisms at the micro-scale [85,

99-105]. One advantage of the microgrid techniques is that they enable simultaneous observation of the microstructure and evaluation of the local strain field at the surface of a sample under loading. However, until recently, microgrid techniques could not be applied to deformation conditions representative of a hot rolling process. With the method initiated by Pinna et al. [88] and further developed by Hernandez [89] and Rupin [90], local deformation in steel samples can be measured at temperatures up to 1050°C. The latter technique has been adopted in this present work to investigate strain partitioning in DSS. Note that strain partitioning can also be evaluated directly on the deformed microstructure if the contrast between the phases is large enough [106]. Interphase strain heterogeneities can also be mapped on materials on which a microgrid-type of marking is not possible when a sufficient intraphase image contrast is available, induced by a natural heterogeneity at a lower scale, an appropriate surface preparation or the use of specific imaging conditions [107]. However, because of the too low intraphase contrast in duplex steels and its potential strong evolution during hot deformation such grid-less techniques are not applicable for high temperature investigations.

Thus, a microgrid technique has been developed for the analysis of the micro-scale strain distribution between α and γ into DSS. The local strain is measured by micro-extensometry using square microgrids engraved on flat

specimens by electro lithography. An electron-based lithography technique for manufacturing microgrids, based on the procedure developed by Pinna et al. [88], has been used to generate microgrids on the microstructure of interest. Small rectangular volumes with dimensions were machined from the heat treated material. The specimens will microgrid process is adapted from the procedure described in [99] by replacing the metal sputtering and evaporation step by an appropriate etching of the sample. It is schematically summarized on Fig. 1.4.

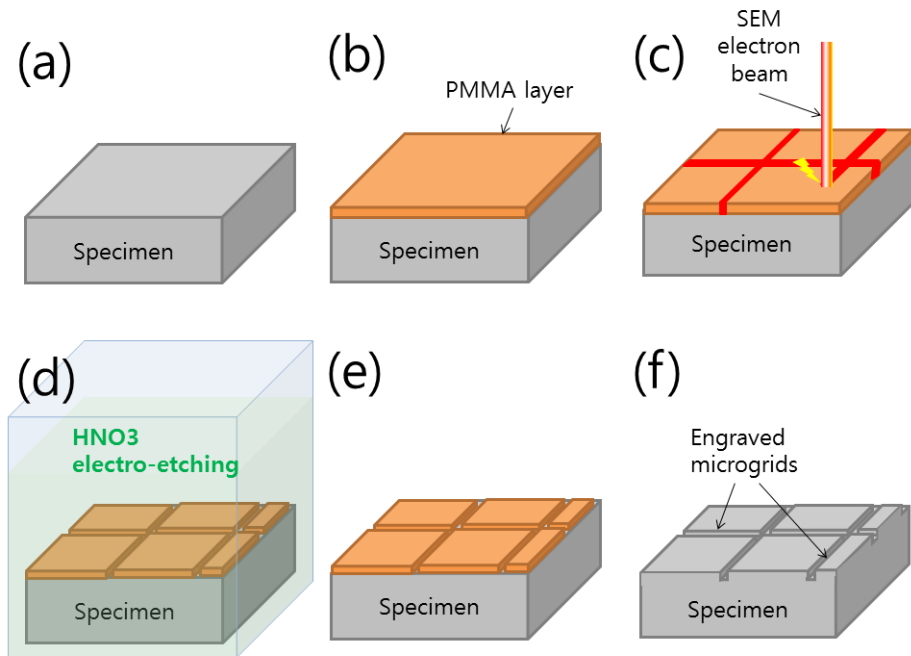


Figure 1.4 Fabrication of the microgrids; (a) polishing and electro-etching; (b) coating with an electro-sensitive polymer; (c) irradiation of the resin with the electron beam; (d) dissolution of the irradiated polymer; (e) engraving by electro-etching; (f) dissolution of the remaining polymer [85].

The sample with microgrids on the surface and preliminary imaged with high definition scanning electron microscope (SEM) is deformed. After deformation, the sample is extracted from the distorted block and the surface is again analyzed by SEM and image processing to determine the strain field. The comparison between the undeformed and the deformed state allows a quantitative characterization of the strain distribution. A fully automated digital image correlation analysis was not possible because of the presence of many small areas where the microgrids were damaged or exhibited too large variation of the local image contrast between the reference and the undeformed configuration. The local reliefs induced by the out-of-plane displacement as well as the slight oxidation which can occur during the thermomechanical process are responsible for the variations of the local image contrast. In these areas, the grey level conservation principle on which correlation technique relies is no longer valid. That is why the microgrid intersections were for the majority of them manually located using the software CMV developed at the laboratory LMS. This software combines DIC-based automatic pattern matching algorithms with a graphical user interface which allows a reasonably accurate and fast mouse-based manual positioning of point. Automatic procedures are used in areas where image characteristics are compatible with a direct application of these procedures; DIC principles can also be used to relocate more accurately points which have been approximately set manually. This software has originally been developed

for the work described in [88] to process the strongly deformed SEM images obtained in that context, which could not be fully processed with automatic DIC routines [105]. Various developments have been added since then various applications [90, 103, 104, 107].

This software provides the in-plane displacement components of each microgrid intersection, from which the inplane components of the local, per-phase average or overall transformation gradient tensor \bar{F} can be calculated. The local transformation gradient at a given grid intersection p is computed as the average of the true local gradient over a small surface S^p around the grid intersection. The chosen surface is a polygonal surface where vertices are neighbors of the considered grid intersection. Let x be the position of a grid intersection in the deformed configuration, Σ^p the boundary of S^p and ν^p its normal. The local transformation gradient can then be computed using a contour integral:

$$F^p = \frac{1}{S^p} \int_{\Sigma^p} x \otimes \nu^p dl \quad (1-7)$$

$\nu^p dl$ is constant on a segment of Σ^p and a local linear interpolation between intersections is assumed. Several choices are possible for the polygonal surface S^p , see [99]. In the present study, a four-neighbor scheme is used, resulting in a gage length for local strain evaluations of $\sqrt{2}$ grid intersections.

The procedure to compute local gradients as averages over a small domain around the considered grid intersection can be used to compute perphase average gradients using the polygonal lines defined as Fig. 1.5.

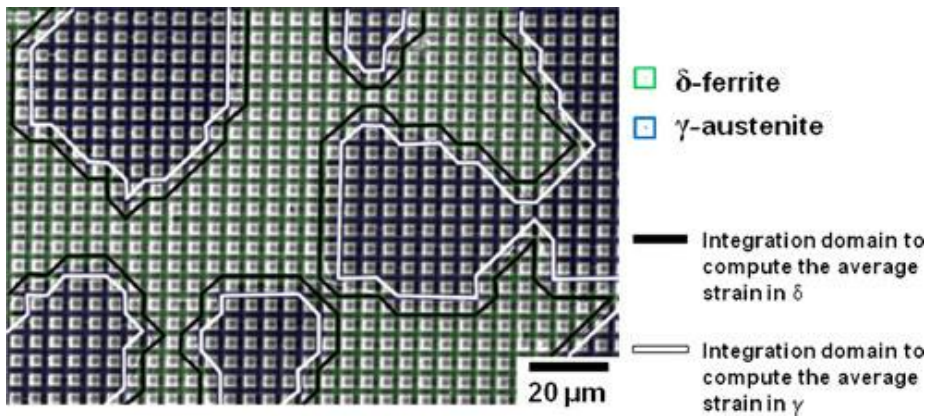


Figure 1.5 Example of a correspondence between the microgrids and the underlying microstructure with phase boundaries [108].

The out-of-plane displacement cannot be measured directly. Its variations with the in-plane coordinates are assumed to be negligible for the computation of the inplane components of the logarithmic strain tensor "log. This assumption is equivalent to assume that the surface of observation is a principal plane of the strain tensor. It seems appropriate from a macroscopic point of view since plane strain conditions are globally enforced at the location of the plane of interest. As a first approximation, it is also reasonable for the per-phase average strain since, on average, the deformation state of a phase keeps the same symmetry as the macroscopic deformation. Indeed, the local phase distribution on a representative domain is statistically symmetric with respect to the plane of observation. This assumption is probably not justified locally at a particular point within each phase, since a three-dimensional state of deformation develops because of the heterogeneity of the microstructure and the anisotropy of the plastic deformation at the grain scale.

A representative area was selected from the large SEM picture of the deformed microgrids, and the displacements of the grid intersections with respect to the undeformed configuration were used to calculate the distribution of the local strain components and of the Von Mises equivalent strain. The calculated data were represented as color maps corresponding to different levels of strain. The corresponding microstructure, in the undeformed configuration, was edited to extract the interphase boundaries.

The boundaries were then superimposed to the color maps in order to reveal clearly the link with the background microstructure. The strain maps are shown as Fig. 1.6. The strain is heterogeneously distributed with a strong localization of the deformation, in the form of shear bands located within the α and at the vicinity of the γ/α interphase boundaries. These strain maps provide useful informations about the rheology of the phases as well as about the local conditions at the origin of the damage process.

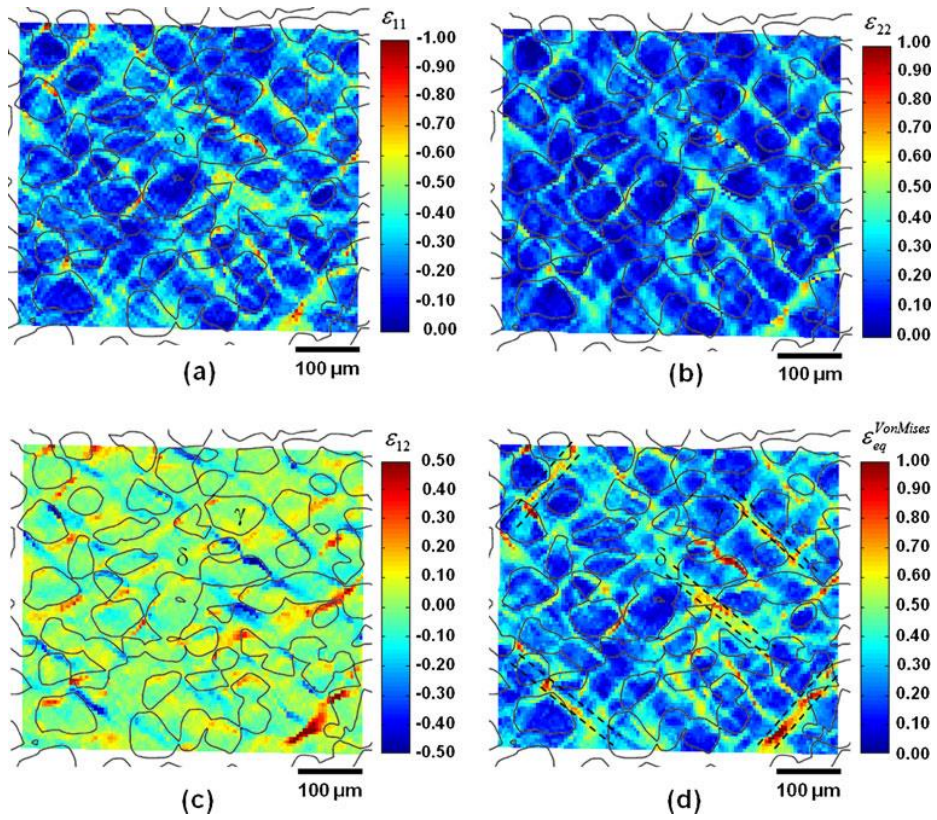


Figure 1.6 Logarithmic strain distribution maps after plane strain compression; (a) ϵ_{11} ; (b) ϵ_{22} ; (c) ϵ_{12} ; (d) ϵ_{eq} ; the strain maps are superimposed with the undeformed microstructure; the compression axis corresponds to the vertical axis [108].

1.4 Issues of existing deformation analysis for DSS and motivations for research

As has been previously stated, there are three conventional methods to analyze relationship between small scale deformation of respective phases in DSS and macroscopic mechanical behavior on deformation. These are (1) neutron diffraction analysis, (2) EBSD (texture) base analysis and (3) digital image base analysis. Many researchers reported deformation behavior of DSS by using these methods and showed a lot of great results [108-112]. However, the respective analysis methods also have been pointed out several disadvantages.

In case of neutron diffraction base deformation analysis for DSS, lattice plane strain of various lattice planes of α and γ were determined as a function of the applied true stress during uniaxial tension to define yield stress. However, the lattice strain can indicate only elastic strain [37, 41]. Information of plastic deformation cannot be measured directly by neutron diffraction analysis. Thus plastic behavior is estimated indirectly by tracing changes of lattice strain during deformation [35, 37, 61, 111]. However, for DSS, it is difficult to separate the individual contribution of each phase from macroscopic applied stress or strain, and state of stress-strain is generally assumed as isostress. The critical issue arises in this procedure. The respective

phases, α and γ , have different mechanical properties and response to stress or strain. Thus in DSS, in a greater or less, strain partitioning between α and γ necessarily occurs during deformation [35, 61, 111, 112]. Consequently, if yield stress or other specific stress state is defined assuming isostress state, it can involve critical error because of disregarding strain partitioning effect. And in-situ neutron diffraction method collects diffracted neutron beam with specific intervals of stress or strain [113]. Thus specific stress states can't be measured precisely by this method since there is a limitation in the step for the static load control during in-situ neutron diffraction. Moreover, neutron diffraction has bad accessibility because size of equipment is quite huge and there are few locations to use it. For these reasons, we want to measure precise yielding behavior of respective phases in DSS by more simple method. Efforts for this motivation are stated in detail at Part I of this article under the title of "Investigation of yielding behavior of duplex stainless steel by nanoindentation, EBSD and in-situ neutron diffraction".

Not only neutron diffraction analysis, EBSD base method and digital image base method also have some issues for deformation analysis of DSS. In EBSD base deformation analysis, crystal orientation change of respective phases during macroscopic deformation is measured. And the phase which has intensely distorted texture regards as severely deformed phase, since recent researches reported that value some indicators of misorientation (ex.

KAM, GAM, or LAMF) become greater when deformation becomes more severe, statistically [47, 52, 67, 72, 110]. However, these results cannot directly interpret like value of local metric misorientation regard as amount of local deformation. Until a recent date, relationship between strain and misorientation is not investigated clearly. Thus it is dangerous to directly define deformation by orientational information without additional detailed investigation about relationship between strain and misorientation.

Contrastively, precise quantitative strain of respective phases and grains are measured directly by digital image base deformation analysis [108]. The strain field of deformed specimen can be calculated by comparing captured digital images during deformation. But with this method, phase/grain boundaries cannot be identified clearly because they are identified by etched surface morphology. Phase/grain boundaries of specimen reveal faintly by electro-chemical etching. In addition, micro grids for strain calculation disturb identifying the boundaries [86]. Thus it is quite difficult to analyze deformation behavior of each individual phase with this method. However, in order to analyze complex deformation of DSS, accurate quantitative local strain and precise phase/grain information are both necessary. Finally, we thought that they can be measured together if digital image base analysis can be supported by EBSD technique. Thus EBSD combined digital image base deformation analysis method was developed. In addition, relation between

local strain and misorientation was investigated to verify texture base deformation analysis. We expect this approaching can compensate the defect of both EBSD base deformation analysis and digital image base analysis. Before applying this technique to DSS, experimental/analytical techniques for this method were developed by using pure copper specimen. The details for this research are stated at Part II of this article under the title of “Investigation of correlation between strain and crystal orientation by EBSD supported DIC”.

1.5 References

- [1] R.A. Lula, J.G. Parr, *Stainless steel*, American Society for Metals, 1986.
- [2] J. Beddoes, J.G. Parr, *Introduction to Stainless Steels*, ASM International, 1999.
- [3] D. Peckner, I.M. Bernstein, *Handbook of Stainless Steels*, McGraw-Hill, 1977.
- [4] A. Mateo, L. Llanes, M. Anglada, A. Redjaimia, G. Metauer, *Journal of Materials Science*, 32 (1997) 4533-4540.
- [5] P. Hedstrom, U. Lienert, J. Almer, M. Oden, *Scripta Mater*, 56 (2007) 213-216.
- [6] V.G. Gavriljuk, H. Berns, C. Escher, N.I. Glavatskaya, A. Sozinov, Y.N. Petrov, *Mat Sci Eng a-Struct*, 271 (1999) 14-21.
- [7] I.A. Yakubtsov, A. Ariapour, D.D. Perovic, *Acta Mater*, 47 (1999) 1271-1279.
- [8] P. Hedstrom, U. Lienert, J. Almer, M. Oden, *Mater Lett*, 62 (2008) 338-

340.

[9] Y. Yamamoto, M.P. Brady, Z.P. Lu, P.J. Maziasz, C.T. Liu, B.A. Pint, K.L. More, H.M. Meyer, E.A. Payzant, *Science*, 316 (2007) 433-436.

[10] A. Belyakov, H. Miura, T. Sakai, *Mat Sci Eng a-Struct*, 255 (1998) 139-147.

[11] A. Belyakov, T. Sakai, H. Miura, *Mater T Jim*, 41 (2000) 476-484.

[12] A. Belyakov, T. Sakai, H. Miura, R. Kaibyshev, *Scripta Mater*, 42 (2000) 319-325.

[13] A. Belyakov, T. Sakai, H. Miura, R. Kaibyshev, *Phil Mag Lett*, 80 (2000) 711-718.

[14] S.M. Teus, V.N. Shivanyuk, B.D. Shanina, V.G. Gavriljuk, *Phys Status Solidi A*, 204 (2007) 4249-4258.

[15] V. Gavriljuk, H. Berns, *High Nitrogen Steels: Structure, Properties, Manufacture, Applications*, Springer Berlin Heidelberg, 2013.

[16] U.K. Mudali, B. Raj, *High Nitrogen Steels and Stainless Steels: Manufacturing, Properties and Applications*, Alpha Science International, 2004.

- [17] L. Weber, P.J. Uggowitzer, *Mat Sci Eng a-Struct*, 242 (1998) 222-229.
- [18] Humphrie.Cw, N. Ridley, *Journal of Materials Science*, 9 (1974) 1429-1435.
- [19] R.C. Gibson, H.W. Hayden, J.H. Brophy, *Asm Trans Q*, 60 (1967) 565-&.
- [20] H.W. Hayden, P.D. Goodell, S. Floreen, *Metall Trans*, 3 (1972) 833-&.
- [21] D. PulinoSagradi, A.M.M. Nazar, J.J. Ammann, R.E. Medrano, *Acta Mater*, 45 (1997) 4663-4666.
- [22] J.A. Jimenez, G. Frommeyer, M. Carsi, O.A. Ruano, *Mat Sci Eng a-Struct*, 307 (2001) 134-142.
- [23] R.C. Gibson, H.W. Hayden, J.H. Brophy, *Asm Trans Q*, 61 (1968) 85-&.
- [24] Y. Maehara, Y. Ohmori, *Metall Trans A*, 18 (1987) 663-672.
- [25] Y. Maehara, *T Iron Steel I Jpn*, 27 (1987) 705-712.
- [26] Y. Maehara, *Metall Trans A*, 22 (1991) 1083-1091.
- [27] X. Zhang, A. Misra, H. Wang, M. Nastasi, J.D. Embury, T.E. Mitchell, R.G. Hoagland, J.P. Hirth, *Appl Phys Lett*, 84 (2004) 1096-1098.

- [28] Y.S. Han, S.H. Hong, *Mat Sci Eng a-Struct*, 266 (1999) 276-284.
- [29] H. Miyamoto, T. Mimaki, S. Hashimoto, *Mat Sci Eng a-Struct*, 319 (2001) 779-783.
- [30] T.G. Nieh, D.R. Lesuer, C.K. Syn, *Mat Sci Eng a-Struct*, 202 (1995) 43-51.
- [31] K. Tsuzaki, X.X. Huang, T. Maki, *Acta Mater*, 44 (1996) 4491-4499.
- [32] J.A. Jimenez, F. Carreno, O.A. Ruano, M. Carsi, *Mater Sci Tech Ser*, 15 (1999) 127-131.
- [33] J.L. Song, P.L. Blackwell, *Mater Sci Tech Ser*, 15 (1999) 1285-1292.
- [34] J.L. Song, P.S. Bate, *Acta Mater*, 45 (1997) 2747-2757.
- [35] Y. Tomota, H. Tokuda, Y. Adachi, M. Wakita, N. Minakawa, A. Moriai, Y. Morii, *Acta Mater*, 52 (2004) 5737-5745.
- [36] D.G. Carr, M.I. Ripley, D.W. Brown, S.C. Vogel, T.M. Holden, *Journal of Nuclear Materials*, 359 (2006) 202-207.
- [37] S. Harjo, Y. Tomota, M. Ono, *Acta Mater*, 47 (1998) 353-362.
- [38] I. Karaman, H. Sehitoglu, H.J. Maier, Y.I. Chumlyakov, *Acta Mater*, 49

(2001) 3919-3933.

[39] D. Dye, H.J. Stone, R.C. Reed, *Acta Mater*, 49 (2001) 1271-1283.

[40] A. Baczmanski, C. Braham, *Acta Mater*, 52 (2004) 1133-1142.

[41] G.E. Bacon, *Neutron diffraction*, 3d ed., Clarendon Press, Oxford Eng., 1975.

[42] D. Balzar, *J Res Natl Inst Stan*, 98 (1993) 321-353.

[43] P. Scardi, M. Leoni, R. Delhez, *Journal of Applied Crystallography*, 37 (2004) 381-390.

[44] T.H. de Keijser, J.I. Langford, E.J. Mittemeijer, A.B.P. Vogels, *Journal of Applied Crystallography*, 15 (1982) 308-314.

[45] T. de Keijser, E.J. Mittemeijer, H.C.F. Rozendaal, *Journal of Applied Crystallography*, 16 (1983) 309-316.

[46] G.K. Williamson, R.E. Smallman, *Philos Mag*, 1 (1956) 34-46.

[47] M. Mineur, P. Villechaise, J. Mendez, *Mat Sci Eng a-Struct*, 286 (2000) 257-268.

[48] D. Jorge-Badiola, A. Iza-Mendia, I. Gutierrez, *Mat Sci Eng a-Struct*, 394

(2005) 445-454.

[49] S. Bugat, J. Besson, A.F. Gourgues, F. N'Guyen, A. Pineau, *Mat Sci Eng a-Struct*, 317 (2001) 32-36.

[50] K.K. Park, S.T. Oh, S.M. Baeck, D.I. Kim, J.H. Han, H.N. Han, S.H. Park, C.G. Lee, S.J. Kim, K.H. Oh, in: *Materials Science Forum*, 2002, pp. 571-576.

[51] S. Fréchar, F. Martin, C. Clément, J. Cousty, *Materials Science and Engineering A*, 418 (2006) 312-319.

[52] A. Gironès, P. Villechaise, A. Mateo, M. Anglada, J. Méndez, *Materials Science and Engineering A*, 387-389 (2004) 516-521.

[53] W. Zieliński, W. Światnicki, M. Barstch, U. Messerschmidt, *Materials Chemistry and Physics*, 81 (2003) 476-479.

[54] P. Dawson, D. Boyce, S. MacEwen, R. Rogge, *Metallurgical and Materials Transactions A: Physical Metallurgy and Materials Science*, 31 (2000) 1543-1555.

[55] B. Clausen, T. Lorentzen, T. Leffers, *Acta Mater*, 46 (1998) 3087-3098.

[56] J.W.L. Pang, T.M. Holden, T.E. Mason, *Acta Mater*, 46 (1998) 1503-

1518.

[57] Y.D. Wang, R. Lin Peng, X.L. Wang, R.L. McGreevy, *Acta Mater*, 50 (2002) 1717-1734.

[58] Y.D. Wang, H. Tian, A.D. Stoica, X.L. Wang, P.K. Liaw, J.W. Richardson, *Nat Mater*, 2 (2003) 101-106.

[59] M.P. Miller, J.V. Bernier, J.S. Park, A. Kazimirov, *Review of Scientific Instruments*, 76 (2005) 1-11.

[60] J.V. Bernier, M.P. Miller, *Journal of Applied Crystallography*, 39 (2006) 358-368.

[61] N. Jia, R. Lin Peng, Y.D. Wang, S. Johansson, P.K. Liaw, *Acta Mater*, 56 (2008) 782-793.

[62] K.Z. Baba-Kishi, *Journal of Materials Science*, 37 (2002) 1715-1746.

[63] R.A. Schwarzer, D.P. Field, B.L. Adams, M. Kumar, A.J. Schwartz, *Electron Backscatter Diffraction in Materials Science*, (2009) 1-20.

[64] A. Arsenlis, D.M. Parks, *Acta Mater*, 47 (1999) 1597-1611.

[65] P.J. Buchanan, V. Randle, P.E.J. Flewitt, *Scripta Mater*, 37 (1997) 1511-

1518.

[66] A.J. Wilkinson, D.J. Dingley, *Acta Metallurgica Et Materialia*, 39 (1991) 3047-3055.

[67] T. Maitland, S. Sitzman, *Scanning Microscopy for Nanotechnology Techniques and Applications*, (2007) 41-75.

[68] F.J. Humphreys, *Journal of Materials Science*, 36 (2001) 3833-3854.

[69] S.I. Wright, M.M. Nowell, D.P. Field, *Microscopy and Microanalysis*, 17 (2011) 316-329.

[70] M. Kamaya, *Materials Characterization*, 60 (2009) 125-132.

[71] K. Masayuki, *Ultramicroscopy*, 111 (2011) 1189-1199.

[72] R. Yoda, T. Yokomaku, N. Tsuji, *Materials Characterization*, 61 (2010) 913-922.

[73] M. Kamaya, A.J. Wilkinson, J.M. Titchmarsh, *Acta Mater*, 54 (2006) 539-548.

[74] M. Kamaya, A.J. Wilkinson, J.M. Titchmarsh, *Nuclear Engineering and Design*, 235 (2005) 713-725.

- [75] A. Sáez-Maderuelo, L. Castro, G. De Diego, *Journal of Nuclear Materials*, 416 (2011) 75-79.
- [76] J.J. Sanchez-Hanton, R.C. Thomson, *Materials Science and Engineering A*, 460-461 (2007) 261-267.
- [77] E.M. Lehockey, Y. Lin, O.E. Lepik, *Electron Backscatter Diffraction in Materials Science*, (2000) 247-264.
- [78] J.Y. Kang, B. Bacroix, H. Réglé, K.H. Oh, H.C. Lee, *Acta Mater*, 55 (2007) 4935-4946.
- [79] C. Fukuoka, K. Morishima, H. Yoshizawa, K. Mino, *Scripta Mater*, 46 (2002) 61-66.
- [80] R. M'Saoubi, L. Ryde, *Materials Science and Engineering A*, 405 (2005) 339-349.
- [81] K. Fujiyama, K. Mori, D. Kaneko, H. Kimachi, T. Saito, R. Ishii, T. Hino, *International Journal of Pressure Vessels and Piping*, 86 (2009) 570-577.
- [82] D.J. Child, G.D. West, R.C. Thomson, *Acta Mater*, 59 (2011) 4825-4834.
- [83] R. Badji, T. Chauveau, B. Bacroix, *Mat Sci Eng a-Struct*, 575 (2013) 94-103.

- [84] D.P. Field, K.R. Magid, I.N. Mastorakos, J.N. Florando, D.H. Lassila, J.W. Morris, *Philos Mag*, 90 (2010) 1451-1464.
- [85] D. Kempf, V. Vignal, G. Cailletaud, R. Oltra, J.C. Weeber, E. Finot, *Philos Mag*, 87 (2007) 1379-1399.
- [86] R.L. Peng, G. Chai, N. Jia, Y.D. Wang, S. Johansson, *Fatigue and Fracture of Engineering Materials and Structures*, 31 (2008) 892-901.
- [87] P. Evrard, A. El Bartali, V. Aubin, C. Rey, S. Degallaix, D. Kondo, *International Journal of Solids and Structures*, 47 (2010) 1979-1986.
- [88] C. Pinna, J.H. Beynon, C.M. Sellars, M. Bornert, *Proceedings of the Int. Conf. on Mathematical Modelling in Metal Processing and Manufacturing-COM 2000*, (2000).
- [89] L.E. Hernandez-Castillo, *Determination of micro-scale strain distribution in hot-worked steel microstructures*, (2005).
- [90] N. Rupin, *Déformation á Chaud de Matériaux Biphases: Modérations Théoriques et Confrontations Expérimentales*, (2007).
- [91] H. Unckel, *J. Inst. Met.*, 61 (1937).
- [92] L. Duprez, B.C. De Cooman, N. Akdut, *Zeitschrift fuer*

Metallkunde/Materials Research and Advanced Techniques, 93 (2002) 236-243.

[93] F.E. Al Jouni, Hot deformation of two phase stainless steels, (1983).

[94] J.J. Petrovic, A.K. Vasudevan, Mater Sci Eng, 34 (1978) 53-59.

[95] X.L. Cai, J. Feng, W.S. Owen, Metallurgical Transactions A, 16 (1985) 1405-1415.

[96] G.I. Raab, Materials Science and Engineering A, 410-411 (2005) 230-233.

[97] Z.J. Wang, Y. Liu, J Mater Process Tech, 210 (2010) 1536-1544.

[98] C. Badulescu, M. Grédiac, J.D. Mathias, Measurement Science and Technology, 20 (2009).

[99] L. Allais, M. Bornert, T. Bretheau, D. Caldemaison, Acta Metallurgica Et Materialia, 42 (1994) 3865-3880.

[100] A. Soula, D. Locq, D. Boivin, Y. Renollet, P. Caron, Y. Bréchet, Journal of Materials Science, 45 (2010) 5649-5659.

[101] H. Ghadbeigi, C. Pinna, S. Celotto, J.R. Yates, Materials Science and

Engineering A, 527 (2010) 5026-5032.

[102] J. Kang, Y. Ososkov, J.D. Embury, D.S. Wilkinson, *Scripta Mater*, 56 (2007) 999-1002.

[103] E. Héripré, M. Dexet, J. Crépin, L. Gélébart, A. Roos, M. Bornert, D. Caldemaison, *International Journal of Plasticity*, 23 (2007) 1512-1539.

[104] E. Soppa, P. Doumalin, P. Binkele, T. Wiesendanger, M. Bornert, S. Schmauder, *Computational Materials Science*, 21 (2001) 261-275.

[105] P. Doumalin, M. Bornert, *Interferometry in Speckle Light, Theory and Applications*, (2000) 67-74.

[106] P.J. Jacques, Q. Furnémont, F. Lani, T. Pardoën, F. Delannay, *Acta Mater*, 55 (2007) 3681-3693.

[107] M. Bornert, F. Valès, H. Gharbi, D. Nguyen Minh, *Strain*, 46 (2010) 33-46.

[108] G. Martin, D. Caldemaison, M. Bornert, C. Pinna, Y. Bréchet, M. Véron, J.D. Mithieux, T. Pardoën, *Experimental Mechanics*, 53 (2013) 205-215.

[109] O. Muransky, P. Sittner, J. Zrník, E.C. Oliver, *Acta Mater*, 56 (2008) 3367-3379.

[110] N. Jia, R.L. Peng, G.C. Chai, S. Johansson, Y.D. Wang, *Mat Sci Eng a-Struct*, 491 (2008) 425-433.

[111] S. Harjo, Y. Tomota, P. Lukas, D. Neov, M. Vrana, P. Mikula, M. Ono, *Acta Mater*, 49 (2001) 2471-2479.

[112] Y. Tomota, P. Lukas, S. Harjo, J.H. Park, N. Tsuchida, D. Neov, *Acta Mater*, 51 (2003) 819-830.

[113] N. Jia, R.L. Peng, D.W. Brown, B. Clausen, Y.D. Wang, *Metall Mater Trans A*, 39A (2008) 3134-3140.

Part I

2. Investigation of yielding behavior of duplex stainless steel by nanoindentation, EBSD and in-situ neutron diffraction

2.1 Introduction

Until a recent date, duplex stainless steels (DSS) have been researched and characterized as super-plastic materials [1-5]. More than all, DSS which has a two-phase microstructure mixed ferrite(α) and austenite(γ), has been received great attention with its cost-saving combination of high strength and improved resistance to general and localized corrosion, stress-corrosion cracking, abrasion and wear [4]. Popular DSS which is widely used recently contains Ni at levels ranging from 4 to 7 wt.% to improve both γ stability and formability. However, Ni in DSS is high-priced material, thus price of DSS is highly dependent on Ni as shown in Fig. 2.1. Besides, Ni causes an allergic reaction in human skin [4-6]. Over the years, many researches have been

carried out to develop harmless and cost-effective DSS. For this, N has been considered as a candidate alloying element to achieve a reduction in Ni and improvements in both the strength and corrosion resistance of DSS [4-6].

Deformation of multi-phase alloys like DSS, is inhomogeneous, and each phase in the material will have a different response to an applied stress or strain. Therefore it is hard to estimate mechanical behavior of DSS, and of course it is also hard to control mechanical properties. In addition, there are few reference of mechanical properties data for high N DSS because chemical composition of high N DSS is very complex and various. However, it is necessary to understand mechanical behavior of high N DSS for appropriate use and commercial application.

Generally, intrinsic mechanical properties of each phase directly affect overall plastic behavior. Thus it is important to define respective mechanical behaviors of α and γ grains in DSS, for analyzing performance of α - γ mixed DSS. Especially, it is very important issue that which phase is softer in multi-phase alloys, because elasto-plastic transition stress of soft phase dominantly rules elastic limit of material. For those reasons, in the present studies, the plastic yielding behavior of each phase in DSS was often focused by many different methods like electron backscattered diffraction (EBSD) or time-of-flight (TOF) analysis using in-situ neutron diffraction [7, 8]. Above all,

neutron diffraction technique is a well established tool for studying micromechanical behavior of materials [9, 10]. Lattice plane stain (LPS) of various lattice planes of α and γ were determined as a function of the applied true stress during uniaxial tension to define yield stress. However, the LPS can indicate only elastic strain [11, 12]. Thus plastic behavior is indirectly estimated by tracing change of LPS while macro-scale deformation. However, for DSS, it is difficult to separate the individual contribution of each phase from macroscopic applied stress or strain, and state of stress-strain is generally assumed as isostress [7, 9, 11, 13]. In case of DSS, the critical issue arises in this procedure. The respective phases, α and γ , have different mechanical properties and response to stress or strain. Thus in DSS, in a greater or less, strain partitioning between α and γ necessarily occurs during deformation [7, 9, 13, 14]. Consequently, if yield stress or other specific stress state is defined assuming isostress state, it can involve critical error because of disregarding strain partitioning effect. And in-situ neutron diffraction method collects diffracted neutron beam with specific intervals of stress or strain [15]. Thus specific stress states can't be measured precisely by this method since there is a limitation in the step for the static load control during in-situ neutron diffraction. Moreover, neutron diffraction has bad accessibility because size of equipment is quite huge and there are few locations to use it. For these reasons, more simple method is demanded to measure precise yielding behavior of each phase in DSS.

Recently, nanoindentation has been used to probe small-scale mechanical properties, which are relevant to a wide range of materials and applications [16]. Especially in multi-phase materials, nanoindentation technique combining with EBSD is useful to measure mechanical behavior of respective phases in materials [17]. The response of a material to nanoindentation is usually presented in the form of a load–displacement (L-D) curve. Many researchers have tried to define various mechanical properties from L-D curve, and now there are various reliable L-D curve analysis methods [18-21]. Unlike neutron diffraction analysis, separated intrinsic mechanical behavior of each phase can be measured by nanoindentation, that is, it is not affected by strain partitioning of respective phases in DSS. And elasto-plastic transition stress can be calculated as continuous value by this technique. Moreover, it is much accessible and easy to perform than neutron diffraction.

For these reasons, nanoindentation was suggested to measure elasto-plastic transition behavior of each phase in DSS. To obtain intrinsic deformation behavior of individual α and γ grains, nanoindentation tests combined with EBSD were carried out. And the combination method with EBSD and SPM were used to eliminate grain boundary effect during nanoindentation. The correlation between the small-scale nanoindentation behavior to the macro-scale tensile behavior was investigated by comparing the indentation load-depth (L-D) curves for each phase with the lattice strains

of various lattice planes in α and γ obtained by in-situ neutron diffraction. In addition, the dislocation nucleation energy (DNE) was calculated to explain deformation behavior of DSS.

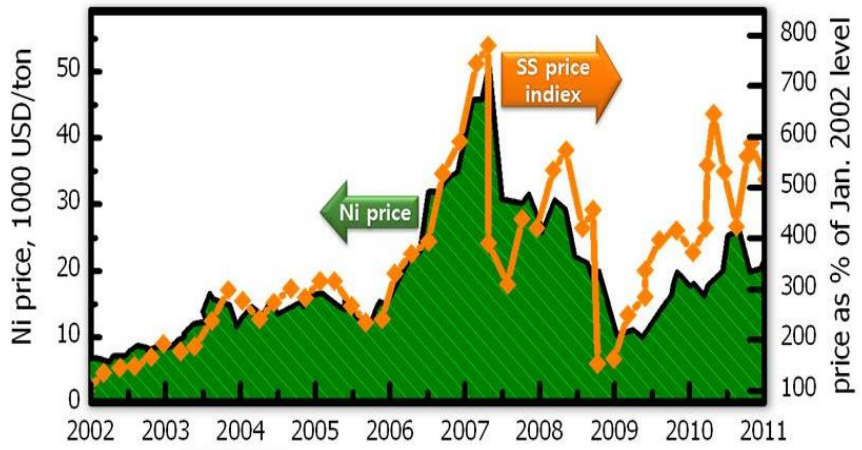


Figure 2.1 Price histories of stainless steel and Ni.

2.2 Materials and experimental procedures

2.2.1 Materials: Duplex Stainless Steel

For getting similar numbers of test data of each phase from specimen, the composition of the α - γ mixed DSS used in this study was designed by Ferrous Alloy Group of KIMS. In this research, two kinds of specimen, DSH and DSL, were used. Chemical composition of DSH is Fe-24.67Cr-7.04Mn-3.98Ni-3.88Mo-0.49Si-0.45N-0.022C and that of DHL is Fe-17.2Cr-5.9Mn-5.01W-2.54Mo-0.31Si-0.43N-0.012C (DSL). Both alloys contain the high fraction of nitrogen for controlling phase fraction of α - γ mixed DSS by stabilizing γ phase [22]. And the fraction of other alloying elements in DSH is higher than that in DSL. The alloys were fabricated utilizing a pressurized induction melting furnace. After homogenization, the ingots were hot-rolled into sheets (thickness is 4mm), followed by water quenching. Then DSH was solution-treated at 1200 degree for 1hr, and DSL was solution-treated at 1090 degree for 30min.

EBSM was performed for getting information about phase fraction and micro structure of the specimens. Every EBSM tests in this research were carried out in a SEM (Hitachi SU70) equipped with a field emission gun. The EBSM images were analyzed by an TSL OIM collection 6 and TSL OIM

analysis 6.1, EDAX Instruments. The accelerating voltage and probe current were set at 15 kV and 4 nA, respectively. Step size for EBSD mapping was 1 μm . In order to get reliable SEM/EBSD image and nanoindentation curve, the specimen was prepared by gentle polishing with SiC paper and repeated electro-polishing with a solution of 20% perchloric acid (HClO_4), 70% ethanol ($\text{C}_2\text{H}_5\text{OH}$) and 10% ethylene glycol monobutyl ether ($\text{CH}_3(\text{CH}_2)_3\text{OCH}_2\text{CH}_2\text{OH}$) in volume at 20 °C with the voltage of 30V for 10 s, to remove the mechanically damaged layer. As shown in Fig. 2.2, DSH has 47% of α and 53% of γ in volume fraction, and DSL has 52% of α and 48% of γ . In case of DSH, grain size of α and γ is approximately 16.8 μm and 11.2 μm , respectively. In DSL, grain size of α and γ is approximately 12.4 μm and 7.3 μm . Grain size distribution of DSH and DSL are plotted as Fig 2.3 and Fig. 2.4.

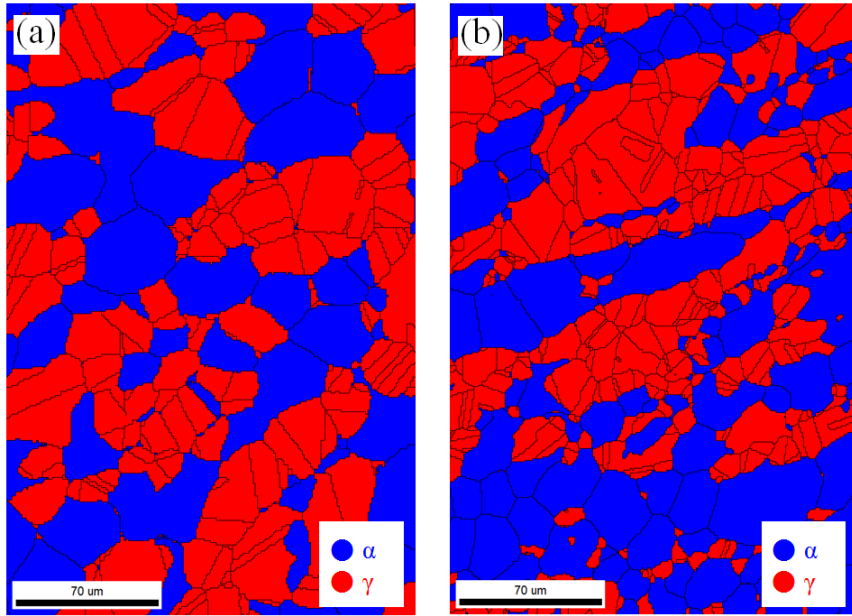


Figure 2.2 Phase map of (a) DSH and (b) DSL by EBSD.

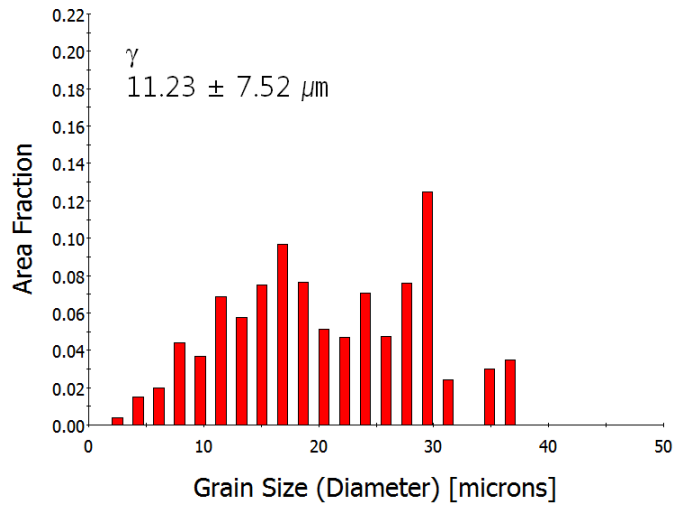
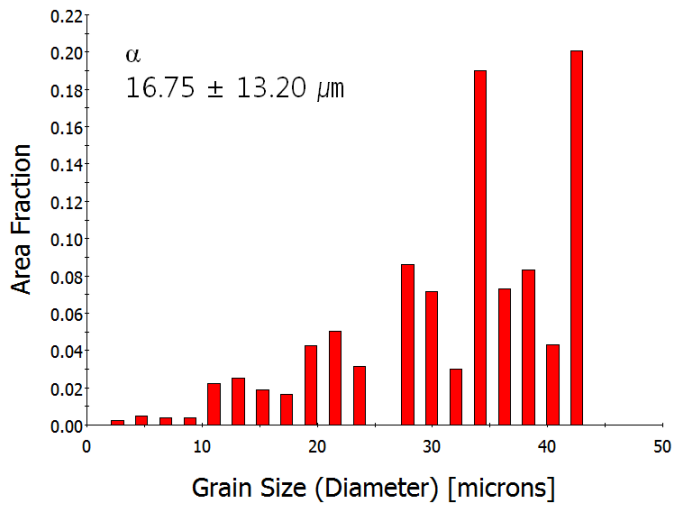


Figure 2.3 Grain size distribution of DSH.

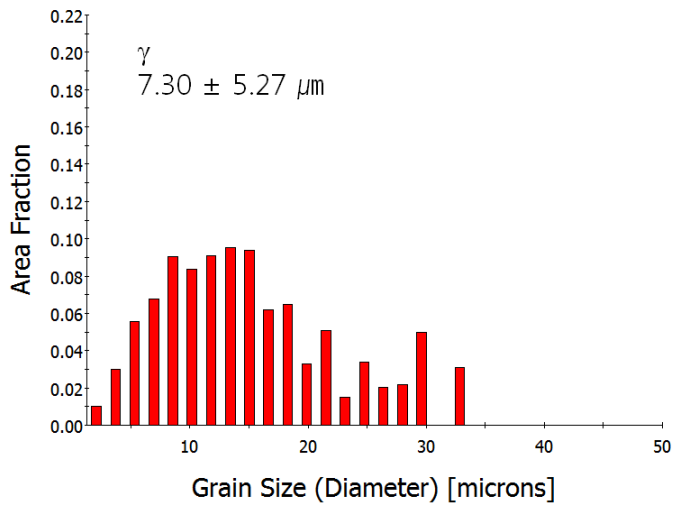
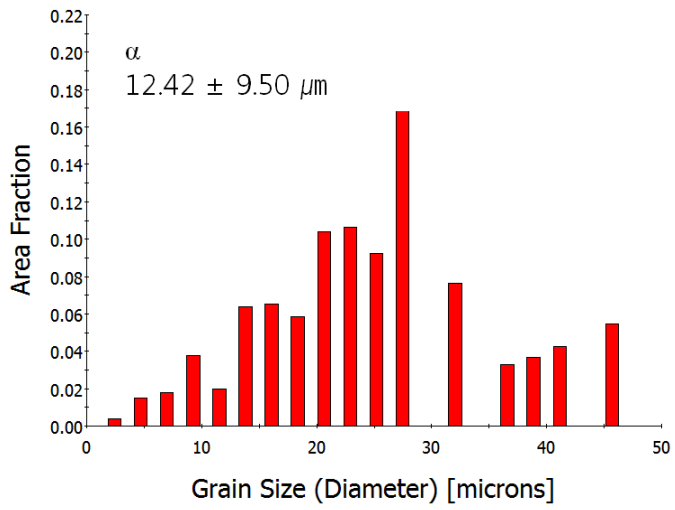


Figure 2.4 Grain size distribution of DSL.

Then overall mechanical properties were measured by uniaxial tension test. The specimen (ASTM E8M) was tensile-tested at room temperature with a strain rate of $5 \times 10^{-3} \text{ s}^{-1}$ using a servohydraulic machine (INSTRON 5882, Canton, USA). Stress-Strain curve of specimen is shown as Fig. 2.5. Yield stress of DSH and DSL is 636 MPa and 657 MPa, respectively and elongation of DSH and DSL is 34% and 20%. In this result, we could find some notable point, that DSH and DSL have similar initial yield strength even though they have quite different chemical composition. But yield stress from uniaxial tension can be strongly influenced by crystal orientation texture. Therefore overall texture of specimen was measured by EBSD and orientation maps of specimen are drawn as Fig 2.6 and Fig 2.7. For measuring precise texture, orientation distribution function (ODF) is also drawn as Fig. 2.8 and Fig 2.9. If specimen has such strong texture, it will affect mechanical properties, so anisotropy of mechanical property must be considered. But as you shown in Fig. 2.8 and Fig. 2.9, both DSH and DSL don't have any specific strong texture on every phase. So it is reasonable to think that texture doesn't affect overall yield stress of specimen in this case. Therefore, overall yield stress of specimen will be influenced mostly by intrinsic mechanical property.

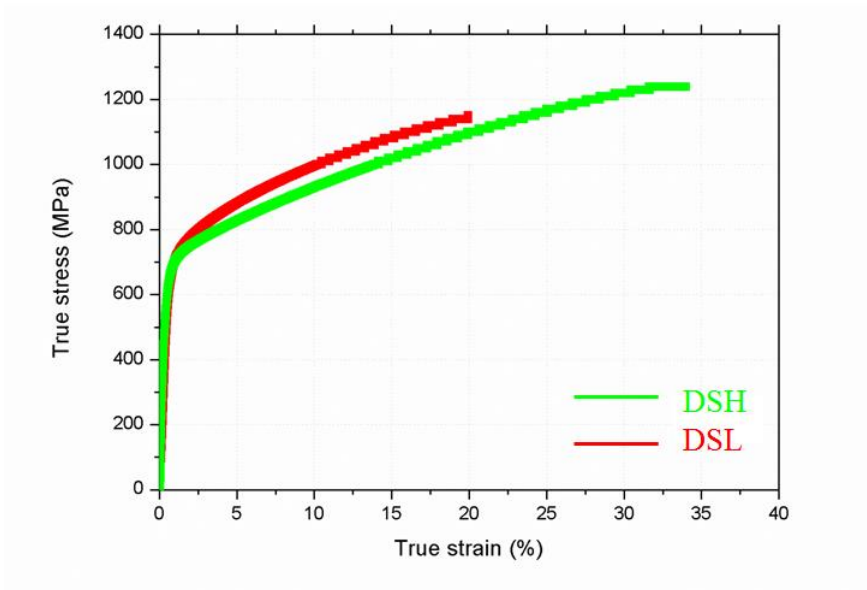


Figure 2.5 S-S curves of DSH and DSL

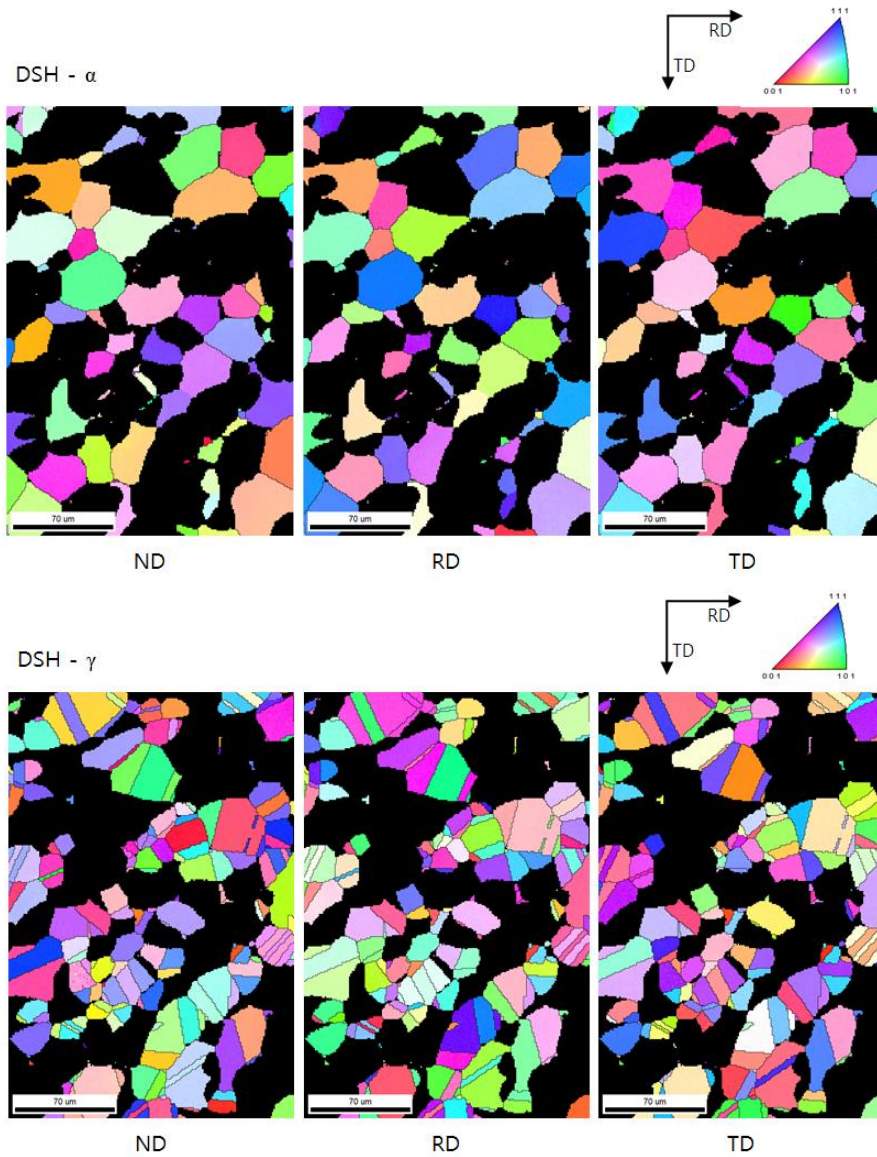


Figure 2.6 Crystal orientation map of DSH.

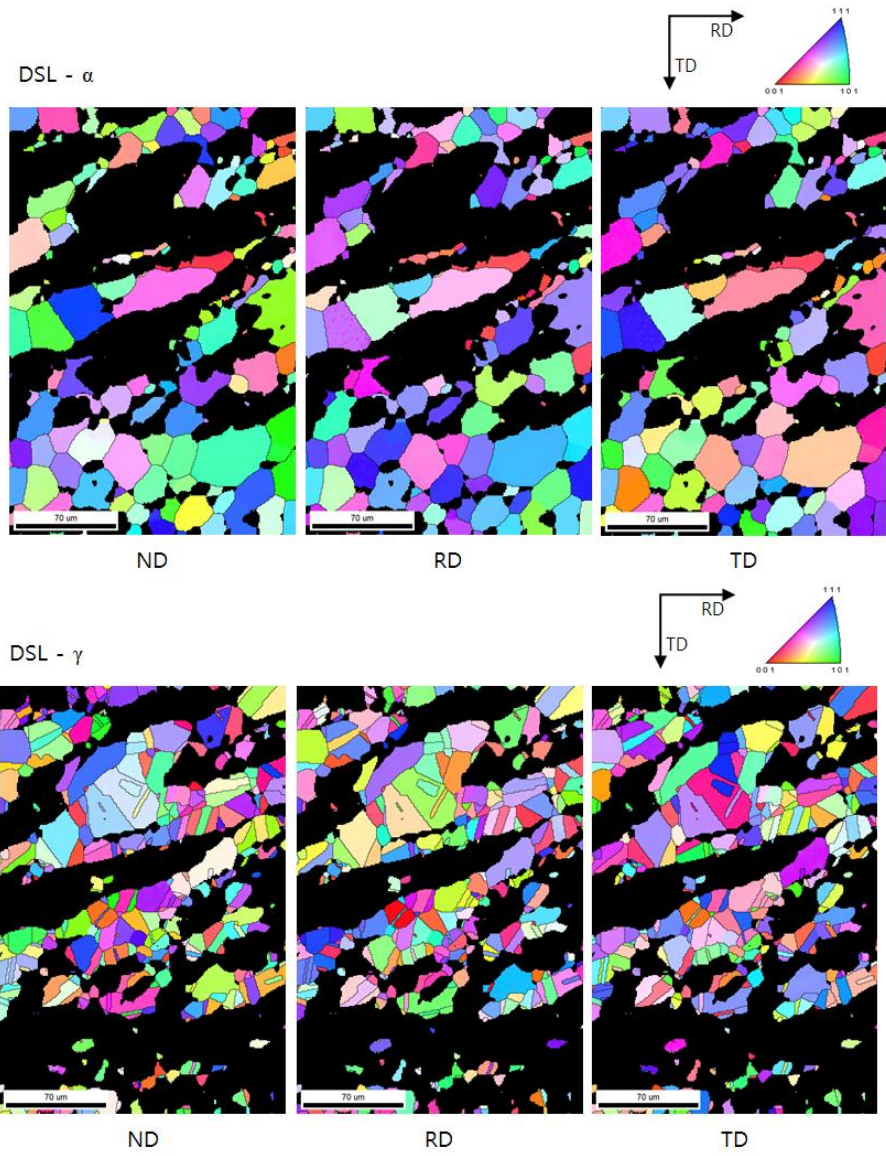
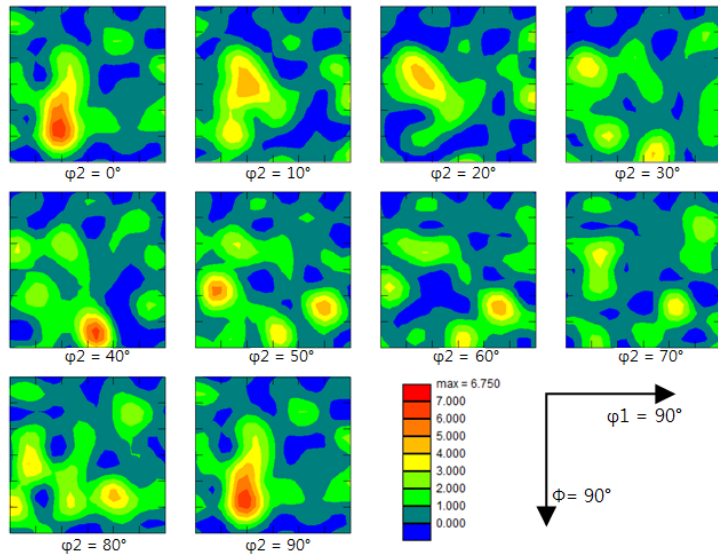


Figure 2.7 Crystal orientation map of DSL.

DSH - α



DSH - γ

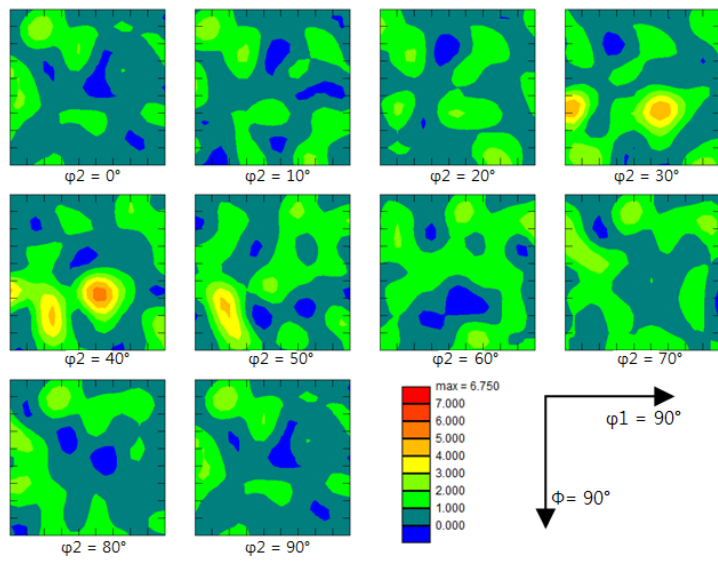
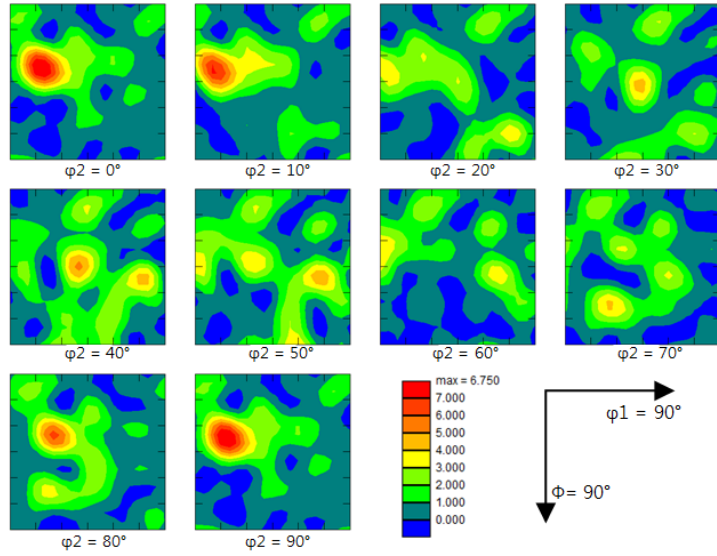


Figure 2.8 Orientation distribution function (ODF) of DSH.

DSL - α



DSL - γ

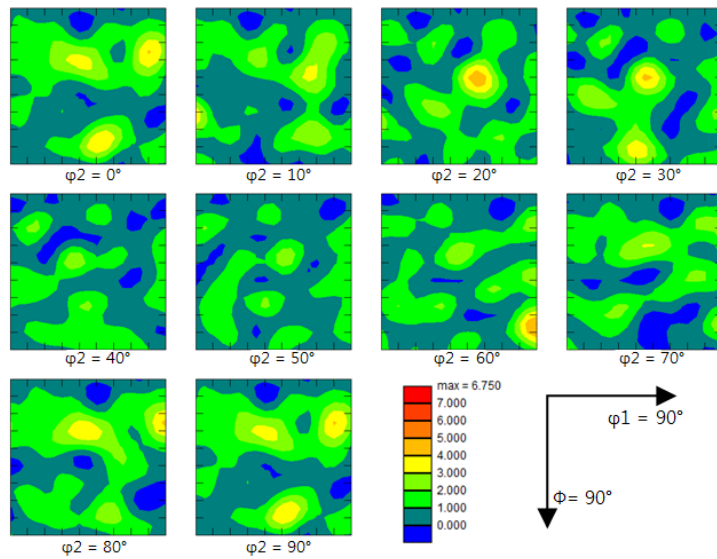


Figure 2.9 Orientation distribution function (ODF) of DSL.

2.2.2 Experimental procedure

In order to observe intrinsic deformation behavior of respective phases in specimens, EBSD combined nanoindentation tests were carried out using a Hysitron Tribolab nanoindentation system in load control at a constant loading rate of 200Ns^{-1} up to a maximum load of 5000N. For precise elastic contact analysis, a cono-spherical type indenter was used because of its simple geometry. Radius of indenter tip is $1\mu\text{m}$ and Included angle 120 degree. The tests were performed as 10×12 rectangular arrays by automation mode on selected zone of each specimen. The distance of each indentation point was $30\mu\text{m}$ wide and also in height, total number of indenting point is 120. Since nanoindentation test is very sensitive to surface condition, a scanning probe microscope (SPM) was carried out to evaluate surface morphology, before and after nanoindentation. Image quality maps by EBSD of indenting areas were also used to observe the surface. The result data of nanoindentation test which was performed at inappropriate area like grain boundaries or local defect was identified by those images, and omitted from subsequent analysis. After indentation, EBSD image was scanned on indenting area. Phase map and crystal orientation (ND) map of indentation area are shown as Fig 2.10. Then using EBSD phase map, L-D curves were grouped according to the phase.

To verify results from nanoindentation, angular-dispersive in-situ neutron diffraction test was carried out using a residual stress analysis diffractometer equipped with a deformation device enabling tensile straining up to a maximum load of 20 kN at HANARO, Korea Atomic Energy Research Institute (KAERI), South Korea. The tensile specimens were prepared using electrical discharge machining (EDM) with the total length of 100 mm and the gauge length of 25 mm. The diffraction was measured from the gauge volume of neutron beam defined by a 5-mm wide, 4-mm high cadmium slit in the incident beam and 2-mm wide cadmium slit. A bent perfect crystal monochromator Si(220) at the take-off angle of 45° was adopted to provide the wavelength of 1.46 \AA of the neutron beam. And a high-resolution position-sensitive detector was used in the in-situ experiment, and the neutron beam was monochromatized to a wavelength of 1.8344 \AA . And the instrumental resolution of the diffractometer was of $\Delta d/d \approx 2.0 \times 10^{-3}$, which was sufficient to the evaluation of broadening effects. The neutron measurements were performed at diffraction angles (2θ) of 41.0° , 60.4° , and 76.0° for (110), (200), and (112) diffraction peaks of the α phase, respectively, and 2θ of 47.0° , 83.3° and 88.0° for (200), (311) and (222) diffraction peaks of the γ phase, respectively. The $(200)\alpha$, $(112)\alpha$, $(110)\alpha$, $(200)\gamma$, $(311)\gamma$ and $(222)\gamma$ reflections A number of static loading stages were used to measure neutron diffraction peaks from the specimen loaded were measured with a crosshead speed of 0.01 mm s^{-1} (corresponding to the strain rate of $\sim 4 \cdot 10^{-4} \text{ s}^{-1}$) under a controlled

load of 1 kN in the elastic region, followed by displacement control corresponding to a strain of 0.1 after yielding. LPS of various lattice planes of α and γ were determined as a function of the applied stress during uniaxial tension to define plastic transition stress. Then yield stress could be measured by analyzing increasing tendency of LPS.

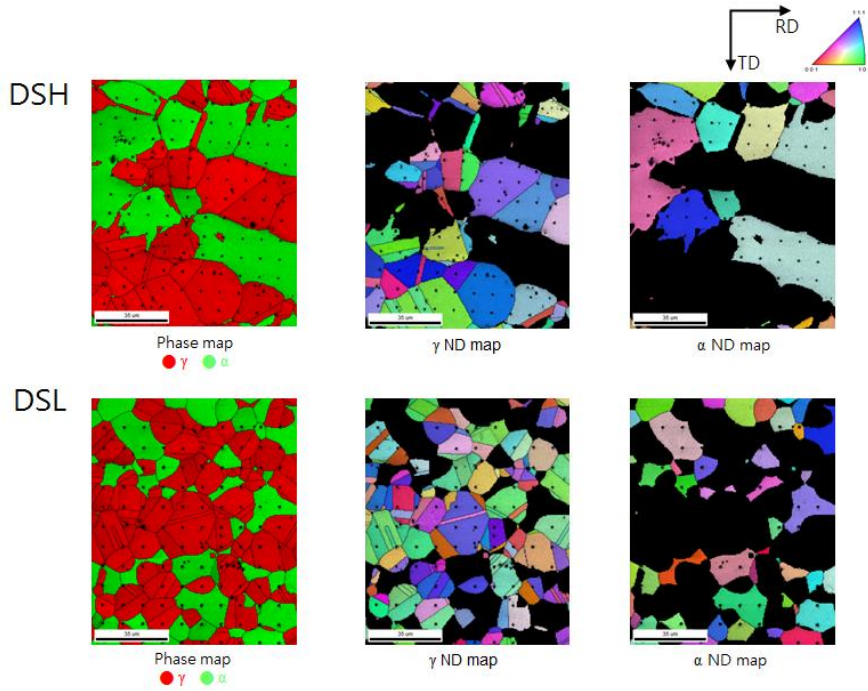


Figure 2.10 Phase map and crystal orientation (ND) map of indentation area.

2.3 EBSD combined Nanoindentation

Grouped L-D curves from EBSD combined nanoindentation test were drawn as Fig. 2.11 and 2.12. The overall analyses of L-D curves were conducted using the Oliver and Pharr method [18] and Hertzian contact theory [23]. As shown in Fig. 2.8 and 2.9, specific texture was not observed in any phase on these specimens, and indentations were performed on various segregated grains. In addition, recent researches reported that intrinsic properties measured by anisotropic analysis in nanoindentation are almost same with isotropic case in BCC and FCC metallic materials [24]. For these reasons, texture effect was ignored in this research and analysis is treated as isotropic case.

As shown in Fig. 2.11 and 2.12, a sudden displacement burst, called a pop-in was observed in every single nanoindentation. In force-controlled experiments on pristine oxide-free surfaces, the stress level reached underneath the indenter just before the first pop-in has been found to correspond to the theoretical strength of the material [25-27]. It is thus now widely accepted that dislocation nucleation is indeed responsible for the pop-in event, and it has been shown by experimental and MD simulation [24, 28, 29]. On carefully polished metal surfaces, the deformation before the first pop-in has been shown to be perfectly elastic [25, 30]. Therefore maximum

shear stress underneath indenter tip when pop-in occurs can be considered as elasto-plastic transition stress. Yield stress means stress that occur elasto-plastic transition during tensile test. In order to define elasto-plastic transition stress of respective phases in DSH and DSL, maximum shear stress when pop-in occurs is measured.

If indenter tip is spherical at shallow depths, the experimental data before the first pop-in can be identified by fitting the solution of Hertzian contact theory [23]:

$$P = \frac{4}{3} E_r \sqrt{R} h^3 \quad (2-1)$$

where P is the load applied, h is the penetration depth, R is the radius of the indenter tip, and E_r is the effective (or reduced) modulus of indentation. The radius of used indenter tip in this research, R was defined to be $1\mu\text{m}$ from a calibrated data of Hysitron Tribolab nanoindentation system, using standard fused silica. The point that the tip geometry transit from spherical to cone was calculated approximately 267nm by method of Gouldstone et al. [31]. As shown in Figure 4, every pop-in had occurred at penetration depth under 267nm , so pop-in section was assumed that indentation performs with a spherical tip. And in case of isotropic elastic material, the effective indentation modulus E_r given in Eq. (2-2) is provided by the elastic modulus

of the sample and indenter as follows:

$$\frac{1}{E_r^2} = \frac{1-\nu_i^2}{E_i^2} + \frac{1-\nu_s^2}{E_s^2} \quad (2-2)$$

where ν_s and ν_i are the Poisson's ratios of the specimen and the indenter, and E_s and E_i are the Young's modulus of the specimen and the indenter, respectively. The theoretical (Hertzian) elastic behavior during indentation was calculated using this effective modulus of α and γ at room temperature and the isotropic elastic constants of the diamond tip [29]. Elastic modulus of each phase was obtained from L-D curves by using solution of Hertzian elastic contact theory with Oliver and Pharr method, and Poisson's ratio was acquired from general experimental data of austenitic and ferritic Ni-Cr stainless steel [18, 23, 32, 33]. Followed elastic constants, $E_i = 1141$ GPa, $\nu_i = 0.07$, $\nu_{s(\gamma)} = 0.29$, and $\nu_{s(\alpha)} = 0.29$ were used in this research. Poisson's ratios were defined as conventional value for austenitic and ferritic Ni-Cr stainless steel [32, 33]. And calculated elastic modulus is $E_{\alpha(DSH)} = 194$ GPa, $E_{\gamma(DSH)} = 184$ GPa, $E_{\alpha(DSL)} = 172$ GPa, and $E_{\gamma(DSL)} = 209$ GPa. Respective Hertzian elastic curves that used these elastic constant is also indicated in Fig. 2.11 and 2.12. In the elastic regime, Hertzian analysis gives the maximum shear stress underneath the indenter, τ_m , as follows:

$$\tau_m = 0.31 \left(\frac{6PE_r^2}{\pi^3 R^2} \right)^{1/3} \quad (2-3)$$

George E.P. et al. developed a statistical model for pop-in as cumulative probability [34]. In this case, pop-in data was treated by that model as a function of maximum stress under the indenter, because overall tendency of pop-in is clearly shown by this way. Fig. 2.13 shows cumulative probability of pop-in as a function of maximum stress under the indenter.

As shown in Fig. 2.13, interestingly, pop-in tendency of DSH and DSL was quite different. In case of DSH, γ has approximately 20% lower plastic transition stress than α . But in DSL, both α and γ has similar plastic transition stress. Average value of calculated elasto-plastic transition stress is shown as table 2.1. By results shown in table 1, intrinsic elasto-plastic transition stress of respective phases can be compared. However, macroscopic yield stress is affected by grain size, not only intrinsic property. Thus grain size effect should be considered to define tendency of yield stress in polycrystalline material like DSS. Recently, analyzing method of the intrinsic mechanical properties based on nanoindentation results considering the Hall–Petch relationship was developed [17]. Tendency of yield stress was defined from corrected elasto-plastic transition stress by that method as shown in table 2.2. According to corrected value, soft phase of DSH is γ , and its elasto-plastic

transition stress is 4.37GPa. In case of DSL, soft phase is also γ , and its elasto-plastic transition stress is 4.57GPa. As previously stated, yield stress of DSH and DSL is 636 MPa and 657 MPa. Thus it is reasonable to think that macroscopic yield stress of DSH is about 3% lower than DSL because soft phase of DSH has about 4% lower elasto-plastic stress than that of DSH even though average elasto-plastic transition stress of DSH is higher than DSL.

But it is hard to compare directly elasto-plastic transition stress (by nanoindentation) with yield stress (by uniaxial tension test), because their deformation mode and exact plastic transition stress value are quite different. Therefore it is necessary to verify this result by same deformation mode, uniaxial tension test. Thus in order to correlate the small-scale nanoindentation behavior to the macro-scale tensile behavior, an angular-dispersive in-situ neutron diffraction test was performed.

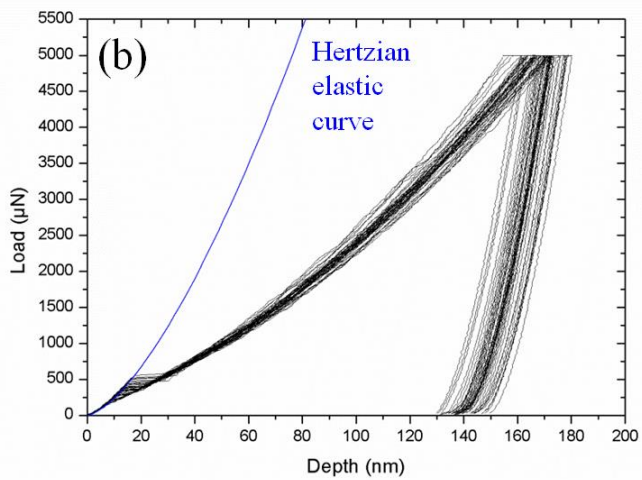
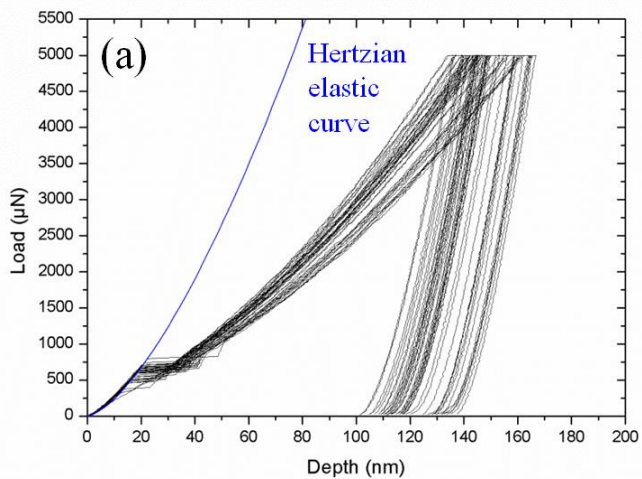


Figure 2.11 Group of L-D curves of (a) α , (b) γ in DSH.

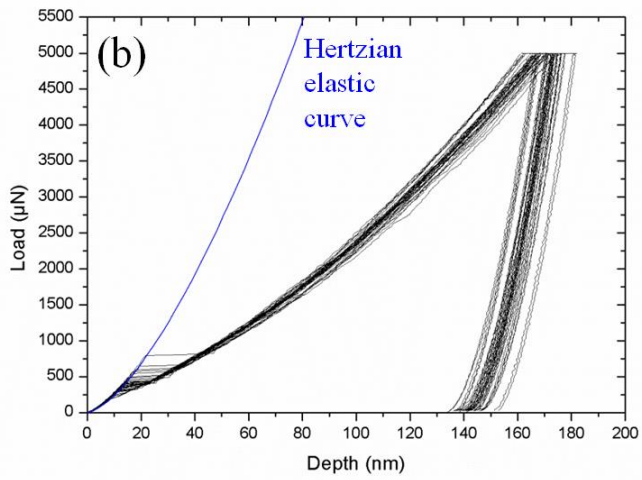
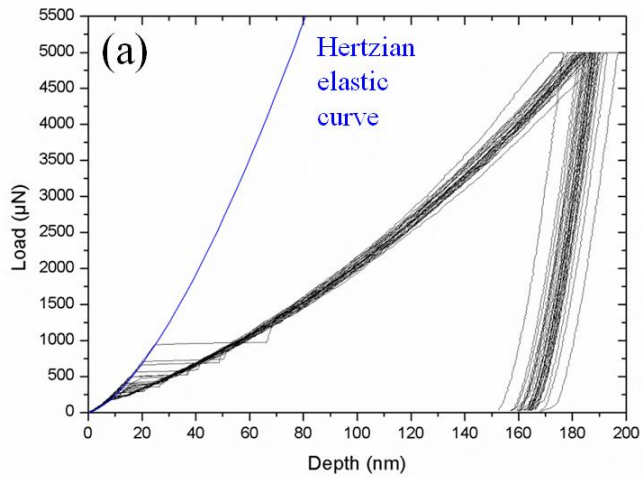


Figure 2.12 Group of L-D curves of (a) α , (b) γ in DSL.

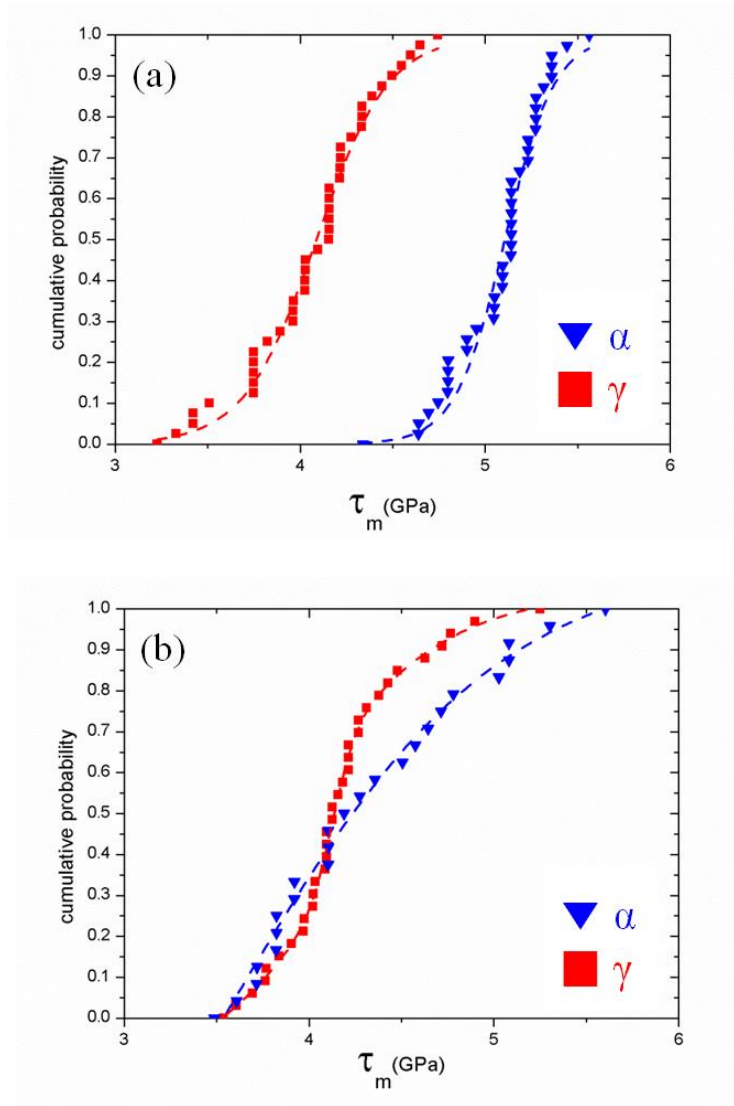


Figure 2.13 Cumulative probability of pop-in of (a) DSH and (b) DSL, as a function of maximum stress under the indenter.

	DSH		DSL	
	α	γ	α	γ
Average elasto-plastic transition stress (GPa)	5.07 ± 0.25	4.06 ± 0.36	4.47 ± 0.72	4.18 ± 0.37

Table 2.1 Average elasto-plastic transition stress of respective phases in DSS.

	DSH		DSL	
	α	γ	α	γ
Average elasto-plastic transition stress considering the Hall–Petch relationship (GPa)	5.32 ± 0.51	4.37 ± 0.67	4.77 ± 1.02	4.57 ± 0.76

Table 2.2 Corrected average elasto-plastic transition stress of respective phases in DSS considering the Hall–Petch relationship.

2.4 In-situ neutron diffraction

The LPS, ε_{hkl} , were calculated by the relation:

$$\varepsilon_{hkl} = (d_{hkl} - d_{hkl}^0) / d_{hkl}^0 = -\cot\theta_{hkl} \Delta\theta_{hkl} \quad (2-4)$$

where d_{hkl} and d_{hkl}^0 are the measured and stress-free LPS, respectively [7, 15, 35]. When the measured ε_{hkl} are plotted as a function of the applied stress, ε_{hkl} before tensile loading are tensile (positive) for γ and compressive (negative) for α [7, 35]. Due to the difference in thermal expansion coefficients, the residual tensile stress in γ , generated during cooling from the solution-annealing temperature, is balanced by the compressive stress in α . Thus, the variation of ε_{hkl} with the applied stress was replotted considering the thermal residual stresses following the approach by Harjo et al. [7]. To clarify the dissimilar responses of the two phases to plastic deformation, the applied nominal stresses were converted to true stress. Schematic image of this procedure is drawn as Fig. 2.14. In this research, stress state assumed as isostress case.

Fig. 2.15 and 2.16 show the changes in ε_{hkl} of respective phases in DSH and DSL as a function of applied true stress for the $(200)_\alpha$, $(112)_\alpha$, $(110)_\alpha$, $(200)_\gamma$, $(311)_\gamma$ and $(222)_\gamma$ reflections. At first, Fig. 2.15 shows general tendency of DSS [7]. Three stages I, II and III could be identified in the

relationships between LPS and applied stress. At stage I, an almost linear response of LPS to applied stress is observed for all the hkl planes which indicate that the elastic response is dominant during this stage in both phases. The different slopes for the different hkl reflections are associated mainly with the difference in individual diffraction elastic modulus. At stage II, the soft γ phase is plastically deformed around 400MPa, while the hard α phase is still deformed only elastically. As a result, LPS of γ phase increases more slowly with increasing applied stress, while the ε_{100} for α phase increases more rapidly. The onset stress of stage II deformation is marked by Y_γ . At stage III, both phases are deformed plastically around 700MPa, resulting in LPS of γ phase increasing rapidly again with increasing applied stress. Therefore it can be concluded that elasto-plastic transition stress of γ is much lower than α in case of DSH.

On the other hand, in DSL, tendency of yield stress is quite different with DSH. Respective phases of DSL behave as single phase metallic materials [14]. As you see in Fig. 2.16 (a) and (b), the early stage of deformation is purely elastic like DSH. And then, increasing rate of LPS becomes slower momentarily at around 600MPa in both α and γ . It is because that plastic flow starts preferentially towards the tensile direction. When plastic deformation starts, elastic strain of tensile direction is released instantly for a moment [8, 14, 36]. Thus, it is reasonable to think that elasto-plastic transition stress of α

and γ are similar each other in DSL. As a result, we concluded that yield stress of γ is lower than α in DSH, and similar in DHL on in-situ neutron diffraction test. And then, the elasto-plastic transition stress obtained from nanoindentation and yielding start stress measured by in-situ neutron diffraction were plotted and compared as previously planned.

Tendency of plastic yielding behavior measured from neutron diffraction and nanoindentation is shown as Fig. 2.17. Interestingly, tendency of elasto-plastic transition from two different experiments correspond each other correctly. Of course, elasto-plastic transition stress value from neutron diffraction is quite different with value from nanoindentation, because their deformation modes are quite different each other. However, as you see in these figures, it is shown that tendency of maximum shear stress when pop-in occurs can represent tendency of yield stress measured by uniaxial tension. At least, it seems pretty clear that pop-in behavior is closely related with yield stress.

Besides, comparing Fig. 2.17 (a) and (b), difference of elasto-plastic transition stress between respective phases in same specimen is bigger on in-situ diffraction test than on nanoindentation. In this LPS analysis, stress state is considered as isostress. But in fact, every single grain in the specimen cannot be in isostress state while tensile test. Actually, grains in specimen will

have stress state between isostrain and isostress. Thus difference of yield stress between respective phases in same specimen can be slightly overestimated on in-situ neutron diffraction results. And yield stress can't be measured precisely by in-situ neutron diffraction as nanoindentation since there is a limitation in the step for the static load control during in-situ neutron diffraction. As shown in Fig. 2.17 (a), it is expected that α and γ in DSL look like they have equal yield stress value because of this step size problem during in-situ neutron diffraction test. Take together all these results and discussion, it is possible that yield stress tendency of respective phases in multi-phase alloy can be measured more precisely by nanoindentation than in-situ diffraction test.

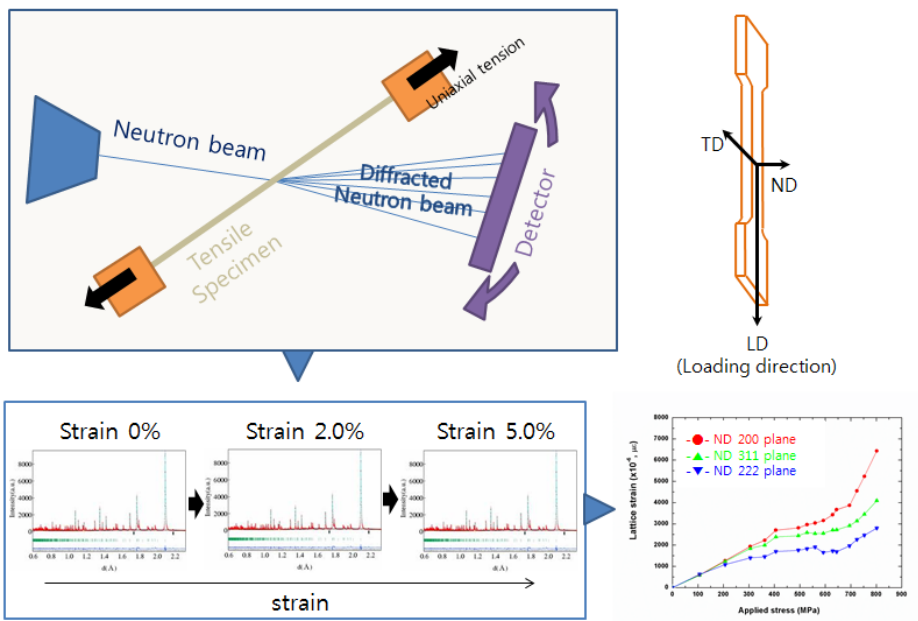


Figure 2.14 Schematic image of in-situ neutron diffraction.

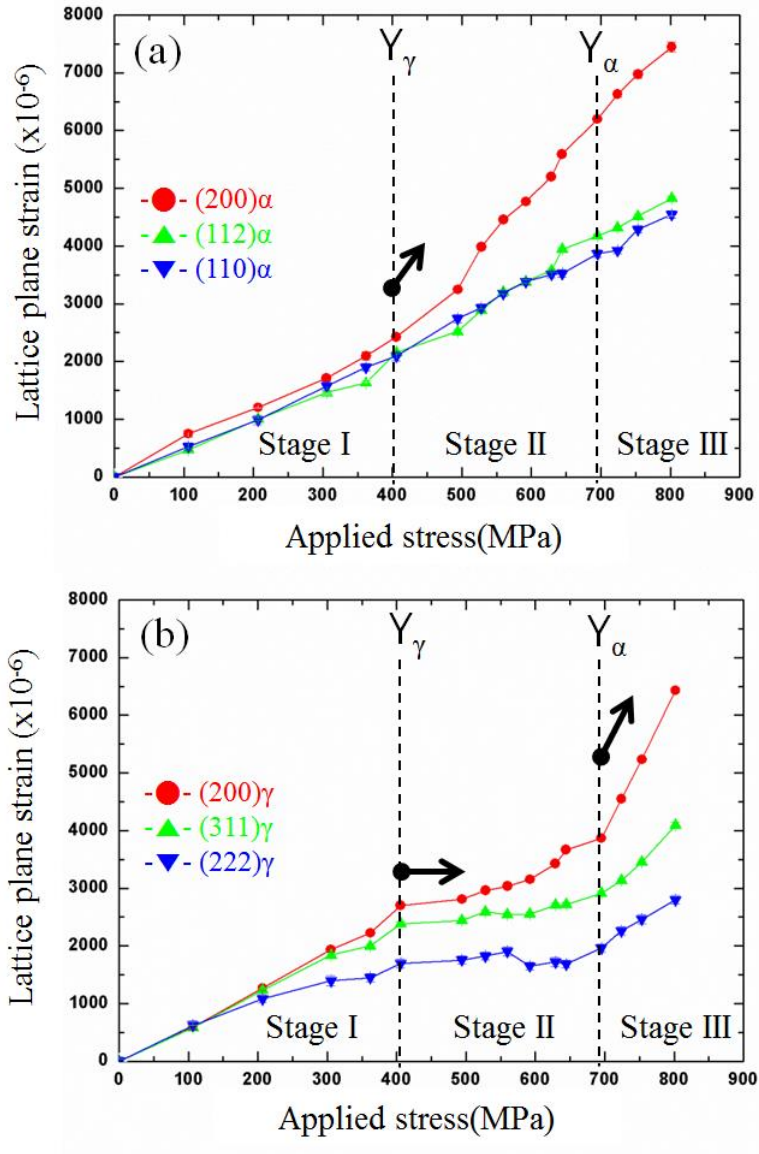


Figure 2.15 changes in ε_{hkl} of (a) α , (b) γ in DSH, as a function of applied true stress for the $(200)_\alpha$, $(112)_\alpha$, $(110)_\alpha$, $(200)_\gamma$, $(311)_\gamma$ and $(222)_\gamma$ reflections.

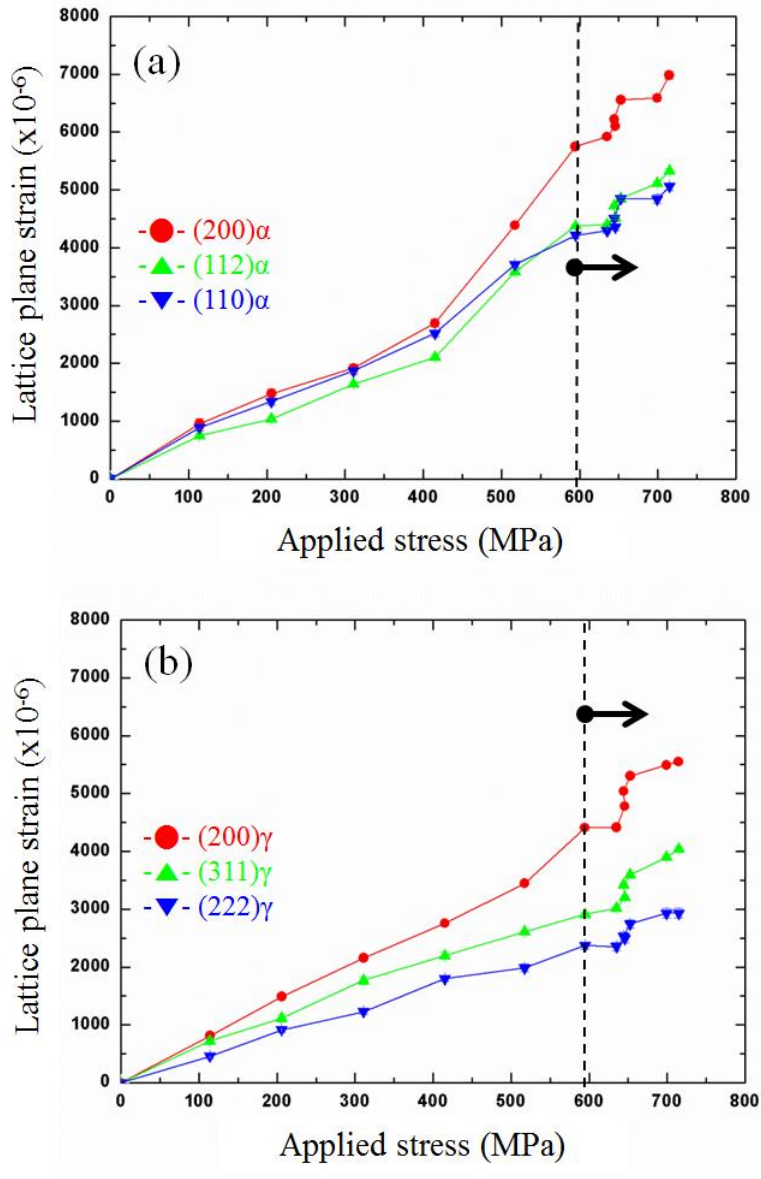


Figure 2.16 changes in ε_{hkl} of (a) α , (b) γ in DSL, as a function of applied true stress for the $(200)\alpha$, $(112)\alpha$, $(110)\alpha$, $(200)\gamma$, $(311)\gamma$ and $(222)\gamma$ reflections.

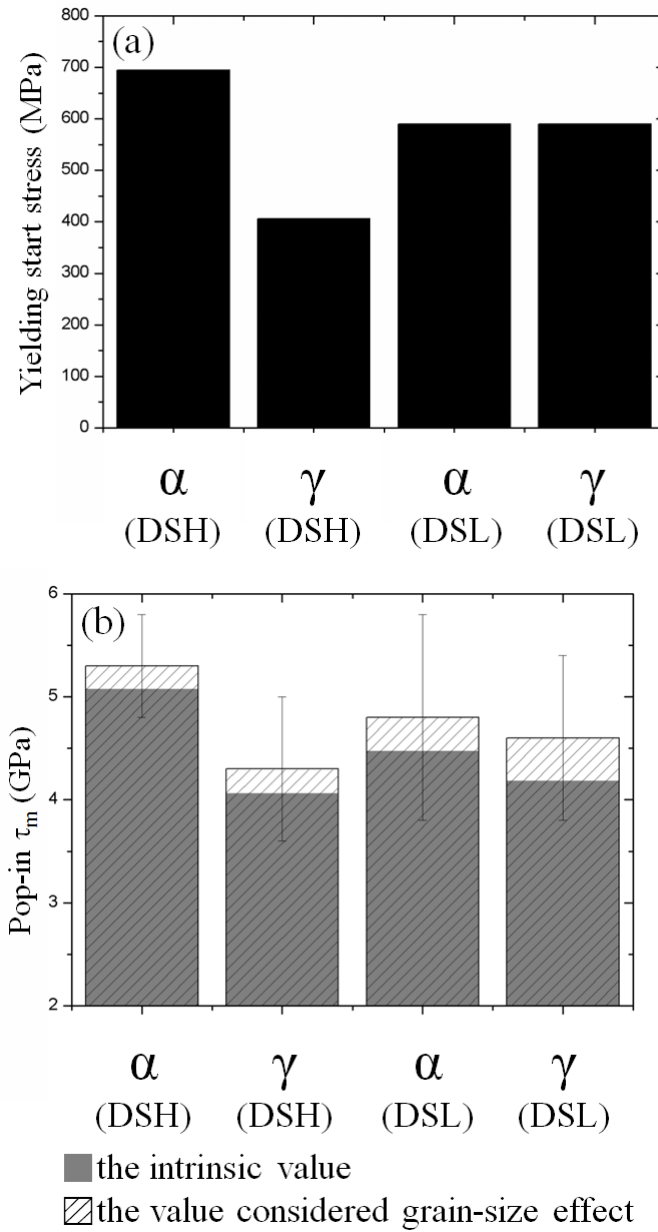


Figure 2.17 Elasto-plastic transition stress tendency from (a) in-situ neutron diffraction test and (b) nanoindentation.

2.5 Dislocation nucleation energy barrier calculation

Previously stated, maximum shear stress when pop-in occurs highly depends on dislocation nucleation energy (DNE) [24-29]. If pop-in behavior is highly related with overall tendency of the yield stress like above-analyzed results, yield stress tendency of respective phases in multi-phase alloy can be estimated by analysis of the DNE. Thus we calculated DNE barriers of respective phases in DSH and DSL, and compare them with experimental results.

Nucleation of crystallographic defects such as dislocations can be described as a stress-assisted, thermally activated process involving activation energy for nucleation [37-39]. This energy barrier can be overcome with the assistance of the applied stress, appropriate thermal fluctuations at finite temperatures, or a combination of both thermal and mechanical energy. In this research, the simple theoretical dislocation nucleation model was applied for compare DNE of each phase in same thermal condition [37, 40]. Nucleation energy of dislocation loop in this model is defined as followed equation:

$$J = 2\pi R \frac{Gb^2}{8\pi} \left[\frac{2-\nu}{1-\nu} \left(\ln \frac{8R}{\rho} - 2 \right) + \frac{1}{2} \right] + \gamma_{sf} \pi R^2 - b\tau \pi R^2 \quad (2-5)$$

where J is the energy barrier for homogeneous dislocation loop

nucleation, R is the radius of dislocation loop, G is the shear modulus, b is the length of Burgers vector, ν is the Poisson's ratio, ρ is the effective core cut-off radius of dislocation loop, γ_{SF} is the stacking fault energy (SFE) and τ is the applied shear stress [37, 40, 41]. The first term in Eq. (2-5) is the elastic energy. The second term is for the SFE because a partial (instead of perfect) dislocation can be nucleated. In this research, as conventionally known, α was regarded it generates perfect dislocation. In case of γ , J was calculated regarding it generates partial dislocation since partial dislocation will be nucleated easier than perfect dislocation [37]. The last term represents the work done by the applied shear stress, which drives dislocation nucleation. The energy barrier is changed by applied shear stress. While applied shear stress becomes higher, energy barrier J becomes lower. Then when J reaches to 0, dislocation loop is nucleated and material starts plastic deformation. Thus applied shear stress that J becomes 0 can be regarded as shear stress for dislocation nucleation, τ_{dn} . So τ_{dn} can be calculated as a function of radius of dislocation loop. If first pop-in was cause by dislocation nucleation, DNE barrier of $\alpha_{(DSH)}$ must be greater than $\gamma_{(DSH)}$, since $\alpha_{(DSH)}$ has higher elasto-plastic transition stress than $\gamma_{(DSH)}$ in nanoindentation. Therefore calculated τ_{dn} value of $\alpha_{(DSH)}$ will be higher than $\gamma_{(DSH)}$ for same radius of dislocation loop. By the same token, $\alpha_{(DSL)}$ and $\gamma_{(DSL)}$ will have similar τ_{dn} for same radius of dislocation loop.

In order to calculate J , shear modulus G was calculated from previously measured elastic modulus by L-D curve analysis with following equation.

$$G = \frac{E}{2(1+\nu)} \quad (2-6)$$

where E is elastic modulus, ν is Poisson's ratio [42]. By this equation, eq. (2-5) can be stated as follows.

$$J = R \frac{Eb^2}{8(1+\nu)} \left[\frac{2-\nu}{1-\nu} \left(\ln \frac{8R}{\rho} - 2 \right) + \frac{1}{2} \right] + \gamma_{SF} \pi R^2 - b\tau \pi R^2 \quad (2-7)$$

And Poisson's ratio was obtained from reference experimental data of stainless steel [43]. Poisson's ratios of austenitic stainless steel and ferritic stainless steel were also within range of 0.27 to 0.33 [42, 43]. Within this range, Poisson's ratio hardly affect to J . Thus in this analysis, Poisson's ratio was defined as 0.29 which is conventionally used for austenitic and ferritic Ni-Cr stainless steel [32, 33]. Effective core radius of dislocation loop is normally set as half-length of burgers vector in metallic materials [37].

The length of Burgers vector, b of each phase was measured by X-ray Diffraction (XRD). The X-ray diffraction spectrum for specimen measured

over the 2θ range from 40° to 100° , using New D8 Advance of Bruker. Reference XRD data of α and γ was used for lattice parameter analysis [44, 45]. Measured value of lattice parameter and length of Burgers vector is indicated in Table 2.3.

And lastly, SFE was measured. SFE has much influence in calculating DNE barrier J when partial dislocation was nucleated. Thus analysis of neutron diffraction profiles was performed for precise measuring of SFE. The procedure for line profile analysis adopted in this study consists of two independent schemes, size-strain analysis of whole profiles and peak shift analysis of individual reflections. To evaluate more accurate parameters, the size and strain analysis were performed through two sequential steps: the Rietveld whole-profile fitting and the double-Voigt size-strain analysis [46]. Mean square (MS) strain and stacking fault probability (SFP) of $\gamma_{(DSH)}$ and $\gamma_{(DSL)}$ were calculated by this sequential method. Calculated values of MS strain and SFP are stated in table 2.4. The analyzed results are values at the loading of ~ 750 MPa (DSH) and ~ 700 MPa (DSL). The SFE represents the easiness against dissociation of a perfect dislocation into two partial dislocations and the propensity for formation of stacking fault. In determination of SFE using diffraction methods, Reed and Schramn's formula [47] has been widely used, as follows:

$$\gamma_{SF} = \frac{K_{111}\omega_0 G a_0 A^{-0.37} \langle \varepsilon_{50}^2 \rangle_{111}}{\pi\sqrt{3} P_{SF}} \quad (2-8)$$

Here, $K_{111}\omega_0$ is proportional constant, a_0 is true lattice parameter, A is anisotropy parameter, G is shear modulus, $\langle \varepsilon_{50}^2 \rangle_{111}$ is MS strain and P_{sf} is SFP, respectively. The values of G were calculated from Elastic modulus measured by L-D curve analysis. Other material data were taken from the literature, $K_{111}\omega_0 = 6.6$ [47] and $A = 3.78$ [48]. From the calculated values of MS strain and SFP, the SFE could be determined from their ratio of MS strain to SFP together with predetermined materials constants. Obtained values of SFE are indicated in table 2.5.

Using these parameters, DNE barrier J was calculated and τ_{dn} was plotted as a function of radius of dislocation loop like Fig. 2.18. As you see in these graphs, calculated τ_{dn} of $\gamma_{(DSH)}$ is lower than $\alpha_{(DSH)}$ for same radius of dislocation loop, because $\alpha_{(DSH)}$ has higher DNE barrier $\gamma_{(DSH)}$. On the other hand, calculated τ_{dn} of $\alpha_{(DSL)}$ and $\gamma_{(DSL)}$ is similar. As expected, these results correctly correspond with pop-in tendency from nanoindentation as previously shown in Fig. 2.13. And comparing experimental pop-in stress region with calculated τ_{dn} , radius range of nucleated dislocation loop is almost fixed from 1.5nm to 3.0nm in every cases. That is, it can be thought that radius of dislocation loop when pop-in occurs is within range from 1.5 nm to 3.0nm. It

is interesting result that radius of dislocation loop when pop-in can be estimated by this analysis. If we can predict radius range of nucleated dislocation loop, we also can evaluate other parameter like SFE or G from pop-in stress. By all these results and discussion, we could conclude that shear stress for dislocation nucleation is closely related with the maximum shear stress at nanoindentation pop-in, and difference of elasto-plastic transition stress can be quite reasonably explained by DNE.

	DSH		DSL	
	α	γ	α	γ
Lattice parameter (nm)	0.289	0.364	0.289	0.363
Type of dislocation	Perfect	Partial	Perfect	Partial
Length of Burgers vector (nm)	0.257	0.148	0.257	0.148

Table 2.3 Lattice parameter and length of Burgers vector measured by XRD.

	$\gamma_{(DSH)}$	$\gamma_{(DSL)}$
Mean square strain ($\mu\epsilon$)	11.44	28.90
Stacking fault probability	0.011	0.012

Table 2.4 MS strain and SFP of $\gamma_{(DSH)}$ and $\gamma_{(DSL)}$.

	$\gamma_{(\text{DSH})}$	$\gamma_{(\text{DSL})}$
Sacking fault energy (mJ/m ²)	20.0	56.4

Table 2.5 SFE of $\gamma_{(\text{DSH})}$ and $\gamma_{(\text{DSL})}$.

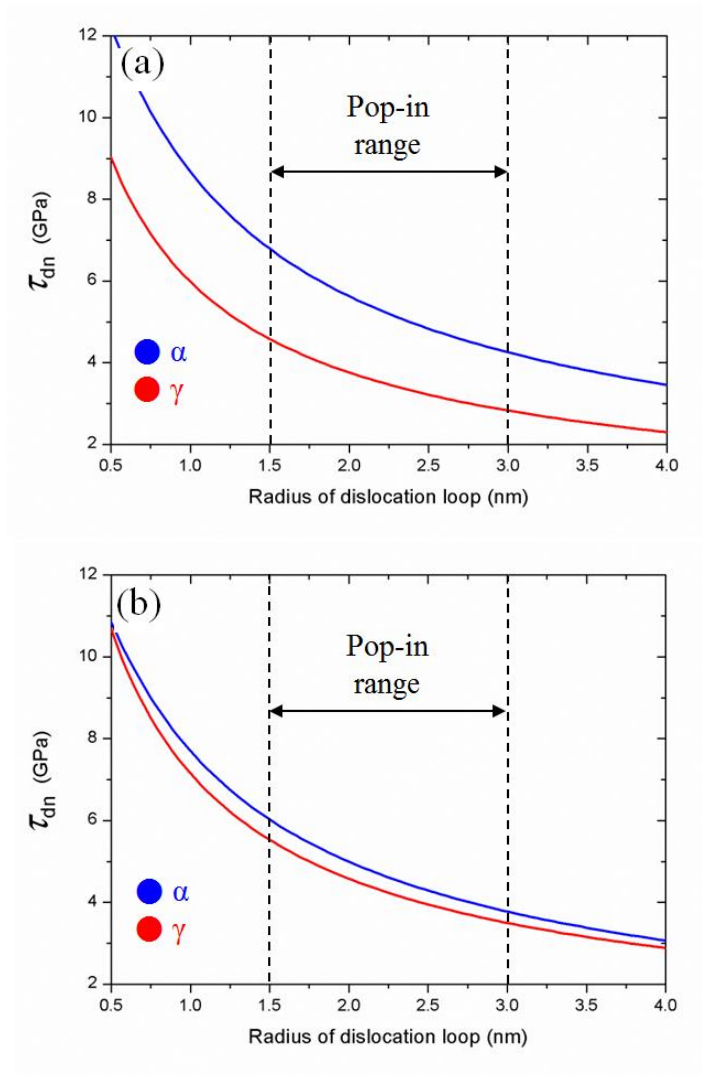


Figure 2.18 Shear stress of dislocation nucleation, τ_{dn} for (a) DSH and (b) DSL, as function of radius of dislocation loop.

2.6 Summary

In this research, mechanical behavior, especially plastic yielding behavior of DSS was analyzed by combining various experimental techniques. EBSD, nanoindentation and in-situ neutron diffraction were performed to define and behavior of respective phases in DSS, and all results were linked each other and analyzed. Relationship between the small-scale nanoindentation behavior and the macro-scale tensile behaviour was investigated by these procedures, and interesting results could be derived. First, the tendency of plastic yielding in macro-scale could be well described by the nanoindentation data for each phase. The results from these two different approaches were corresponded well each other. Thus we could conclude that tendency of maximum shear stress when pop-in occurs can represent tendency of intrinsic yield stress of respective phases in DSS. By these results, tendency of macroscopic yield stress of DSH and DSL was explained. And In addition, DNE was calculated to explain different elasto-plastic transition tendency between DSH and DSL. The used parameters for calculation were obtained from nanoindentation and in-situ neutron diffraction. AS a result, we found shear stress for dislocation nucleation is closely related with the elasto-plastic transition stress. Thus finally, by all these results, we could conclude that the difference of elasto-plastic transition stresses in both DSS can be explained by DNE and the SFE in γ could be evaluated by nanoindentation based DNE calculation.

2.7 References

- [1] H.W. Hayden, R.C. Gibson, J.H. Brophy, *Sci Am*, 220 (1969) 28-&.
- [2] N. Ridley, *Mater Sci Tech Ser*, 6 (1990) 1145-1156.
- [3] J.M. Cabrera, A. Mateo, L. Llanes, J.M. Prado, M. Anglada, *J Mater Process Tech*, 143 (2003) 321-325.
- [4] J.O. Nilsson, *Mater Sci Tech Ser*, 8 (1992) 685-700.
- [5] K.H. Lo, C.H. Shek, J.K.L. Lai, *Mat Sci Eng R*, 65 (2009) 39-104.
- [6] F. Dupoirion, J.P. Audouard, *Scand J Metall*, 25 (1996) 95-102.
- [7] S. Harjo, Y. Tomota, P. Lukas, D. Neov, M. Vrana, P. Mikula, M. Ono, *Acta Mater*, 49 (2001) 2471-2479.
- [8] T.H. Lee, H.Y. Ha, J.Y. Kang, B. Hwang, W. Woo, E. Shin, *Scripta Mater*, 67 (2012) 141-144.
- [9] Y. Tomota, H. Tokuda, Y. Adachi, M. Wakita, N. Minakawa, A. Moriai, Y. Morii, *Acta Mater*, 52 (2004) 5737-5745.

- [10] D.G. Carr, M.I. Ripley, D.W. Brown, S.C. Vogel, T.M. Holden, *Journal of Nuclear Materials*, 359 (2006) 202-207.
- [11] S. Harjo, Y. Tomota, M. Ono, *Acta Mater*, 47 (1998) 353-362.
- [12] G.E. Bacon, *Neutron diffraction*, 3d ed., Clarendon Press, Oxford Eng., 1975.
- [13] N. Jia, R. Lin Peng, Y.D. Wang, S. Johansson, P.K. Liaw, *Acta Mater*, 56 (2008) 782-793.
- [14] Y. Tomota, P. Lukas, S. Harjo, J.H. Park, N. Tsuchida, D. Neov, *Acta Mater*, 51 (2003) 819-830.
- [15] N. Jia, R.L. Peng, D.W. Brown, B. Clausen, Y.D. Wang, *Metall Mater Trans A*, 39A (2008) 3134-3140.
- [16] T.H. Ahn, C.S. Oh, K. Lee, E.P. George, H.N. Han, *J Mater Res*, 27 (2012) 39-44.
- [17] K. Lee, S.J. Park, Y.S. Choi, S.J. Kim, T.H. Lee, K.H. Oh, H.N. Han, *Scripta Mater*, 69 (2013) 618-621.
- [18] W.C. Oliver, G.M. Pharr, *J Mater Res*, 7 (1992) 1564-1583.

- [19] W.C. Oliver, G.M. Pharr, *J Mater Res*, 19 (2004) 3-20.
- [20] G.M. Pharr, *Mat Sci Eng a-Struct*, 253 (1998) 151-159.
- [21] G.M. Pharr, W.C. Oliver, F.R. Brotzen, *J Mater Res*, 7 (1992) 613-617.
- [22] J.W. Simmons, *Mat Sci Eng a-Struct*, 207 (1996) 159-169.
- [23] S. Pathak, S. R. Kalidindi, *Mat Sci Eng R*, 91 (2015) 1-36.
- [24] H.J. Chang, H.N. Han, M.C. Fivel, in: *Key Engineering Materials*, 2007, pp. 925-930.
- [25] H. Bei, Y.F. Gao, S. Shim, E.P. George, G.M. Pharr, *Phys Rev B*, 77 (2008).
- [26] H. Bei, E.P. George, J.L. Hay, G.M. Pharr, *Phys Rev Lett*, 95 (2005).
- [27] J. Li, K.J. Van Vliet, T. Zhu, S. Yip, S. Suresh, *Nature*, 418 (2002) 307-310.
- [28] C. Begau, A. Hartmaier, E.P. George, G.M. Pharr, *Acta Mater*, 59 (2011) 934-942.
- [29] C.A. Schuh, J.K. Mason, A.C. Lund, *Nat Mater*, 4 (2005) 617-621.

- [30] S. Shim, H. Bei, E.P. George, G.M. Pharr, *Scripta Mater*, 59 (2008) 1095-1098.
- [31] A. Gouldstone, H.J. Koh, K.Y. Zeng, A.E. Giannakopoulos, S. Suresh, *Acta Mater*, 48 (2000) 2277-2295.
- [32] H.M. Ledbetter, M.W. Austin, *Mater Sci Eng*, 70 (1985) 143-149.
- [33] G.E. Dieter, *Mechanical metallurgy*, McGraw-Hill, 1986.
- [34] J.R. Morris, H. Bei, G.M. Pharr, E.P. George, *Phys Rev Lett*, 106 (2011) 165502.
- [35] J.J. Moverare, M. Oden, *Metall Mater Trans A*, 33 (2002) 57-71.
- [36] B. Clausen, T. Lorentzen, M.A.M. Bourke, M.R. Daymond, *Mat Sci Eng a-Struct*, 259 (1999) 17-24.
- [37] J.P. Hirth, J. Lothe, *Theory of Dislocations*, Krieger Publishing Company, 1982.
- [38] C.A. H, *Dislocations and Plastic Flow in Crystals*, Clarendon Press, 1953.
- [39] J.R. Rice, R. Thomson, *Philos Mag*, 29 (1974) 73-97.
- [40] S. Aubry, K. Kang, S. Ryu, W. Cai, *Scripta Mater*, 64 (2011) 1043-1046.

- [41] T. Ohmura, K. Tsuzaki, *J Phys D Appl Phys*, 41 (2008).
- [42] D.N. LEE, *TEXTURE AND RELATED PHENOMENA*, The Korean Institute of Metals and Materials, 2006.
- [43] T.H. Courtney, *Mechanical Behavior of Materials: Second Edition*, Waveland Press, 2005.
- [44] A.W. Hull, *Phys Rev*, 10 (1917) 661-696.
- [45] W.P. Davey, *Phys Rev*, 25 (1925) 753-761.
- [46] T.H. Lee, E. Shin, C.S. Oh, H.Y. Ha, S.J. Kim, *Acta Mater*, 58 (2010) 3173-3186.
- [47] R.P. Reed, R.E. Schramm, *J Appl Phys*, 45 (1974) 4705-4711.
- [48] S. Lin, H. Ledbetter, *Mat Sci Eng a-Struct*, 167 (1993) 81-85.

Part II

3. Investigation of correlation between strain and crystal orientation by EBSD supported DIC

3.1 Introduction

Understanding deformation mechanisms is essential to improving mechanical properties of materials. In order to understand how the plastic strain, it is important to know the magnitude of plastic strain on a microstructural scale (hereafter, local plastic strain). Even if the macroscopic strain appears uniform and homogeneous, local strain of polycrystalline material is inhomogeneous due to the anisotropy of crystal grains and their random or nearly random orientation distribution [1-3]. On a microstructural scale, plastic deformation causes crystallographic slip and the geometrically necessary dislocations. The crystal orientation is changed due to the dislocations and may show fluctuations of several degrees even in the same grain. For this reason, several attempts to measure plastic strain have been made by using electron backscatter diffraction (EBSD). EBSD, in conjunction

with scanning electron microscopy (SEM), is one of the most promising techniques for measuring the change in local crystal orientation. This is a scanning electron microscope (SEM) based diffraction technique for automated mapping of crystal orientations from bulk samples, which is now widely used in materials characterization [4-6]. It has been shown that scalar parameters obtained from crystal orientations of the scanned area correlate with the magnitude of macroscopic plastic strain induced in materials [3, 7, 8]. Therefore, by using this correlation, the macroscopic plastic strain can be estimated from crystal orientations obtained by EBSD measurements. The degree of the plastic strain can be estimated by utilizing either changes in the diffraction pattern quality [9] or changes in local orientation [3, 7, 10, 11], which are measured using EBSD. On that basis, many researchers have regarded area which has high local misorientation value as severe deformed area [8, 12-18]. However, quantitative amount of deformation is cannot be measured directly by EBSD analysis. Of course, recent researches reported that value some indicators of misorientation become greater when deformation becomes more severe, statistically [19]. However, these results cannot directly interpret that value of local metric misorientation regard as amount of local deformation. Until a recent date, relationship between strain and misorientation is not investigated clearly. It is dangerous to directly define deformation by orientational information without additional detailed investigation about relationship between strain and misorientation. Thus for

appropriate strain estimating by EBSD analysis, it is essential to define relationship between deformation and misorientation.

In order to link crystal orientation information with deformation, mapping local strain and crystal orientation should be carried out together on same area. And we thought it can be accomplished by using digital image correlation (DIC) supported by EBSD technique. DIC [20, 21] is a non-contact, adaptable metrology technique for strain field measurement that can be utilized on a variety of length scales ranging from civil engineering structures[22] to microstructures of metallic specimens [23, 24]. Contrary to EBSD strain analysis, quantitative local strain can be measured and mapped directly by DIC [25]. If DIC analysis and EBSD can be performed on same area during deformation, local strain and orientational information can be matched pixel by pixel.

The DIC algorithm tracks a grayscale pattern on the deforming surface step by step in a small area called a subset. To track the fullfield surface deformation, an isotropic random speckle pattern is required on the specimen surface. This speckle pattern can be either intrinsic (from existing surface features) or extrinsic, as in a deposited pattern. The optimal feature size of a speckle pattern is reportedly 2 to 3 pixels for a recorded image [26]. Therefore, different patterning methods are needed to meet this requirement at different

scales. While there have been multiple investigations reporting the use of DIC in making microscale strain measurements, one of the major challenges in such endeavors is producing a nanoscale, random, and isotropic speckle pattern required for DIC. By the way, this speckle pattern for DIC cause critical problem to scan EBSD. Since EBSD is very sensitive about surface condition, the beam/specimen interaction layer must be relatively strain free and clean for patterns to be obtained. Thus in many cases, fine mechanical polish is required, and if it is necessary, electropolish or ion-beam milling must be carried out to ensure surface cleanliness. Generally, Pt, Au or C particles are disposed on surface of specimen for speckle patterning. These particles disturb contact of beam to specimen, thus orientational information around those particles cannot be obtained by EBSD [27]. However, in order to match local strain with relevant orientational information, well indexed precise EBSD image is indispensable. Some researcher enhanced raw data of EBSD before analysis because EBSD image is severely damaged by speckle patterning [27, 28]. But orientational information can be distorted by enhancing EBSD raw data. Especially, misorientation is highly dependent on orientation of neighbor pixel. If EBSD data is distorted, the misorientation values from that data are unreliable. Thus new method which enables to perform DIC analysis with measuring precise EBSD data should be developed for this research.

In this paper, EBSD supported DIC (digital image correlation) analysis was tried using full annealed pure Cu specimen, in order to investigate relationship between local strain and misorientation. For precise EBSD images with gray scale pattern for DIC, new patterning technique using carbon coat was developed and compared with conventional speckle patterning method. Subsequently, selected area of Cu specimen was captured while tensile test by in-situ SEM equipped with a deformation module. The area was also scanned by EBSD. The sequential SEM images during deformation were analyzed by DIC and quantitative strain maps were drawn. As a result, accurate quantitative strain, precise microstructure and texture of the selected area could be measured together. Then Kernel average misorientation (KAM) map and grain average misorientation (GAM) map were drawn and directly compared with local strain, in order to correlate local strain and misorientation.

3.2 Experimental procedures-

3.2.1. Material and processing

A commercial pure copper sheet (purity 99.9%) with thickness of 1 mm was used for this research. Prior to the test, the sheet was cut as dog-bone shape along the rolling direction with a gauge length of 20 mm and a width of 4 mm for uniaxial tension. And then the specimen was annealed at 973 K for 240 min in argon atmosphere in order to diminish the rolling structures and to release intragranular dislocations. And then the material was furnace cooled. EBSD was performed for getting information about micro structure of the specimen. Every EBSD tests in this research were carried out in a field emission SEM (Hitachi SU70). The EBSD images were analyzed by TSL OIM collection 6 and TSL OIM analysis 6.1, EDAX Instruments. The accelerating voltage and probe current were set at 15 kV and 4 nA, respectively. Step size for EBSD mapping was 1 μm . In order to get reliable SEM/EBSD image, the specimen was prepared by fine polishing with SiC paper and repeated electro-polishing. The average grain size after annealing is about 10.4 μm and annealed twins are frequently observed in the sample as shown in Fig. 3.1. Specific strong texture was not observed.

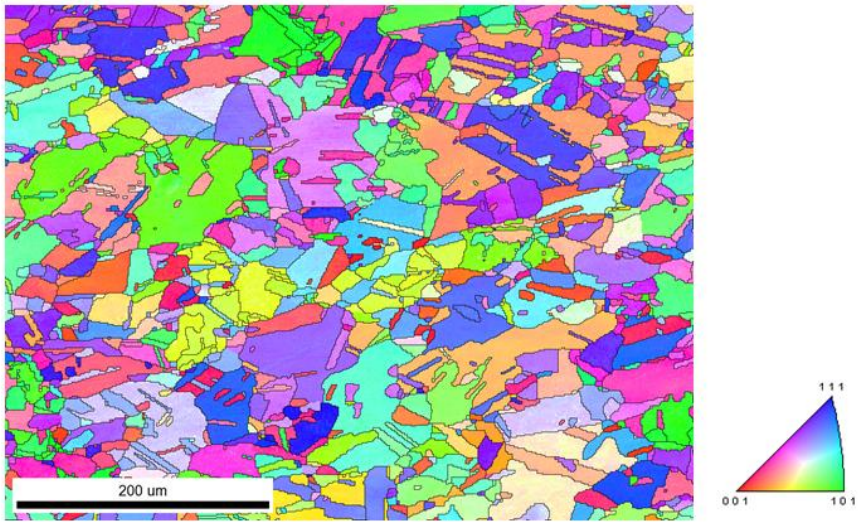


Figure 3.1 ND orientation map of Cu specimen.

3.2.2. Developing carbon coat patterning method

As previously stated, gray scale pattern is required on surface of specimen for DIC [21, 22]. Thus patterning process should be performed on Cu specimen for this experiment. However, conventionally used speckle patterning method was inappropriate for this research since the speckles disturb scanning EBSD [27, 28]. In order to overcome this problem, new patterning technique using carbon coat was developed.

Carbon coat is generally used for enhancing electro conductivity of surface to obtain clean SEM/EBSD image. After carbon is coated on surface of specimen, brightness of SEM image changes but the coat do not disturb collecting EBSD pattern. Carbon coat patterning method for DIC was developed from this phenomenon. If random pattern is drawn by carbon coat on surface of metallic specimen, that region is observed on SEM image as gray scale pattern caused by difference of electro conductivity, without damage to EBSD. This carbon coat patterned area can be used for DIC analysis, and precise EBSD image of that area can be also measured.

Schematic image of carbon coat patterning method is shown as Fig. 3.2. At first, polymer webs which have 0.5~2.0 μm diameter are randomly disposed on surface of specimen. In this research, polychloroprene was used for drawing out polymer web. Diameter of polymer web varies with

magnification of SEM image. 2~3 times the size of SEM pixel is appropriate for the diameter of polymer web since the size of web is resolution of pattern for DIC. Then, carbon is coated on the specimen. At this step, disposed polymer webs act as masking for carbon coat. The thickness of carbon coat is 150~200Å. The thickness affects to contrast of random pattern. Carbon coat layer becomes thicker, contrast of pattern become stronger. However, excessively thick carbon coat cause low image quality of EBSD. Subsequently, disposed polymer webs are removed by sonic cleaning in acetone. Carbon coat layer remains on area which is not masked by polymer web. Thus finally, random carbon coat pattern can be generated on surface of specimen.

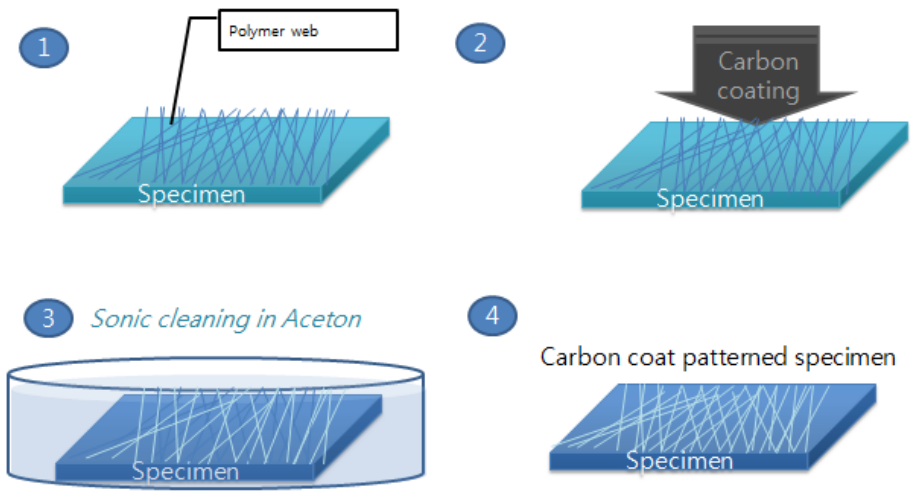


Figure 3.2 Schematic image of carbon coat patterning method.

In order to compare carbon coat patterning method with speckle patterning method, SEM and EBSD images were measured before and after patterning. At first, 10% tensile deformation was applied to Cu specimen for increasing local misorientation, since comparing KAM map of before and after patterning. Then selected area of two Cu specimens were marked by micro indenter as $400 \times 400 \mu\text{m}$ square then captured by SEM, and scanned by EBSD. Subsequently, speckle patterning and carbon coat patterning were performed on respective specimen. Disposed particle for speckle patterning is carbon power which has $0.5 \sim 2.0 \mu\text{m}$ diameter. And SEM and EBSD image of previously selected area was obtained after patterning. Pixels which have confidence index (CI) value under 0.1 were excluded for reliable analysis on EBSD image. As shown in Fig. 3.3, EBSD image was severely damaged after speckle patterning. Before speckle patterning, indexing ratio of EBSD was 91% but the ratio dropped to 54% after patterning. Then KAM map was drawn as Fig. 3.4, and high angle misorientation distribution was also plotted as Fig. 3.5 for investigating damage effect caused by the speckles. As previously stated, some researchers used enhanced EBSD data for analysis [27, 28], thus enhanced data was also regarded and compared together. In the same way with references, the raw EBSD data was first processed using a grain confidence index (CI) standardization procedure. A secondary process called single iteration grain dilation was carried out. As shown in Fig. 3.4, KAM

value from damaged EBSD image was severely distorted compared with well indexed (before speckle patterned) image. And after enhancing damaged EBSD image, shape of microstructure was partly recovered. However, local misorientation was severely distorted and even shape of some grains was twisted. High angle misorientation distributions of damaged data and enhanced data were also quite different with original information as indicated by Fig. 3.5. Thus, it is reasonable to conclude that EBSD data scanned from speckle patterned surface is unreliable.

And then, SEM and EBSD images of before and after carbon coat patterning were measured in same procedure as speckle patterned specimen. Compared to Fig. 3.6 (a) and (b), random gray scale pattern appeared definitely on SEM image. But contrary to speckle patterning method, EBSD image was scarcely damaged by patterning as it can be seen from Fig. 3.6 (c) and (d). Before speckle patterning, indexing ratio of EBSD was 92% and the ratio was 89% after carbon coat patterning. As shown in Fig. 3.7 and 3.8, KAM maps and high angle distributions were not distorted by patterning even in enhanced data. Thus we can conclude that carbon coat patterning hardly affect to image quality of EBSD, and DIC analysis can be performed with scanning reliable EBSD data at the same time by using this method.

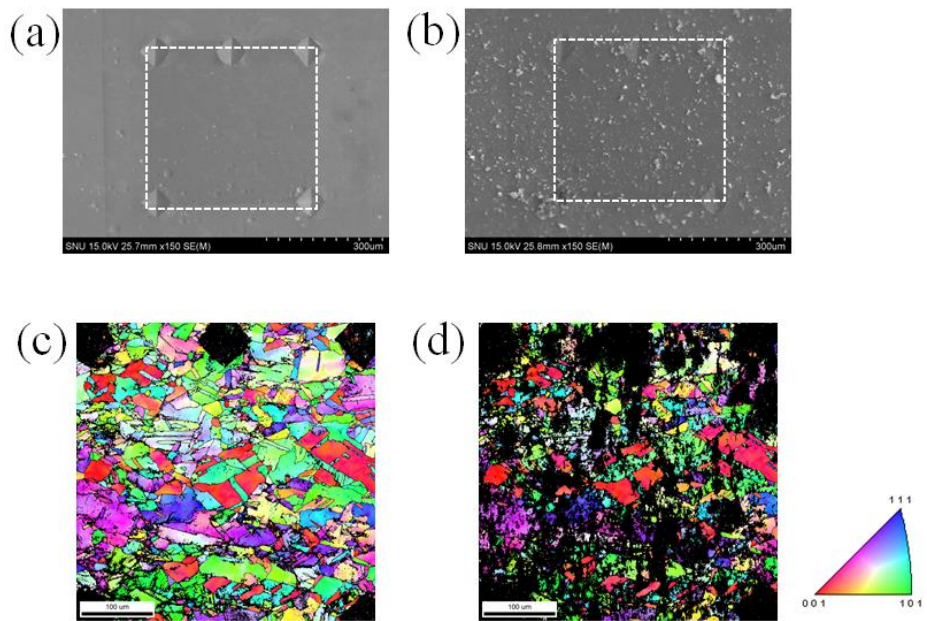
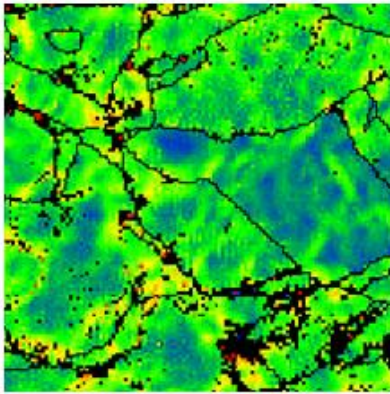
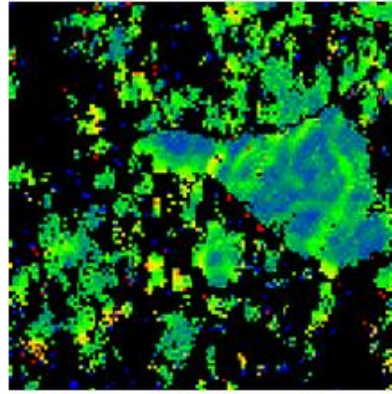


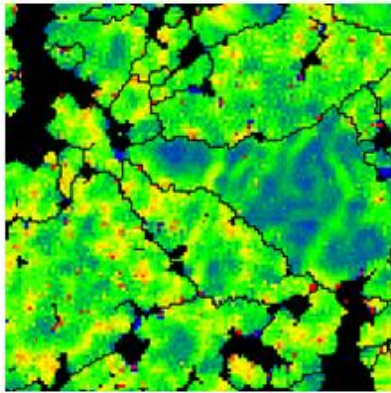
Figure 3.3 SEM image of Cu specimen (a) before patterning, (b) after speckle patterning and ND orientation map of Cu specimen (c) before patterning, (d) after speckle patterning.



(a)

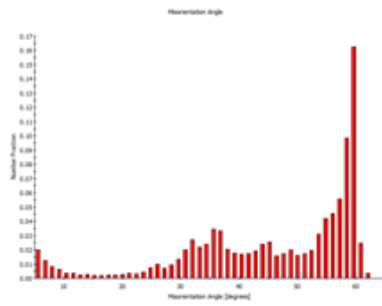


(b)

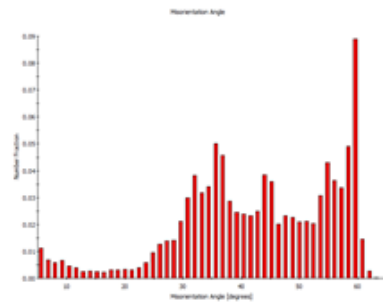


(c)

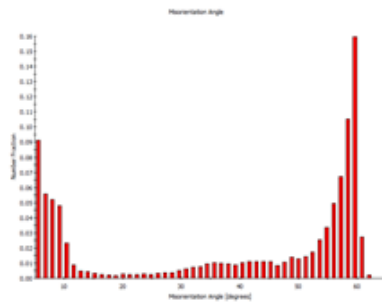
Figure 3.4 KAM map of Cu specimen (a) before patterning, (b) after speckle patterning and (c) enhanced KAM map from EBSD data of patterned specimen.



(a)



(b)



(c)

Figure 3.5 High angle misorientation distribution of Cu specimen (a) before patterning, (b) after speckle patterning and (c) enhanced result from EBSD data of patterned specimen.

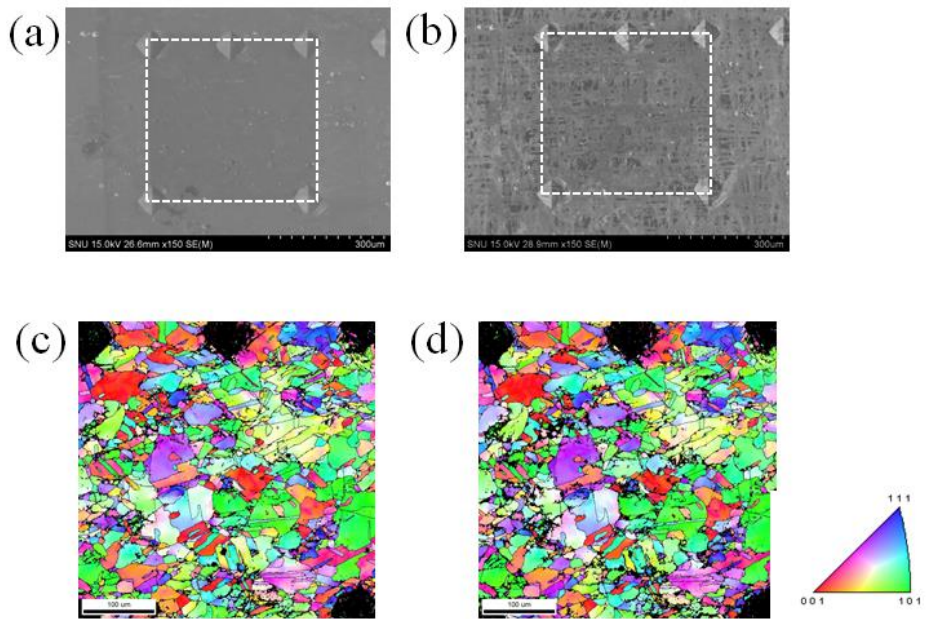
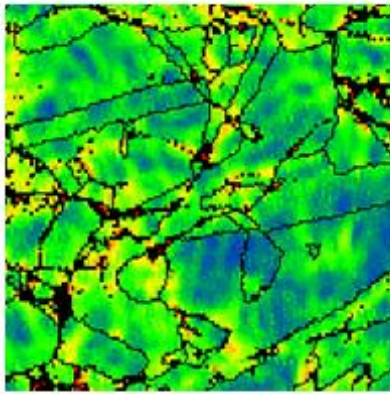
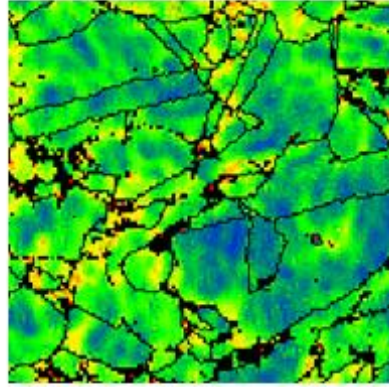


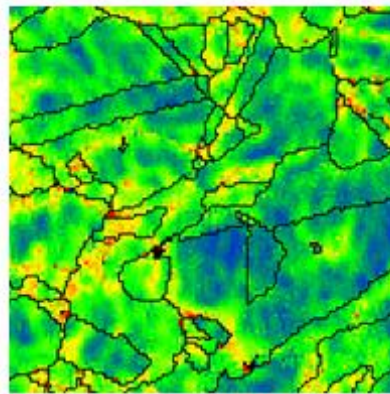
Figure 3.6 SEM image of Cu specimen (a) before patterning, (b) after carbon coat patterning and ND orientation map of Cu specimen (c) before patterning, (d) after carbon coat patterning.



(a)



(b)



(c)

Figure 3.7 KAM map of Cu specimen (a) before patterning, (b) after carbon coat patterning and (c) enhanced KAM map from EBSD data of patterned specimen.

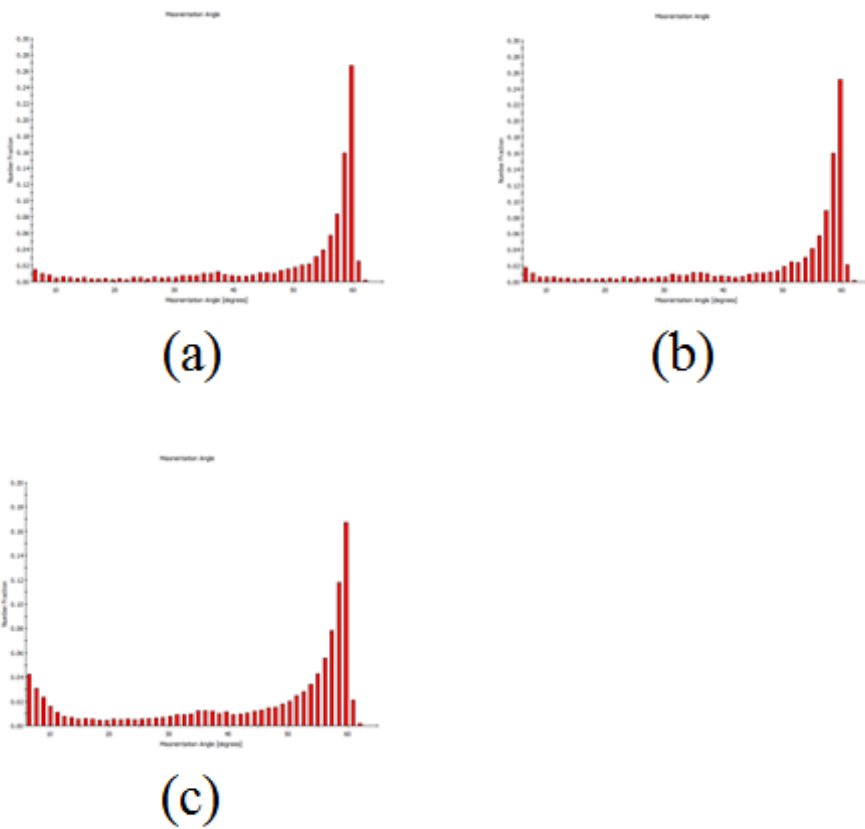


Figure 3.8 High angle misorientation distribution of Cu specimen (a) before patterning, (b) after speckle patterning and (c) enhanced result from EBSD data of patterned specimen.

3.2.3. DIC by using in-situ SEM image with EBSD

At first, gray scale random pattern was applied on prepared tensile specimen by using carbon coat method as Fig 3.9. Tensile tests were carried out in-situ in a SEM vacuum chamber at room temperature using the deformation devices system (DDS) made by Kammrath & Weiss shown in Fig 3.10. The dimensions of the tensile stage (150mm × 55mm × 220mm) are small enough to be placed inside a SEM chamber. Mounted inside a SEM vacuum chamber, the tensile stage can be controlled by DDS control unit via a feed-through. The tensile module was capable of achieving a maximum load of 5 kN. The SEM used for this in-situ experiment (S-4300SE, Hitachi) equipped with a high-sensitivity EBSD system (CrystAlign e-Flash^{HR}, Bruker), and image distortion was evaluated prior to the actual tensile test. A SEM and EBSD image were recorded prior to deformation of the sample. DIC analysis was then conducted on this nondeformed reference SEM image to determine the pseudo-strain introduced by image distortion. Entire area of SEM image was scanned by EBSD, and step size for EBSD mapping was 1 μm. Thus SEM images were resized to same spatial resolution with EBSD, 1 μm pixel⁻¹ for data matching. Used Image size of SEM and EBSD is 500x375 pixels.

A strain rate of $4.0 \times 10^{-4} \text{s}^{-1}$ was selected for a quasi-static tensile testing. During tensile tests, SEM images were recorded after the test was

interrupted every 10 seconds. After each step, the sample was held for at least 1 minute to allow the load to stabilize. The test was finished at tensile strain 9.2%, since strain rate could not be kept as same rate because of strain hardening. Total 23 sequential SEM images were captured during deformation, and whole area of final SEM image was also scanned by EBSD. All the SEM and EBSD images were recorded at the same magnification. Series of deforming SEM images were imported into the originally coded 2D DIC program developed by Ahn et al. [29] and an undeformed image was used as a reference image. Algorithm of the applied 2D DIC program was coded based on classical Newton–Raphson method [30-34]. But unlike conventional registration methods, control points were placed regularly to prevent biased distribution of feature points and find optimized correspondences by minimizing the cost function. The cost function is based on SIFT descriptors and considers the smoothness of motion and topological relations [29,35]. Then deformed images were compared to the first reference image. During deformation, the gray scale carbon coat pattern was traced and displacement fields of deformed images were generated. Then finally, maximum shear strains were calculated and mapped on EBSD image. We expect carbon coat patterning method for DIC and EBSD supported DIC analysis introduced in this paper can be widely used for analyzing strain with regarding texture.



Figure 3.9 SEM image of carbon coat patterned Cu specimen before deformation.

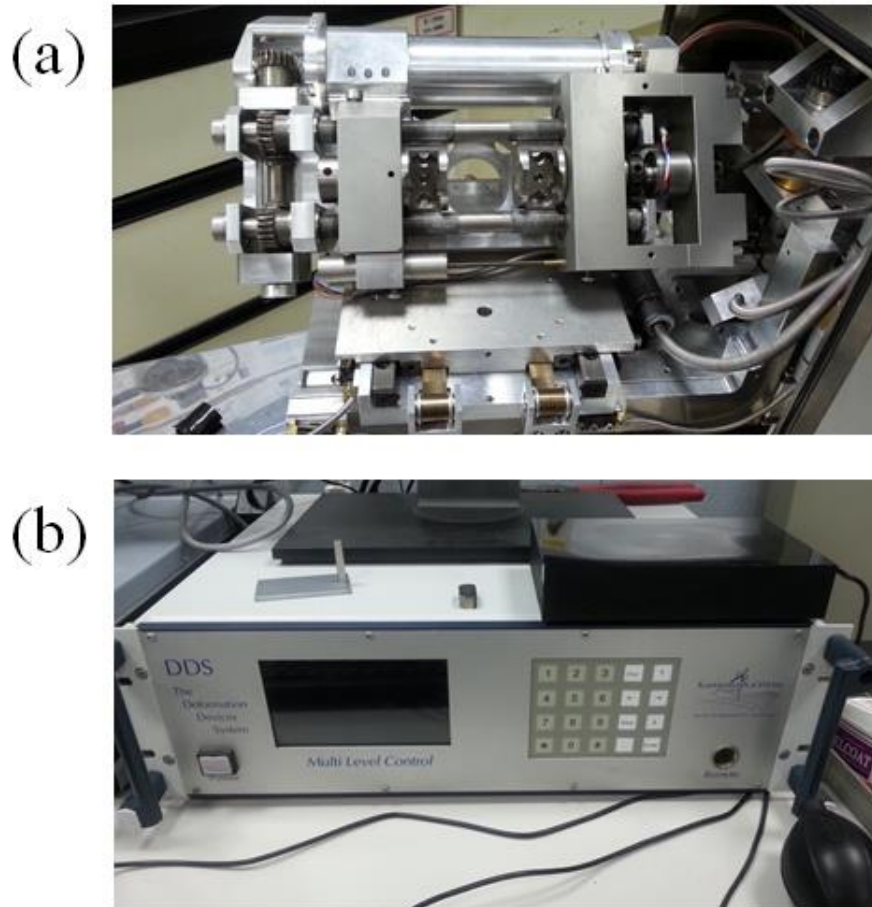


Figure 3.10 (a) Tensile stage and (b) control unit of deformation module.

3.3 Relation between strain and crystal orientation

ND orientation map after 9.2% tensile test are drawn as Fig. 3.11. As shown in the figures, precise EBSD image could be measured despite gray scale pattern on surface for DIC. Ratio of indexed pixels which have CI value over 0.1 on EBSD was 91%. And maximum shear strain map was also drawn as Fig. 3.12. In order to verify reliability, the strain was calculated by two different coordination and each result was compared. Maximum shear strain was calculated first in normal Cartesian coordinate system as Fig. 3.12 (a). And next, the strain was calculated again in 45° rotated coordination and indicated as Fig. 3.12 (b). If DIC analysis was carried out properly, the strain maps from two different coordination systems should be same, since maximum shear strain is isotropic value. As you seen in the Fig. 3.12, the maximum shear strain maps are correctly correlated. Thus we could conclude that the carbon coat patterns were sufficient to be traced for DIC analysis.

In order to compare local misorientation with local strain, KAM map was drawn as Fig. 3.13. Calculation of KAM was regarded to 2nd neighbor pixels of target pixel. Before deformation, crystal orientation was hardly distorted thus overall value of KAM was quite low, since the specimen was full annealed. And KAM was drastically developed after 9.2% tensile as shown in the figures. Comparing KAM map with maximum shear strain map (Fig 3.11

(b)), contrary to expectations, obvious correlation between KAM and local strain was not observed. For precise quantitative analysis, KAM value was plotted as function of maximum shear strain as indicated in Fig. 3.14. As shown in the graphs, maximum shear strain becomes greater as average value of KAM becomes greater, statistically. However, it is ambiguous to assert that KAM has direct, intimate relationship with local strains, since data points are spreaded too widely as known from indicated error bars. Followed by linking KAM to local strain, relation between GAM and grain average strain was analyzed. It is well known that overall GAM value increases during deformation [19]. Thus grain which has relatively high GAM value was often regarded as more deformed one [17]. In order to confirm this, GAM map and grain average maximum shear strain map after 9.2% tensile were drawn and compared each other. As shown in the Fig. 3.15 (a) and (b), overall GAM value quite increase after 9.2% tensile deformation as conventionally reported. And then, GAM map (Fig. 3.15 (b)) was compared with grain average maximum shear strain map (Fig. 3.16), and GAM value was also plotted as function of grain average maximum shear strain as indicated in Fig. 3.17. As shown in the graph, the data points were randomly scattered and meaningful relationship was not observed. As a result, we concluded it is hard to directly correlate GAM with grain average strain.

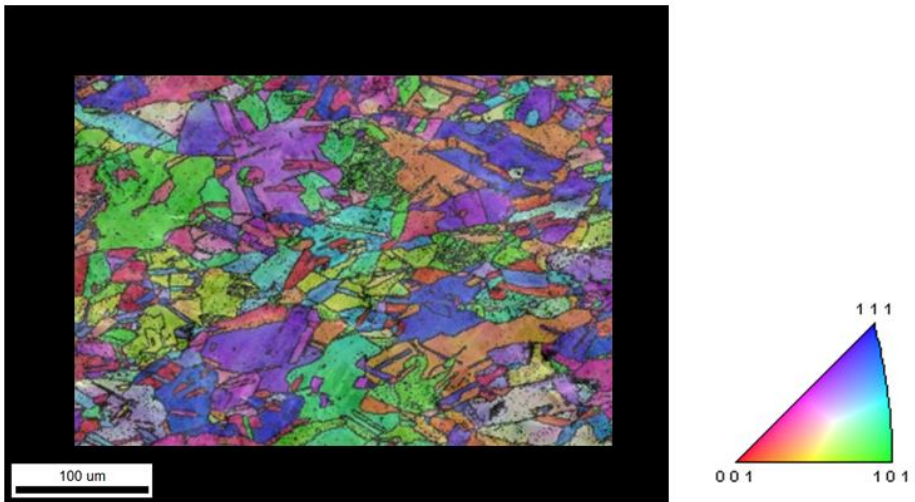
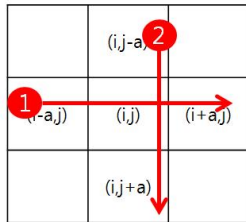
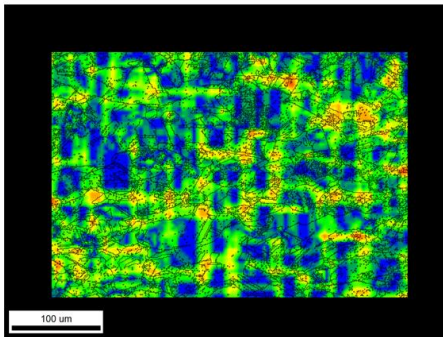


Figure 3.11 ND orientation map of Cu specimen after 9.2% tensile test.

(a) normal calculation



(b) 45° rotated calculation

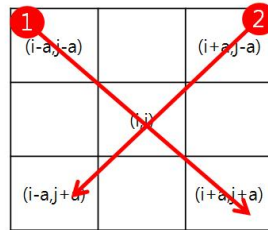
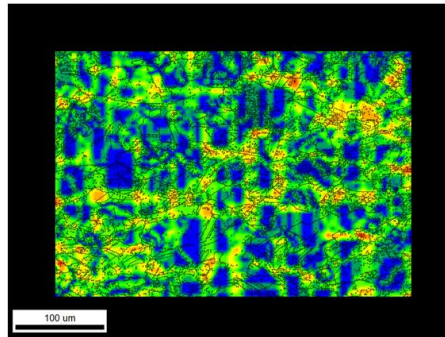
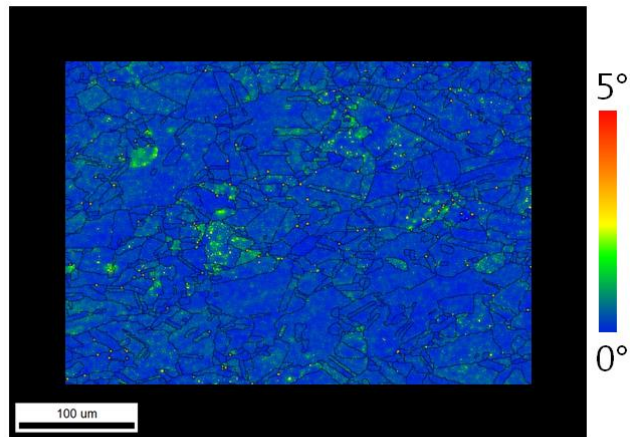


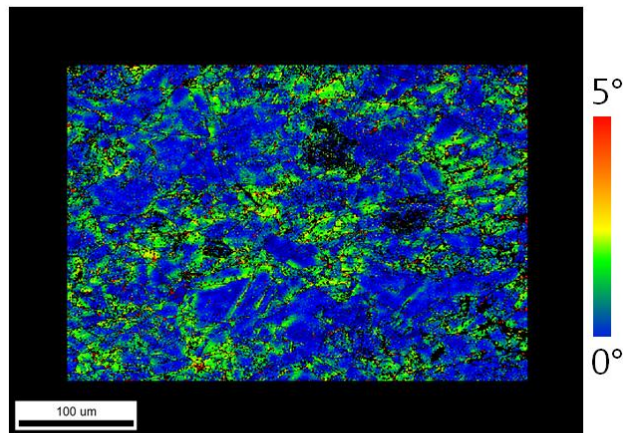
Figure 3.12 Maximum shear strain map calculated by (a) normal Cartesian coordination and (b) 45° rotated coordination.

Tensile Strain 0%



(a)

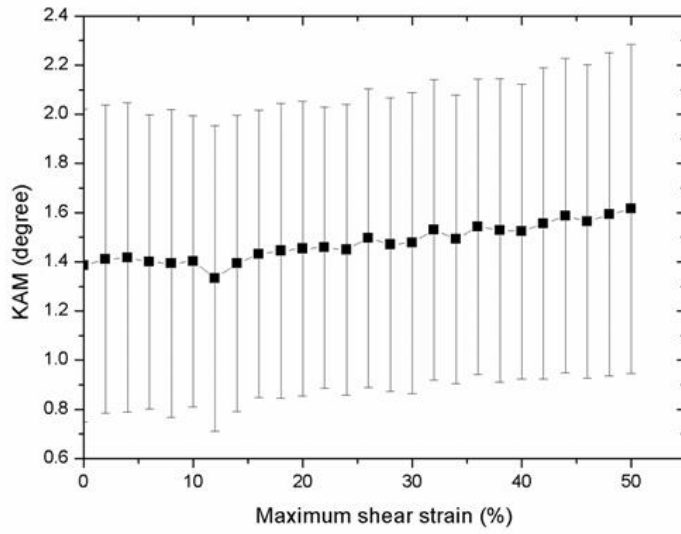
Tensile Strain 9.2%



(b)

Figure 3.13 KAM maps of (a) undeformed state and (b) 9.2% tensile deformed state.

(a)



(b)

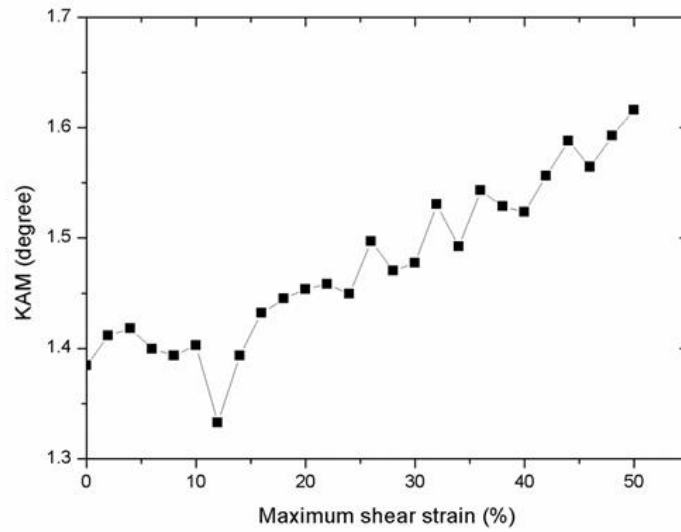


Figure 3.14 KAM developments as function of maximum shear strain of 9.2% tensile specimen (a) with error bars and (b) without error bars.

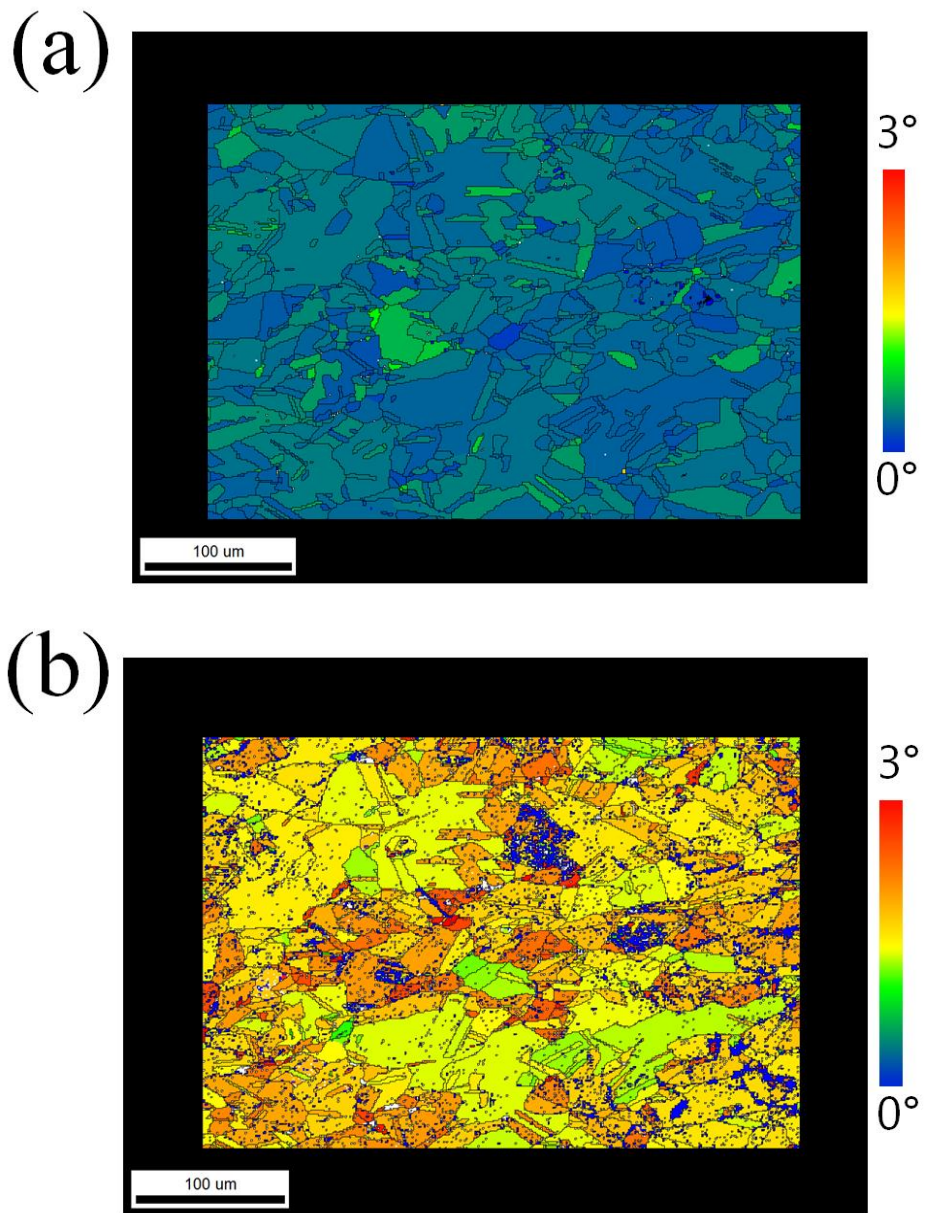


Figure 3.15 GAM maps of (a) undeformed state and (b) 9.2% tensile deformed state.

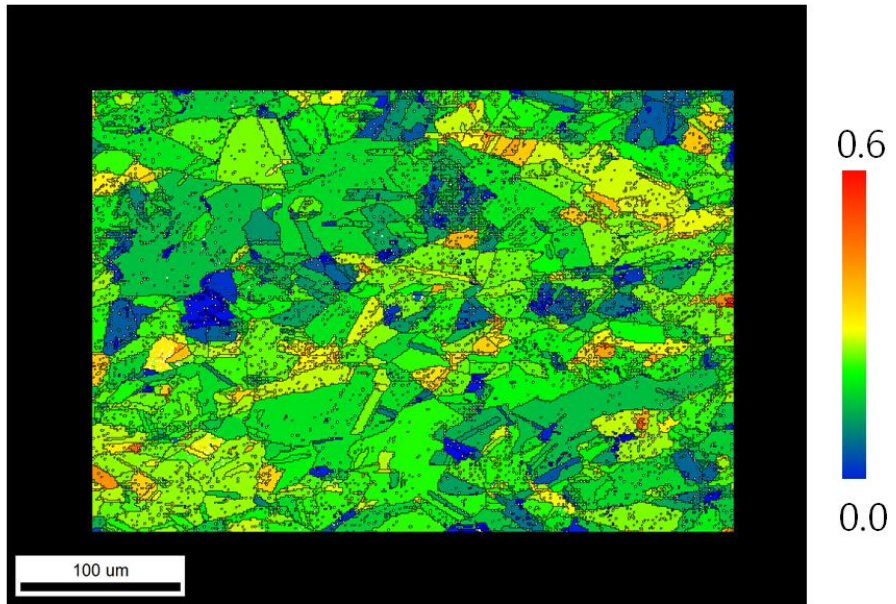


Figure 3.16 Grain average maximum shear strain map after 9.2% tensile deformation.

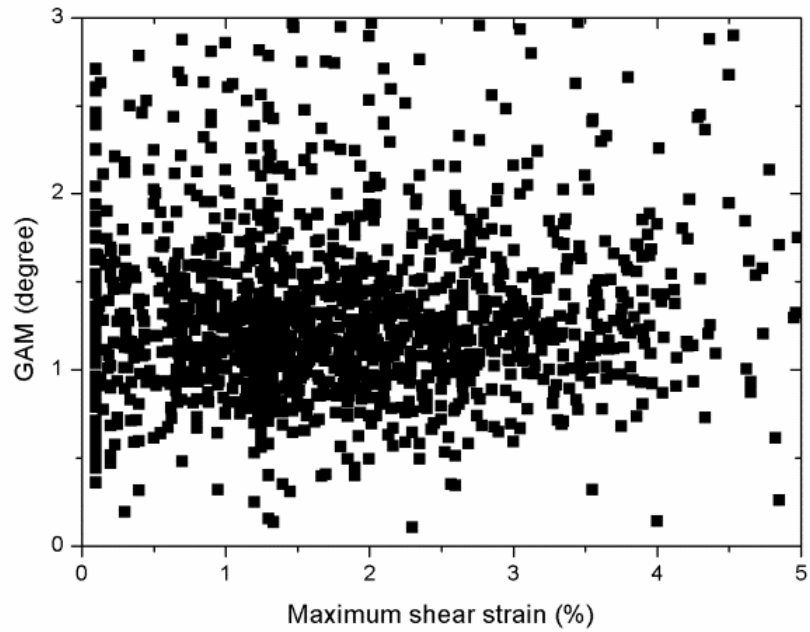
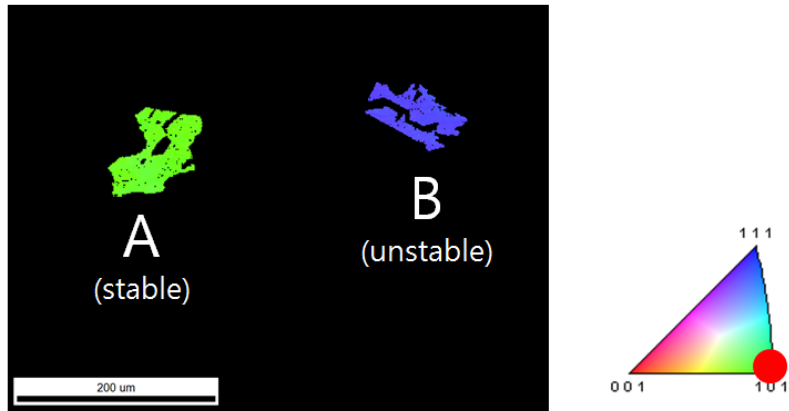
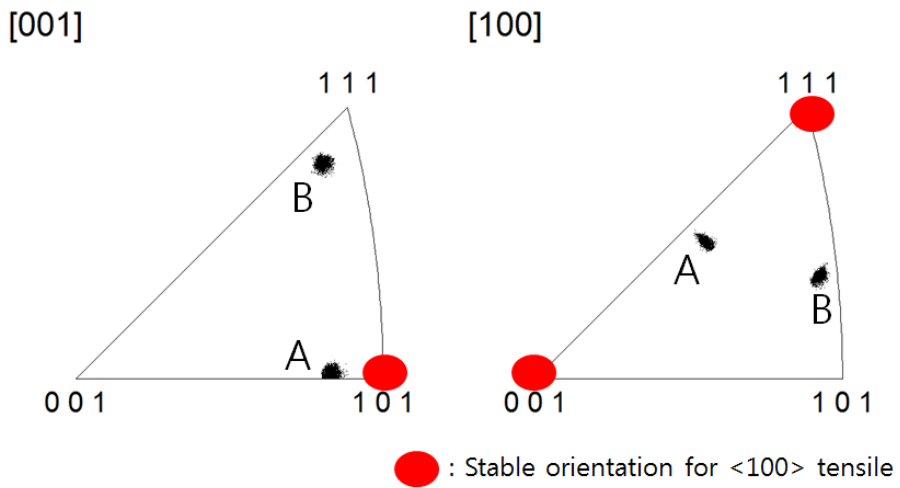


Figure 3.17 GAM as function of grain average maximum shear strain of 9.2% tensile specimen.

Seen from other researches and these results, it is clear that overall average value of KAM/GAM becomes greater when deformation becomes more severe, statistically. However, locally evaluated KAM/GAM values have quite weak correlation with applied strain of the measured spot. We thought these results can be caused by difference of orientational stability for deformation mode. If distortion of crystal orientation is influenced by orientational stability for deformation mode, increasing rate of misorientation varies with orientational stability. That is, increased KAM/GAM value can be varied by initial orientation even though applied strain is same. In order to verify this, two grains which have different orientational stability were selected and compared. The grain which has more stable orientation for deformation is named “A” and unstable grain is named as “B”. Other characteristics of selected grains are limited as similar level except crystal orientation. In this experiment, uniaxial tension test was performed along $\langle 100 \rangle$ direction of specimen. Stable orientation of FCC material for $\langle 100 \rangle$ direction tensile is known as (110)[100] and (110)[111] in $(hkl)[uvw]$ Miller indices [34-36]. Misorientation between grain A and stable orientation is 23° . And in case of grain B, the misorientation with stable orientation is 37° . Selected grains are indicated in Fig. 3.18 (a) and inverse pole figures are drawn as Fig. 3.18 (b). Information of grain A and B is stated as Table 3.1.



(a)



(b)

Figure 3.18 (a) ND orientation map and (b) inverse pole figures of selected grains.

	<i>Crystal orientation as Euler angles (degree)</i>	<i>Misorientation with stable orientation for <100> tensile (degree)</i>	<i>Grain size (μm)</i>	<i>Schmid factor for <100> tensile</i>	<i>Grain average KAM (degree)</i>
Grain A	146.4, 37.9, 180.7	23	70.3	0.43	0.91
Grain B	255.4, 47.7, 131.1	37	63.2	0.43	0.81

Table 3.1 Information of selected grains.

In order to observe overall tendencies of strain concentration and misorientation developing, maximum shear strain maps of grain A and B were drawn with individual KAM maps as Fig. 3.19. And we found there are undeformed areas in both grain A and B. If the areas were really not formed, the crystal orientation should be conserved. Thus crystal orientation maps of undeformed and deformed grain were compared each other. In addition, misorientation between undeformed grain orientation and deformed grain was calculated and mapped as Fig. 3.20 and 3.21. As shown in the figures, undeformed areas of both grain A and B conserve their original crystal orientations. And interestingly, tendency of maximum shear strain was quite well corresponded with KAM in grain B as shown in Fig 3.19 (b). But in case of grain A, there was little correlation between the maps as Fig 3.19 (a). The same tendency was also found in Fig. 20 and 21. For precise quantitative analysis, KAM values of respective grains were also plotted as function of maximum shear strain as indicated in Fig. 3.22. As a result, increasing rate of KAM was higher in grain B than grain A. That is, it is verified that distortion of crystal orientation is dependent on orientational stability for deformation mode. Thus, increased KAM/GAM value will be varied by initial orientation of deformed grains. For these reasons, it is unreliable in most cases to use KAM or GAM as direct indicator of quantitative strain. KAM can be indicator of intragranular strain, but it is also not reliable for orientational stable grain.

Above all, it is important to regard initial texture of deformed specimen for texture based deformation analysis.

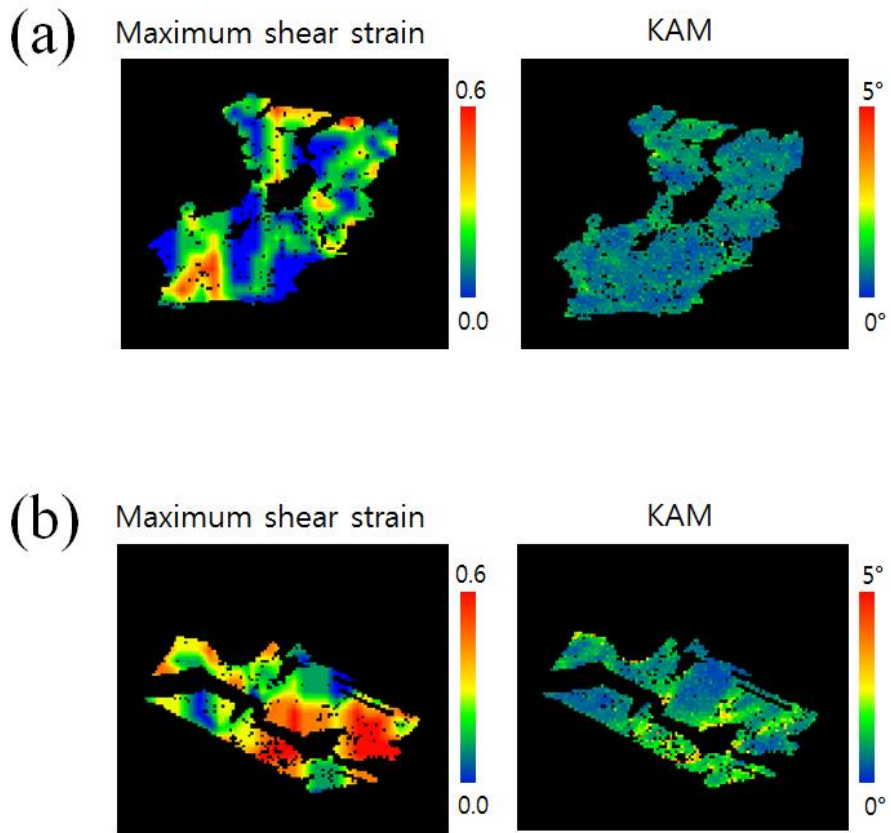


Figure 3.19 Maximum shear strain map and KAM map of (a) grain A and (b) grain B.

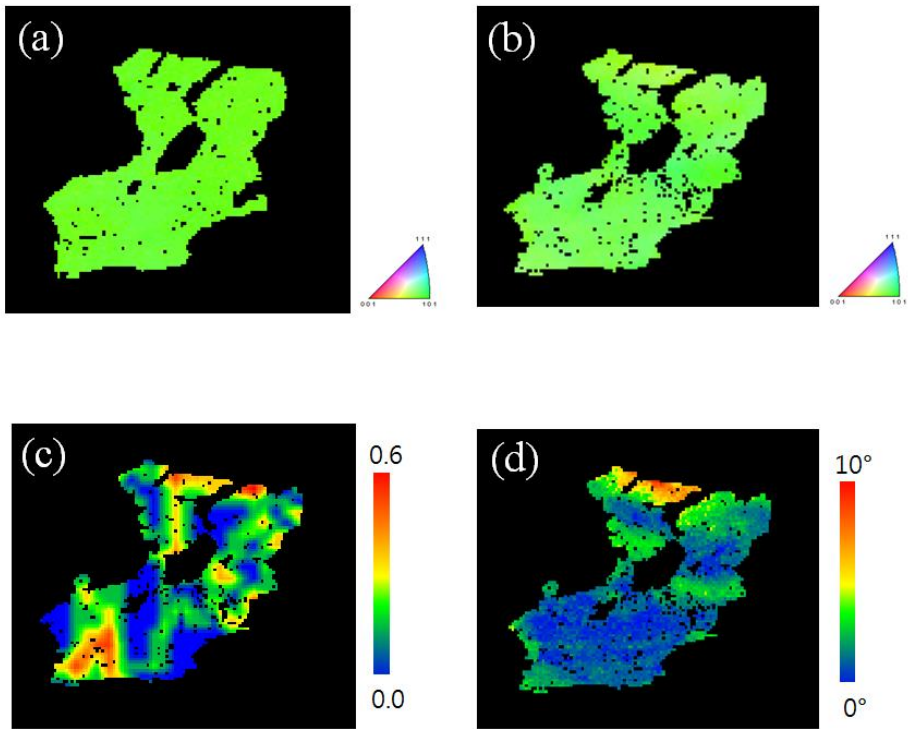


Figure 3.20 ND orientation map of (a) undeformed and (b) after 9.2% tensile state of grain A. And (c) maximum shear strain map and (d) misorientation map with original orientation of deformed grain A.

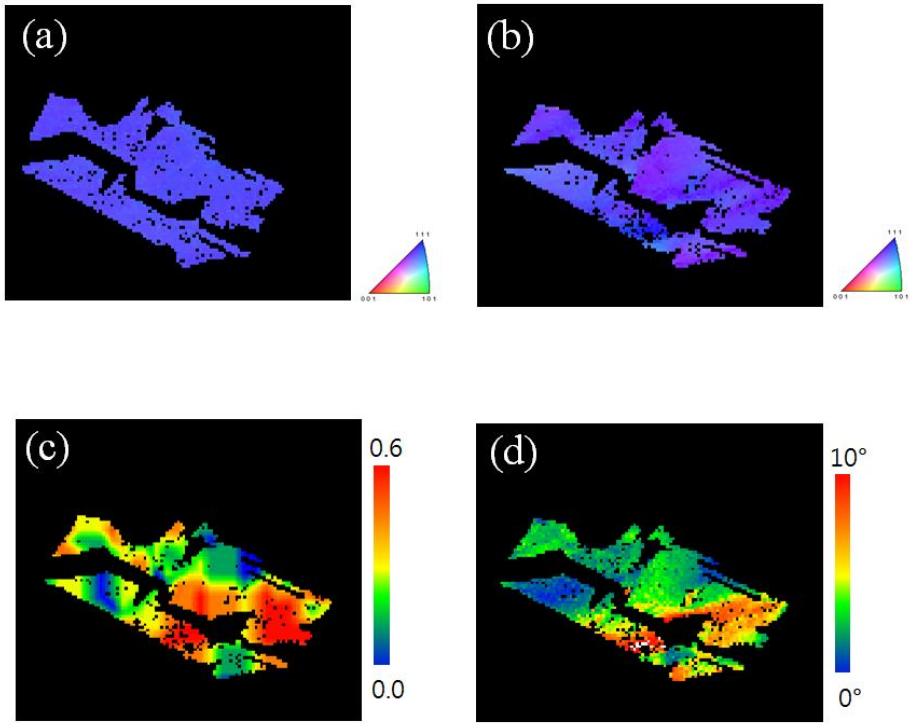


Figure 3.21 ND orientation map of (a) undeformed and (b) after 9.2% tensile state of grain B. And (c) maximum shear strain map and (d) misorientation map with original orientation of deformed grain B.

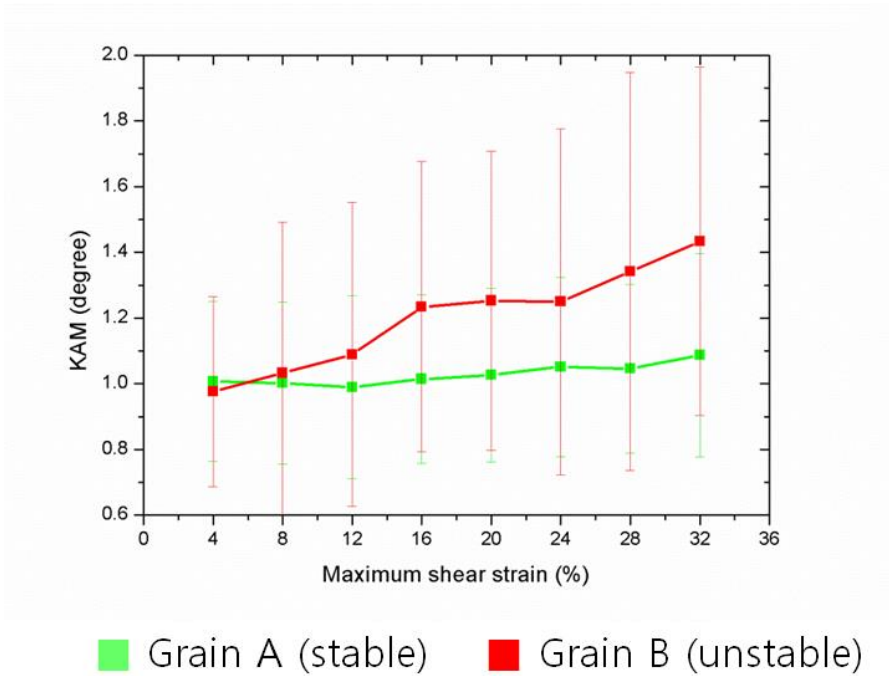


Figure 3.22 KAM values of selected grains as function of maximum shear strain.

3.4 Summary

In order to investigate relationship between strain and misorientation, DIC and EBSD analysis was carried out by using in-situ deformation device equipped in SEM chamber. For well indexed precise EBSD image with gray scale pattern for DIC, carbon coat patterning method was applied. Conventional speckle patterning method is inappropriate for EBSD by this research, since the EBSD image is seriously damaged by the speckles. Selected area of full annealed Cu specimen was captured by SEM, and same area was also scanned by EBSD during uniaxial tension. The sequential SEM images during deformation were analyzed by DIC and quantitative strain maps were drawn. As a result, accurate quantitative strain, precise microstructure and texture of the selected area could be measured together.

Then KAM and GAM maps were drawn and directly compared with maximum shear strain map, in order to correlate local strain and misorientation. As generally known, overall average value of KAM or GAM becomes greater when deformation becomes more severe, statistically. However, locally evaluated KAM and GAM values have quite weak correlation with applied local strain. One of the reasons for this, we thought these results can be caused by difference of orientational stability for deformation mode. In order to verify this, two grains which have different

orientational stability were selected and compared. As a result, it was shown that distortion of crystal orientation and increasing misorientation are dependent on orientational stability for deformation mode. Thus, increased KAM/GAM value will be varied by initial orientation of deformed grains. For these reasons, we could conclude that it is unreliable in most cases to use KAM or GAM as direct indicator of quantitative strain, and initial texture of deformed specimen should be regarded to estimate deformation behavior from texture information.

3.5 References

- [1] M. Kamaya, T. Kitamura, *International Journal of Fracture*, 124 (2003) 201-213.
- [2] R. Magdowski, F. Vaillant, C. Amzallag, M.O. Speidel, *Proc. of the 8th Intl. Symp. on Environmental Degradation of Materials in Nuclear Power Systems-water Reactors*, (1997) 333-338.
- [3] E.M. Lehockey, Y. Lin, O.E. Lepik, *Electron Backscatter Diffraction in Materials Science*, (2000) 247-264.
- [4] A.J. Wilkinson, P.B. Hirsch, *Micron*, 28 (1997) 279-308.
- [5] A.J. Schwartz, M. Kumar, B.L. Adams, *Electron Backscatter Diffraction in Materials Science*, (2000).
- [6] F.J. Humphreys, *J. Mater. Sci.*, 36 (2001) 2833-3854.
- [7] M. Kamaya, A.J. Wilkinson, J.M. Titchmarsh, *Nuclear Engineering and Design*, 235 (2005) 713-725.
- [8] M. Kamaya, A.J. Wilkinson, J.M. Titchmarsh, *Acta Materialia*, 54 (2006)

539-548.

[9] A.J. Wilkinson, D.J. Dingley, *Acta Metallurgica Et Materialia*, 39 (1991) 3047-3055.

[10] K. Mino, R. Imamura, H. Koiwai, C. Fukuoka, *Advanced Engineering Materials*, 3 (2001) 922-924.

[11] J.C. Glez, J. Driver, *Journal of Applied Crystallography*, 34 (2001) 280-288.

[12] D.N. Githinji, S.M. Northover, P.J. Bouchard, M.A. Rist, *Metall Mater Trans A*, 44A (2013) 4150-4167.

[13] Z.P. Lu, T. Shoji, F.J. Meng, H. Xue, Y.B. Qiu, Y. Takeda, K. Negishi, *Corros Sci*, 53 (2011) 1916-1932.

[14] M. Mineur, P. Villechaise, J. Mendez, *Mat Sci Eng a-Struct*, 286 (2000) 257-268.

[15] A. Girones, P. Villechaise, A. Mateo, M. Anglada, J. Mendez, *Mat Sci Eng a-Struct*, 387 (2004) 516-521.

[16] T.E. Maitland, *Ethnic Dis*, 17 (2007) 313-319.

- [17] R. Yoda, T. Yokomaku, N. Tsuji, *Materials Characterization*, 61 (2010) 913-922.
- [18] N. Jia, R.L. Peng, G.C. Chai, S. Johansson, Y.D. Wang, *Mat Sci Eng a-Struct*, 491 (2008) 425-433.
- [19] J.Y. Kang, B. Bacroix, H. Regle, K.H. Oh, H.C. Lee, *Acta Materialia*, 55 (2007) 4935-4946.
- [20] W.H. Peters, W.F. Ranson, *Optical Engineering*, 21 (1982) 427-431.
- [21] S.R. McNeill, M.A. Sutton, W.J. Wolters, W.H. Peters, *Image Vis Comput*, 1 (1983) 1333-1339.
- [22] S. Yoneyama, A. Kitagawa, S. Iwata, K. Tani, H. Kikuta, *Experimental Techniques*, 31 (2007) 34-40.
- [23] M.A. Tschopp, B.B. Bartha, W.J. Porter, P.T. Murray, S.B. Fairchild, *Metallurgical and Materials Transactions A: Physical Metallurgy and Materials Science*, 40 (2009) 2363-2368.
- [24] J. Kang, Y. Ososkov, J.D. Embury, D.S. Wilkinson, *Scripta Materialia*, 56 (2007) 999-1002.
- [25] G. Martin, D. Caldemaison, M. Bornert, C. Pinna, Y. Bréchet, M. Véron,

- J.D. Mithieux, T. Pardoën, *Experimental Mechanics*, 53 (2013) 205-215.
- [26] P. Zhou, K.E. Goodson, *Optical Engineering*, 40 (2001) 1613-1620.
- [27] Y. Zhang, T.D. Topping, E.J. Lavernia, S.R. Nutt, *Metallurgical and Materials Transactions A: Physical Metallurgy and Materials Science*, 45 (2014) 47-54.
- [28] H. Na, S. Nambu, M. Ojima, J. Inoue, T. Koseki, *Scripta Materialia*, 69 (2013) 793-796.
- [29] B. Ahn, H.I. Koo, N.I. Cho, in: 2014 Asia-Pacific Signal and Information Processing Association Annual Summit and Conference, APSIPA 2014, 2014.
- [30] B. Pan, *Experimental Mechanics*, 51 (2011) 1223-1235.
- [31] B. Pan, A. Asundi, H. Xie, J. Gao, *Optics and Lasers in Engineering*, 47 (2009) 865-874.
- [32] B. Pan, P. Cheng, B. Xu, in: *Proceedings of SPIE - The International Society for Optical Engineering*, 2005, pp. 544-551.
- [33] B. Pan, K. Li, W. Tong, *Experimental Mechanics*, 53 (2013) 1277-1289.

- [34] J.Q. Zhao, P. Zeng, L.P. Lei, Y. Ma, *Optics and Lasers in Engineering*, 50 (2012) 473-490.
- [35] C. Liu, J. Yuen, A. Torralba, *IEEE Transactions on Pattern Analysis and Machine Intelligence*, 33 (2011) 978-994.
- [36] Y. Zhou, K.W. Neale, L.S. Tóth, *International Journal of Plasticity*, 9 (1993) 961-978.
- [37] F. Montheillet, M. Cohen, J.J. Jonas, *Acta Metallurgica*, 32 (1984) 2077-2089.
- [38] S. Ahzi, S. M'Guil, in: *Solid State Phenomena*, 2005, pp. 251-258.

4. Conclusion

Duplex stainless steel (DSS) is generally known as material combining good strength with corrosion properties. However, it is hard to understand mechanical behavior of DSS, since each phase in DSS has different response to applied stress or strain. Therefore, many researches have been carried out to understand complex deformation behavior of DSS. Until a recent date, three conventional methods were developed to analyze relationship between small scale deformation of respective phases in DSS and macro-scale deformation behavior. These are neutron diffraction analysis, EBSD (texture) base analysis and digital image base analysis. However, the respective analysis methods have several disadvantages. We want to overcome those demerits and suggest advanced analysis methods in order to analyze complex deformation behavior of DSS, precisely.

Neutron diffraction is one of the conventional methods to analyze deformation behavior of DSS. Especially, the plastic yielding behavior of each phase in DSS was often focused by time-of-flight analysis using in-situ neutron diffraction. However, the neutron diffraction has bad accessibility because the size of equipment is quite huge and there are few places that can use it. And it is difficult to separate the individual contribution of each phase

from macroscopic stress or strain. In addition, applied stress can't be measured precisely by this method since there is a limitation in the step for the static load control during in-situ neutron diffraction. For these reasons, more accessible technique, nanoindentation was suggested as the alternative method, and compared with in-situ neutron diffraction in Part I. Nanoindentation was chosen since separated intrinsic mechanical behavior of each phase can be measured, and applied stress can be obtained as continuous value. In order to observe the intrinsic deformation behavior of each phase in DSS, nanoindentation tests combined with EBSD were performed. Then an angular-dispersive in-situ neutron diffraction test was carried out to correlate the small-scale nanoindentation behavior to the macro-scale tensile behavior. Consequently, the tendency of plastic yielding from two different analyses correspond well each other. Thus we could conclude tendency of maximum shear stress when first pop-in occurs can represent tendency of yield stress. And we also found dislocation nucleation energy (DNE) is closely correlated with the elasto-plastic transition stress. Thus we also could conclude that the difference of elasto-plastic transition stresses in both DSS can be explained by DNE and the SFE in γ could be evaluated by nanoindentation based DNE calculation.

In Part II, EBSD supported digital image correlation (DIC) analysis was introduced to improve EBSD (texture) and digital image base deformation

analysis methods for DSS. In EBSD base deformation analysis, the phase which has intensely distorted texture regards as severely deformed phase. However, correlation between strain and misorientation is not investigated clearly. Thus it is ambiguous to define deformation by texture information and, of course, accurate strain is cannot be measured by EBSD base deformation analysis. On the contrary, precise quantitative strain can be directly measured by digital image base deformation analysis method called DIC. But with this method, phase/grain boundaries cannot be identified clearly because they are identified by etched surface morphology. We thought that precise strain analysis regarding microstructure is possible if digital image base analysis can be supported by EBSD technique. Thus EBSD combined DIC analysis method was tried in order to measure accurate quantitative strain with regarding precise microstructure and texture. For well indexed precise EBSD image with gray scale patterned SEM images for DIC, carbon coat patterning technique was also developed. With this method, accurate quantitative strain, precise microstructure and texture of the selected area could be measured together. Then Kernel average misorientation (KAM) and grain average misorientation (GAM) maps were drawn and directly compared with maximum shear strain map in order to correlate local strain and misorientation. As generally known, overall average state of misorientation correlated with macroscopic applied strain, statistically. However, locally evaluated KAM/GAM values have quite weak correlation with applied local strain of

the spot. One of the reasons for this, we found crystal distortion and increasing misorientation by deformation are influenced by orientational stability for deformation mode. That is, locally increased KAM/GAM values can be varied by initial orientation of observed area, not only applied strain. Thus we conclude that orientational stability for applied deformation mode should be regarded for reliable strain analysis by EBSD.

국문 초록

스테인리스 강재는 1900년대 이후부터 그 고 내식성을 바탕으로 가까운 조리도구, 가구에서부터 멀게는 우주비행선에 이르기 까지 수 많은 분야에 이용되어 왔다. 그 중에서도 페라이트와 오스테나이트로 이루어진 2상 스테인리스 강재는 기존의 내식성에 더해 고 내구성, 고 강도를 갖춰 최근 주목 받고 있다. 하지만 해당 강재는 서로 다른 기계적 성질을 지닌 두 개의 상이 하나의 강재에 혼재되어 있어 그 기계적 거동의 예측이 어렵고, 물성 제어도 난해하다. 이러한 이유로, 해당 강재의 기계적 거동을 이해하여 효율적으로 재료를 설계하기 위해, 2상 스테인리스 강재의 변형 거동에 대한 다양한 연구가 진행되었다.

2상 스테인리스 강재의 변형 거동을 분석하는 대표적인 방법은 크게 셋으로 구분된다. 중성자 회절 분석법, 집합조직 기반 분석법, 이미지 기반 분석법이 그것인데, 선행 연구자들은 이를 이용해 2상 스테인리스 강재의 변형에 대한 훌륭한 연구를 진행하였지만, 한편으로 각각의 분석 기법이 지닌 약점들도 함께 드러났다. 본

논문에는, 2상 스테인리스 강재의 일반적인 분석 방법과 그간 이슈가 되었던 문제점들이 소개되어 있다. 또한 이를 극복하고, 2상 스테인리스의 변형 거동에 대한 더 정교한 분석을 수행하기 위해 시도된 새로운 분석 기법들에 대한 연구 결과가 수록되어 있다.

먼저 2상 스테인리스의 변형 거동 분석에 가장 일반적으로 사용되는 중성자 회절 분석 기법의 여러 단점들을 극복하고자, 나노인텐테이션 기반 분석 기법이 제안되었다. 중성자 회절 분석 기법은, 강재의 변형 시 동일 방위를 가지는 결정립들의 평균 Lattice strain이 변화하는 경향을 바탕으로 각 상 별 항복 거동을 예측한다. 하지만, 이 기법으로는 측정된 데이터로부터 각 상의 변형거동을 정확하게 분리하여 해석하기가 어렵다. 따라서 분석 과정에서 대부분 Isostress상태가 가정되어 두 상의 Strain Partitioning 현상이 무시되고, 따라서 각 상에 가해진 정확한 응력을 산출하기 어렵다. 그리고 또한, 데이터 측정 구간을 제어하는 것에 한계가 있어, 원하는 상황에서 연속적이고 정확한 응력 값을 얻을 수 없다. 게다가, 중성자 회절 실험은 그 설비의 크기가 거대하고 수가 적어 접근성이 매우 낮은 편이다. 이러한 이유로 더 접근성이 좋은 상 별 변형 분석 기법이 요구되었고, 본 연구진은 그 후보로 나노인텐테이션을 선정하였다.

나노인텐테이션을 이용하면, Strain partitioning의 영향 없이 강재의 독립된 결정립별/상별 변형 거동을 관찰할 수 있으며, 응력 상태를 연속적인 값으로 측정 가능하다. 또한 장비도 단순한 편으로 접근성도 높다. 따라서 본 연구진은 나노인텐테이션 기반 분석법이 중성자 회절 기반 변형 분석법을 대체할 수 있을 것으로 판단하고, Fe-24.67Cr-7.04Mn-3.98Ni-3.88Mo-0.49Si-0.45N-0.022C 의 조성을 가지는 DSH, Fe-17.2Cr-5.9Mn-5.01W-2.54Mo-0.31Si-0.43N-0.012C 의 조성을 가지는 DSL 두 2상 스테인리스 강재를 대상으로 나노인텐테이션을 이용해 그 항복 거동을 상 별로 분석하였다. 그 결과, DSH의 경우 Austenite가 Ferrite에 비해 20%가량 낮은 힘에서 소성 변형이 시작되는 것을 확인하였으나, DSL에서는 두 상이 모두 비슷한 힘에서 소성 변형을 시작하는 경향을 나타내었다. 그리고 이와 같은 미시적 경향이 거시적인 1축 인장 시에도 동일하게 나타나는지 확인하기 위해 in-situ 중성자 회절 실험을 진행하여 시편의 각 상 별 항복 응력을 산출하였다. 그 결과 나노인텐테이션 실험 결과의 경향과 마찬가지로, DSH의 경우 Austenite가 Ferrite에 비해 낮은 응력에서 소성 변형을 시작하고, DSL의 경우 두 상이 모두 비슷한 응력에서 소성 변형을 시작하는 경향이 나타났다. 즉, 나노인텐테이션을 통해 구한 미시적 항복

거동과 in-situ 중성자 회절 실험을 통해 구한 거시적 항복 변형이 밀접한 관련이 있음이 밝혀졌고, 이를 통해 2상 스테인리스의 상 별 항복 경향을 구함에 있어 나노인덴테이션 기반 분석 기법이 중성자 회절 기반 분석 기법을 대체할 수 있을 것이라고 판단되었다. 또한 본 연구진은 실험을 통해 얻어진 데이터들을 바탕으로 전위 생성 에너지를 계산하여 각 시편의 상 별 항복 강도의 차이가 전위 생성 에너지의 차이에 기인한다는 것 또한 확인할 수 있었다.

두 번째로, 디지털 이미지 기반 변형 분석 기법과 집합조직 기반 변형 분석 기법을 보완하기 위해, EBSD와 결합된 디지털 이미지 기반 변형 분석 기법이 개발되었다. 그간 다양한 연구를 통해 일반적으로 금속재료의 변형 시, 그 변형량이 증가할수록 결정 방위의 뒤틀림이 심해져, 변형된 시편의 평균 Misorientation의 값이 증가한다는 사실이 보고되었다. 이를 바탕으로 다양한 Misorientation을 대표하는 지표 값 (Kernel average misorientation (KAM), Orientation spread (OS), Grain average misorientation (GAM))들이 높은 영역이 많은 변형량을 수용한 부분으로 간주되곤 했다. 그러나, 전체적인 변형량이 증가함에 따라 Misorientation의 평균값이 증가하는 경향이, EBSD 이미지 상 국소 구간의 Misorientation이 해당 부위의 직접적인 변형량을

나타낸다고 해석될 수는 없다. 이를 위해서는, 변형량과 Misorientation간의 정량적 관계에 대한 연구가 선행 되어야 한다. 반면, 디지털 이미지 기반 변형 분석 기법 (DIC)을 이용하면 변형 전후의 디지털 이미지를 비교 분석하여 국소적인 부위의 변형량을 정량적으로 산출할 수 있다. 그러나 해당 기법은 결정립계나 상 경계를 식각된 시편 표면의 형상을 통해 구분하기 때문에, 그 구분이 모호하여 미세구조와 변형량 사이의 정확한 관계 도출이 어렵다. 하지만 2상 스테인리스의 복잡한 변형 거동을 정밀히 분석하기 위해서는, 정확하고 정량적인 변형량 정보와 해당 구간의 미세조직, 결정방위 정보가 모두 고려되어야 한다. 따라서 앞서 기술된 두 변형 분석 기법의 단점을 개선하고, 국부적 변형량과 Misorientation간의 관계에 대한 정량적 분석을 수행하여 집합조직 기반 변형 거동 분석을 보완하고자, 600℃에서 4시간 열처리한 순도 99.9% Cu 시편을 이용해 DIC (Digital Image Correlation)와 EBSD의 연계 분석이 시도되었다. DIC분석을 위해서는 국부적 변형 추적을 위해 시편 위에 Nano-micro particle을 도포해야 하는데, 이러한 Particle들이 EBSD 측정을 방해하여 Misorientation과 같은 주변 방위와의 관계가 중요한 지표에 큰 오류를 야기한다. 따라서 정밀한 결정 방위 정보를 얻는 동시에 DIC 분석을 수행하기 위해,

기존의 Nano-micro particle 도포 기법을 대체하여 Carbon coat patterning 기법이 개발되었고, 이 방법을 통해 DIC분석을 수행하는 동시에 정밀한 EBSD 이미지를 얻을 수 있었다. 이를 바탕으로 9.2% 1축 인장 변형을 수행한 Cu 시편의 Local strain과 여러 Misorientation 지표 (KAM, GAM) 간의 정량적 관계에 대한 분석을 수행한 결과, 통계적으로 변형량이 클수록 결정립의 왜곡이 심해진다는 일반적인 경향은 확인 했지만, 국부적 변형량과 해당 구간의 KAM, GAM 값 사이에서 밀접한 연관성을 찾을 수 없었다. 본 연구진은 이러한 경향이 나타나게 된 하나의 이유로, 변형에 대한 결정립의 방위 안정성 차이를 제시하였고, 결정립마다 그 초기 방위에 따라 변형에 따른 Misorientation의 증가 추세가 다를 수 있음을 밝혀내었다. 따라서, EBSD 이미지 상에서 KAM과 GAM등의 값을 초기 집합조직에 대한 고려 없이 직접적인 국부적 변형량의 지표로 사용하는 것에는 문제가 있으며, 변형에 대해 불안정 방위를 가지는 결정립에 한해, KAM 값을 결정립 내 변형량의 척도로는 사용할 수 있다는 결론을 얻을 수 있었다.

핵심어: 2상 스테인리스, 페라이트, 오스테나이트, 기계적 거동,

정량적 변형량 분석, 중성자 회절, 후방산란 전자 회절, 전자 현미경,
나노인덴테이션, 항복 응력, 전위 생성 에너지, 디지털 이미지 분석,
입자 도포 패턴 기법, 탄소 코팅 패턴 기법, 집합조직, 어긋남각,
결정 방위, 방위 안정성

Student number: 2009-20589